UNIVERSITY OF SOUTHAMPTON

Faculty of Engineering and Physical Sciences
School of Electronics and Computer Science

Photonic integrated circuit: Optimization and applications

by

Shumeng Wang
MSc

A thesis for the degree of
Doctor of Philosophy

July 2023

University of Southampton

Abstract

Faculty of Engineering and Physical Sciences
School of Electronics and Computer Science

Doctor of Philosophy

Photonic integrated circuit: Optimization and applications

by Shumeng Wang

Photonic integrated circuit (PIC) is a device that combines multiple optical components on a single silicon chip. It leverages the properties of silicon to enable the integration of complex optical functionalities. PIC offers several advantages, including high integration density, compatibility with CMOS fabrication process, low power consumption and potential for large-scale production. They have applications in various fields such as data communication, sensing, nonlinear optics, quantum optics, etc. This thesis proposes three novel PICs that can be applied to different fields including nonlinear optics and sensing, respectively.

Firstly, an unsuspended silicon waveguide platform for enhanced stimulated Brillouin scattering is proposed. The structure is optimized by using genetic algorithm (GA). By limiting the maximum etching step to two during the GA process, a simple and fabricable unsuspended structure is obtained. The optimized platform can realize large SBS gain without suspending the Si waveguide. The best gain coefficient comes from the forward SBS of fundamental TE-like mode with the value of $2462 W^{-1} m^{-1}$. This gain value is 8 times larger than the recent result.

Secondly, a novel on-chip optical frequency domain reflectometry (OFDR) system is proposed theoretically and experimentally. The experiment results show that the system achieves a spatial resolution of $7.59 \mu m$, which is, to our best knowledge, the highest value achieved on-chip. The optical components in the system are designed by traditional methods and photonic inverse design approach, respectively. It is found that the footprint of the inverse-designed-components is at least 20 times smaller than the devices designed by traditional methods, which is essential for ultra-compact PIC.

In addition, to further improve the detecting scheme of the on-chip OFDR system, a modified direct-binary-search (DBS) algorithm is proposed and used to design a novel monolithically integrated polarization rotator and splitter with designed power ratio. The device can fulfil both polarization rotation (TE_{00} to TE_{00} and TM_{00} modes) and power splitting with a designed power ratio. The measured insertion loss is less than 1 dB and the crosstalk between TE_{00} and TM_{00} modes is less than -9.5 dB. This device

can improve the detecting scheme of our on-chip OFDR system, where the detection complexity of the system can be reduced.

Lastly, mode localization is, for the first time, established in optical system. A novel sensing mechanism based on the optical mode localization effect is applied to both optical fibre system and PIC to form ultra-sensitive senors, respectively. The experiment results exhibits at least 3 orders of magnitudes higher sensitivity than the traditional frequency-shift, which can be applied for ultra-sensitive temperature sensing and high-speed modulation.

Contents

List of Figures

List of Tables

Declaration of Authorship

I declare that this thesis and the work presented in it is my own and has been generated by me as the result of my own original research.

I confirm that:

1. This work was done wholly or mainly while in candidature for a research degree at this University;
2. Where any part of this thesis has previously been submitted for a degree or any other qualification at this University or any other institution, this has been clearly stated;
3. Where I have consulted the published work of others, this is always clearly attributed;
4. Where I have quoted from the work of others, the source is always given. With the exception of such quotations, this thesis is entirely my own work;
5. I have acknowledged all main sources of help;
6. Where the thesis is based on work done by myself jointly with others, I have made clear exactly what was done by others and what I have contributed myself;
7. None of this work has been published before submission

Signed:..... Date:.....

Acknowledgements

First, I would like to express my heartfelt appreciation to Dr. Jize Yan, my supervisor, for providing me with constant support and guidance throughout my doctoral studies. His expertise, advice, and motivation were always a source of inspiration and assistance in resolving any issues. His generosity and kindness in sharing his knowledge and experience are greatly appreciated. I feel fortunate and deeply thankful for the chance to collaborate with him.

I want to thank to all members in our group, Yu Feng, Hailong Pi, Wangke Yu, Chuang Sun, Gaoce Han, Peng Li, Weilin Jin and Zixuan Wang for the helps and discussions.

Lastly, I would like to thank my parents and my girlfriend, for all their support and sacrifice. You the motivation that supports me during my PhD.

Definitions and Abbreviations

PIC	Photonic integrated circuit
DBS	Direct binary search
FOM	Figure of Merit
PhC	Photonic crystal
RIE	Reactive ion etching
GA	Genetic algorithm
PSO	particle swarming optimization
OAM	Oribital angular momentum
TO	Topology optimization
E	Electric field
E_{adj}	Adjoint field
J	Current density
ϵ	permittivity
μ_0	Permeability
ω	Frequency
FDTD	Finite difference time domain method
FEM	Finite element method
ANN	Artifical neural network
GAN	Generative adversarial network
SBS	Stimulated Brillouin scattering
Q_m	Quality factor
TE	Transverse electric
TM	Transverse magnetic
OFDR	Optical frequency domain reflectometry
DFOS	Distributed fibre optical sensing
BOTDR	Brillouin optical time domain reflectometry
BOTDA	Brillouin optical time domain analysis
TLS	Tunable laser source
OC1	Optical coupler 1
OC2	Optical coupler 2
FUT	Fibre under test
PD	Photodetecto

v_0	Start frequency
γ	Linear frequency sweepng speed
τ_z	Time delay
n_g	Group index
c	Speed of light in vacuum
α	Attenuation coefficient
R	Reflection coefficient
f_b	Beating frequency
σ	Sensitivity of PD
FFT	Fast Fourier Transform
β	Propagation constant
v_{mph}	Phase velocity
v_{mgr}	Group velocity
τ_{mgr}	Group delay
τ_{mph}	Phase delay
MZI	Mach-Zehnder interferometer
MI	Main interferometer
AI	Auxiliary interferometer
ΔV	Frequency sweeping range
FWHM	Full width at half-maximum
GC	Grating coupler
OPD	Optical path difference
MMI	Multimode interferometer
SOI	Silicon on insulator
ICP	Inductively coupled plasma
SEM	Scanning Electron Microscope
PRE	Power ratio error
MEMS	Micro-electro-mechanical system
K	Spring
C	Damping
M	Mass
$\omega^{\pm}$	In-phase and out-of-phase mode frequencies
DoF	Degree of fredom
κ	Coupling coefficient
t	Transmission coefficient
λ_{res}	Resonant wavelength
FSR	Free spectral range
n	Refractive index
S-mode	Symmetric mode
AS-mode	Antisymmetric mode
CMT	Coupled mode theory

TEC	Thermoelectric
ER	Extinction ratio

Chapter 1

Introduction

1.1 Background

Silicon photonics integrated circuits (PICs) are devices that leverage silicon photonics technology to integrate various optical components and functions on a silicon chip. They offer a platform for the development of miniaturized, high-performance, and cost-effective optical systems. Silicon photonics technology utilizes the unique properties of silicon to manipulate and control light on a chip-scale platform. Silicon, being the dominant material in the semiconductor industry, allows for seamless integration with existing complementary metal-oxide-semiconductor (CMOS) processes. It enables the fabrication of waveguides [1], couplers[2], modulators[3], filters[4] and other optical components directly on a silicon substrate. The integration of these components allows for compact and efficient optical systems that can perfrom functions such as signal generation, modulation, photon detection, multiplexing, etc.

PICs offer several benefits that make them an attractive platform for the development of optical systems. The biggest advantage is its compatibility with CMOS technology. PICs can be seamlessly integrated with CMOS electronics. This compatibility enables the coexistence of optical and electronic functionalities on a single chip, allowing for efficient integration of optical and electrical signal processing. It also leverages the existing infrastructure and manufacturing processes of the semiconductor industry, leading to cost-effective mass production.

Secondly, PICs enable the miniaturization and dense integration of various optical components on a single chip. The use of silicon as the platform material allows for efficient fabrication of the optical functionalities in a compact format. This compactness and integration density result in smaller footprint and space-saving designs, making silicon PICs suitable for applications where space is limited. Furthermore, the compatibility with CMOS technology enables the production of

thousands or even millions of PICs on a wafer, This facilitates the deployment of silicon PICs in high-volume applications, such as data centers[5] and telecommunications networks[6].

Over the last decades, PICs have a wide range of applications across various fields, especially in sensing and nonlinear optics. In the early 2000s, researchers began exploring the use of silicon micro-ring resonators as a platform for real-time detection of biological molecules, such as proteins, DNA, and antibodies[7]. PICs offer advantages such as label-free detection, high sensitivity, real-time monitoring, etc[7]. They have applications in areas such as biomedical research[8], drug discovery[9] and environmental monitoring[7].

However, the applications of PICs, especially the silicon micro-ring resonators, in temperature sensing are not widely explored compared to their applications in biosensing or other areas. This is due to the small thermal-optical coefficient of the silicon material.The use of silicon micro-ring resonators for temperature sensing is based on the principle that the refractive index of the waveguide material changes with temperature. As temperature changes, the effective refractive index of the waveguide is altered, which in turn affects the resonance condition of the ring resonator. By monitoring the shift in the resonance wavelength or the change in the transmission spectrum, the temperature can be inferred. However, due to the small thermal-optical coefficient, the resonance wavelength shift is too small to be detected.

In the field of sensing, PICs show an unique advantage compared to traditional sensing techniques such as distributed optical fibre sensing (DOFS), which is the miniaturization and integration. Despite the achievement of high temperature sensitivity and sensing range [10, 11], DOFS is still challenging to scale up and replicate. A DOFS system typically requires multiple optical components such as fibre coupler, circulator, etc. These components are often larger in size and need to be connected to the fibre, making the overall system bulkier and more complex compared to on-chip sensing, which integrates all components on a single chip. Therefore, taking the advantanges of both DOFS and PICs is a potential way to design small-size and high sensitive sensing device.

In the field of nonlinear optics, including stimulated Brillouin scattering (SBS), PICs also find various applications. Stimulated Brillouin scattering is a nonlinear optical process that involves the interaction of light and acoustic waves in a material. It occurs when a high-power optical wave interacts with an acoustic wave, resulting in the generation of a new optical wave with a slightly different frequency due to the modulation of the refractive index by the acoustic wave[12, 13]. PICs have been used to enhance and control SBS, which can be used to design on-chip Brillouin laser[14] , filter[15], modulator[16], etc.

SBS gain refers to the amplification of light that occurs during SBS. It is a measure of the strength of this amplification process. It quantifies the increase in the power or intensity of the scattered optical wave compared to the incident optical wave. Recently, many different materials have been investigated to generate high SBS gain in PICs, such as chalcogenide glass [17], silicon [18], silicon nitride [19], AlGaAs [20] and GeSbS [21]. However, a strong SBS interaction requires the confinement of optical and acoustic waves at the same time [22], which requires a fully or partially suspension of the silicon core waveguide [23]. This will result in reduced mechanical robustness and complicated fabrication, thus hinders the integration of large-area nonlinear optical devices on a single chip.

1.2 Motivation and objective

In this thesis, we propose three novel PICs that can be applied to the field of temperature sensing and nonlinear optics, which addresses the concerns mentioned in the background section. For each PIC, the optical components are designed by using the novel photonic inverse design algorithms to achieve high performances in a system level. The photonic inverse design algorithms transform the design problem of a device into a multi-parameter optimization problem, which allows the device structure to be free from the constraints of a specific shape and thus has stronger adaptability to different design requirements. It can provide more systematic and comprehensive optimization of device and even create new device structures. Inverse design can be used to explore the performance limits of a device, which is extremely important for the theoretical development of nanophotonic optical components.

Firstly, we set our sights on nonlinear optics. As mentioned above, a strong acoustic-optic interaction in silicon requires fully or partially release of the silicon core waveguide to avoid mechanical leakage into the substrate. This will not only reduce the mechanical stability and thermal conduction, but also increase the difficulties for fabrication and large-area device integration. The currently-reported highest SBS gain is only $\sim 300 W^{-1} m^{-1}$ in unsuspended silicon waveguide [24], which is very small. Therefore, there is a clear motivation to optimize the waveguide's structure to obtain higher SBS gain.

Secondly, DOFS is already a mature technology in fibre sensing, it can measure the physical parameters along the fibre distributively instead of only measuring at specific positions. among all DOFS techniques, optical frequency domain reflectometry (OFDR) shows good tradeoffs in terms of sensitivity, accuracy, speed, detecting range and resolution [25]. One of the main advantages of OFDR system is its passive nature, which means all the components in the fibre system can be migrated onto a chip. Compared with fibre-based system, the chip-scale system can realize high

compactness and performance, also reduce the high cost from the original fibre set-up. Therefore, a motivation is the design of an on-chip OFDR system, the passive components can be made by using the inverse design algorithms.

Thirdly, mode localization effect has been widely used in MEMS (micro-electro-mechanical system) resonators for temperature and strain sensing. The sensor measures the amplitudes variations of two split resonant modes caused by localized vibrations in weakly coupled resonators, which achieves high sensitivity and signal-to-noise ratio (SNR) [26, 27]. Compared with MEMS resonators, optical resonators can achieve high quality factors without using vibration structures and vacuum conditions [28, 29, 30]. We believe mode localization effect is also feasible for optical resonators to make high sensitive senors and other tunable photonic devices, which can solve the problem that the silicon ring resonators with a small thermal-optical coefficient cannot be used for temperature sensing.

1.3 Thesis structure

Each chapter is summarized as below. In chapter 2, the works of PICs that are related to sensing and nonlinear optics are reviewed, respectively. For sensing, two mechanisms will be introduced, one is the OFDR-based sensing, the other one is the mode-localization-based sensing. For nonlinear optics, we mainly focus on the stimulated Brillouin scattering. Finally, the development of photonic inverse design, which will be used to optimize the optical components for PICs, is reviewed. Common approaches, such as direct binary search (DBS), genetic algorithm (GA), gradient descent and deep learning, are discussed in detail.

In chapter 3, genetic algorithm (GA) is utilized to find an optimal structure based on Si-AlN-Sapphire platform to obtain better SBS gain. The process of optimization is presented, and the result is generated and analyzed based on simulation.

In chapter 4, an on-chip OFDR system is proposed. The components of the system are designed by traditional methods and photonic inverse design, respectively. The performances of the components and the system are demonstrated experimentally.

In chapter 5, the optimization process of the current DBS algorithm is improved by combining general Stoke's theorem. Based on the modified DBS algorithm, a monolithically integrated polarization rotator and splitter with designed power ratio is designed. Its performance is verified experimentally. The device can be used in our on-chip OFDR system for potential improvements in detecting scheme and reduction of the set-up complexity.

In chapter 6, mode localization effect is applied to fibre and on-chip systems. Starting from the modelling of a single all-pass optical ring resonators, the mode localization

effect is firstly studied based on microring resonators. Then, the performance of the mode-localization-effect-based sensing is experimentally demonstrated in fibre- and on-chip-coupled-ring resonators, respectively.

In chapter 7, the main contributions and future works are concluded.

Chapter 2

Literature review

Photonic integrated circuits (PICs) are an emerging technology that combines the field of photonics with silicon-based circuit. The history of PICs can be traced back to the early 1990s when researchers began exploring the integration of optical components on silicon substrates [31]. At that time, the primary focus was on achieving on-chip optical interconnects for high-speed data communication within electronic systems. Over the years, significant progress has been made in the development of silicon PICs. Researchers have developed various techniques for fabricating waveguides[32], couplers[2], detectors[33] and other optical components on silicon substrates. They have also made advancements in improving the performance, integration density, and manufacturing processes of silicon PICs.

The development of PICs is rooted in the need for efficient, scalable and cost-effective solutions for optical communications, sensing, nonlinear optics and other applications. In this chapter, we focus on the state-of-art PIC applications typically in the field of temperature sensing and nonlinear optics. The main challenges and possible solutions are also discussed. After that, we introduce the photonic inverse design algorithms, which are used to optimize the optical components for each PIC.

2.1 PICs in nonlinear optics

PICs have become a significant platform for exploring and implementing nonlinear optical processes. Nonlinear optics involves the interaction of light with a material where the optical response is not directly proportional to the input intensity, leading to phenomena such as frequency conversion[34], optical parametric amplification [13, 35, 17], and nonlinear mixing[36], etc. The strong confinement of light within the waveguides in PICs enables a higher optical intensity, enhancing the nonlinear effects

in the material. This allows for efficient generation and manipulation of the nonlinear optical phenomena.

Among all nonlinear optics effects, SBS draws significant attention due to several reasons. Firstly, SBS involves a strong interaction between light and acoustic waves in a material[12, 13]. The resulting scattering process leads to efficient energy transfer between these two waves. The strong interaction strength allows for substantial amplification and manipulation of the optical signal, making SBS an attractive nonlinear process. Secondly, SBS exhibits a narrowband gain profile, typically on the order of MHz or GHz [22, 23, 37], which is useful for applications requiring precise spectral control. This narrowband gain exploits various purposes such as amplification of signals within a specific frequency range [15] and selective filtering of optical signals[38].

SBS in PICs also enables the development of on-chip Brillouin lasers. These lasers utilize the SBS effect to generate coherent and narrow-linewidth light on the same chip as the other integrated components[14]. Various waveguide designs have been explored to enhance the Brillouin gain and achieve narrow-linewidth operation. These include silicon waveguides[22], silicon nitride (SiN) waveguides[19], and hybrid platforms [20, 21, 39, 40, 24]that combine different materials for optimal light-sound interaction. Researchers have focused on methods to increase the Brillouin gain in on-chip lasers. Strategies include designing waveguides with specific dimensions and materials to optimize the interaction between light and acoustic waves. In [41], the authors utilized genetic algorithms to generate novel waveguides for stimulated Brillouin scattering. However, the optimized structures are abstract and cannot be fabricated under the current CMOS fabrication technology.

2.1.1 Stimulated Brillouin scattering

Stimulated Brillouin scattering (SBS) is a third-order nonlinear effect originating from the coupling between optical and acoustic waves[12, 13]. Assuming the light is propagating along a translationally invariant waveguide, then the optical pump and Stokes waves can be approximately described as modulated optical eigenmode, with electric field distributions:

$$\mathbf{E_p}(r,t) = a_p(y,t) \cdot \widetilde{\mathbf{e_p}}(x,z) \cdot e^{i\left(\mathbf{k_p} \cdot y - \omega_p \cdot t\right)} + c.c. \tag{2.1}$$

$$\mathbf{E_s}(r,t) = a_s(y,t) \cdot \widetilde{\mathbf{e}}_\mathbf{s}(x,z) \cdot e^{i(\mathbf{k_s} \cdot y - \omega_s \cdot t)} + c.c. \tag{2.2}$$

where $a_i(y,t)$ with (i=p,s) is the slowly-varying envelope function of the pump and Stokes waves, respectively. And $\widetilde{\mathbf{e}}_\mathbf{i}(x,z)$ represent the spatial mode distribution, which

are the solutions of the Helmholtz equations with wave vector $\mathbf{k_i}$ and angular frequency ω_i. Note that following [42], the energy in each mode is not normalized, instead the energy terms are carried through to the gain calculation in Eq. 2.7.

Similarly, the acoustic mode can also be written as:

$$\mathbf{U} = b(y,t)\widetilde{\mathbf{u}}(x,z)e^{i(\mathbf{q}\cdot y-\Omega_B\cdot t)} + c.c. \tag{2.3}$$

where $b(y,t)$, $\mathbf{q}$ and Ω_B are the slowly varying envelope function, the wave vector and the angular frequency of the acoustic wave. The function $\widetilde{\mathbf{u}}(x,z)$ is the spatial distribution of the acoustic wave displacement, which is the solution of the following eigenvalue problem:

$$\rho\Omega_B^2\tilde{u}_i + \sum_{ijkl}\left(\nabla_T + iq\hat{\mathbf{y}}\right)_j c_{ijkl}\left(\nabla_T + iq\hat{\mathbf{y}}\right)_k \tilde{u}_l = 0 \tag{2.4}$$

where i,j,k,l=(x,y,z), ρ and c_{ijkl} are thematerial density and the elastic tensor, respectively. The acoustic wave decay can be determined by the dynamic viscosity η of the waveguide material [43], this term will be considered as the material loss in this paper.

In a nano-scale waveguide, two mechanisms will contribute to the final SBS gain, which are the photoelastic interaction Q_{PE} and the moving boundary Q_{MB} (units: $W\cdot m^{-1}\cdot s$):

$$Q_{PE} = \varepsilon_0\varepsilon_{\text{core}}^2\int dr^2\sum_{ijkl}e_i^{(s)*}e_j^{(p)}p_{ijkl}\partial_k\widetilde{u}_l^* \tag{2.5}$$

$$\begin{aligned}Q_{MB} = &\int_C dr\left(\hat{\mathbf{n}}\cdot\widetilde{\mathbf{u}}^*\right)\left[\varepsilon_0\left(\varepsilon_{\text{core}}-\varepsilon_{\text{clad}}\right)\left(\widetilde{\mathbf{e}}_s\times\hat{\mathbf{n}}\right)^*\cdot\left(\widetilde{\mathbf{e}}_p\times\hat{\mathbf{n}}\right)\right.\\ &\left.-\varepsilon_0^{-1}\left(\varepsilon_{\text{core}}^{-1}-\varepsilon_{\text{clad}}^{-1}\right)\left(\widetilde{\mathbf{d}}_s\cdot\hat{\mathbf{n}}\right)^*\cdot\left(\widetilde{\mathbf{d}}_p\cdot\hat{\mathbf{n}}\right)\right].\end{aligned} \tag{2.6}$$

where ϵ_i (i=0,core,clad) are the permittivity for vacuum, core material and cladding material, respectively, and $\widetilde{d}_i$ is the induction field. Eq. 2.5 is integrated over the whole transversal plane of the waveguide, while Eq. 2.6 is a line integral to be carried out along the waveguide boundaries with normal vector $\hat{\mathbf{n}}$ pointing from the core material to the cladding material.

Finally the total Brillouin gain can be calculated by means of:

$$G_0 = Q_m\cdot\frac{2\omega_p\left|Q_{PE}+Q_{MB}\right|^2}{P_pP_s\varepsilon_B} \tag{2.7}$$

where Q_m, P_p, P_s and ϵ_B are the mechanical quality factor, the pump, Stokes modal power (units: W) and acoustic modal energy (units: $J \cdot m^{-1}$).

An efficient SBS interaction will only occur when the simultaneous conservations of energy and momentum [35] are satisfied.

$$\begin{aligned} \Omega_B &= \omega_{\mathbf{p}} - \omega_{\mathrm{s}} \\ \mathbf{q} &= \mathbf{k}_{\mathbf{p}} - \mathbf{k}_{\mathrm{s}} \end{aligned} \tag{2.8}$$

According to the relative direction between pump and Stokes waves, SBS can be categorized either as forward SBS (FSBS), where pump and Stokes waves travel co-directionally, or as backward SBS (BSBS), where pump and Stokes waves travel counter-directionally.

Based on the fact that $\Omega_B \ll \omega_p, \omega_s$ and $\omega_p \approx \omega_s$ [22], q is almost zero for FSBS while $q \approx 2k_p$ for BSBS. Here, we focus on FSBS as it requires far fewer simulation steps than backward SBS where phase matching requires simulation of several mechanical propagation vectors. Apart from the above requirements, the field distribution of the selected acoustic mode also needs to match the optical mode distribution.

To better analyse the factors affecting the final gain coefficient, one can divide the right part of Eq. 2.7 into two parts. The first part is the mechanical quality factor Q_m. This parameter reflects the mechanical energy loss. The more phonon energy leaks into the substrate, the smaller the Q_m will be. There are various sources leading to the decrease in Q_m, the two main losses concerned here are material loss $Q_{material}$ and anchor loss Q_{anchor}.

Material loss is a loss related to the acoustic wave frequency. Normally the higher the frequency is, the more significant the material loss will be [44]. For silicon, in the frequency range of gigahertz, material loss is believed to be the main factor limiting mechanical Q factorto around 1000 [35, 37].

The working wavelength is 1550 nm. At this wavelength Si has a higher refractive index than that of AlN, so the optical mode can be well confined in Si via internal reflection. Meanwhile the acoustic velocity of Si is smaller than that of AlN, so AlN can work as a buffer layer to prevent acoustic leakage into the substrate. Material loss can be calculated via the viscosity tensor of the material [19]. The authors added the viscosity tensor of silicon into the simulation model so that the actual material loss can be simulated [45].

As for the anchor loss Q_{anchor}, this can be numerically simulated by applying a perfectly mathced layer (PML) [46] around the substrate. The Q_m is the summation of these two sources ($Q_m^{-1} = Q_{\mathrm{material}}^{-1} + Q_{\mathrm{anchor}}^{-1}$).

2.1.2 Challenges and outlooks

Strong acoustic-optic interaction in silicon requires fully or partially release of the silicon core waveguide to avoid mechanical leakage into the substrate. This will not only reduce the mechanical stability and thermal conduction, but also increase the difficulties for fabrication and large-area device integration. Therefore, a silicon-compatible platform displaying large Brillouin gain while simultaneously not requiring the release of the silicon core is desired.

Many different materials have been investigated to generate high SBS gain in integrated photonic circuits, such as chalcogenide glass [17], silicon [18], silicon nitride [19], AlGaAs [20] and GeSbS [21]. Recently, a silicon-silicon nitride (Si_3N_4)-silica platform is proposed to realize SBS without suspending the core waveguide [37]. However, this platform has few limitations. The first issue is the difficulty of growing high quality Si_3N_4. Current deposition methods cannot grow single crystalline Si_3N_4 above silica due to the lattice mismatch [47]. However, the mechanical properties of Si_3N_4 depends on the crystal quality and orientation, leading to the uncertainties in the final device performance.

The second issue is that the SBS gain coefficient in unsuspended structure is greatly reduced. This results from the fact that the moving boundaries contribution is largely decreased due to the fixed boundary. To our best knowledge, the best result in non-suspended design is only around $300W^{-1}m^{-1}$ [37], while in suspended Si waveguide, the result is 10 times bigger than that [19].

AlN is another material that can be used for realizing sufficient SBS in non-suspension silicon waveguide [48]. AlN has a lower refractive index and higher acoustic velocities than these of silicon [39]. As a result, AlN can be used as a buffer layer to avoid the phonon leakage while strongly confining the optical wave at the same time. In addition, direct wafer bonding between silicon and AlN has been reported recently [40], which guaranteed the crystal qualities of both silicon and AlN.

In Chapter three, we take the advantage of AlN and utilize genetic algorithm (GA) to design a novel unsuspended silicon waveguide for enhanced stimulated Brillouin scattering. The platform is CMOS fabricatable and only requires single etching step. The optimized SBS gain reaches $2462W^{-1}m^{-1}$, which is 8 times larger than the recent result [37]. The details are discussed in Chapter three.

2.2 On-chip temperature sensing

On-chip temperature sensing relies on the temperature-dependent properties of optical components or structures integrated on the chip. Changes in temperature alter

these properties, leading to variations in the optical signals or parameters that can be measured and correlated to temperature changes.

There are different approaches to achieving on-chip temperature sensing. One common method involves utilizing the thermal dependence of the refractive index in waveguides or resonators[49]. Changes in temperature cause variations in the effective refractive index, which can be monitored through changes in the optical transmission or resonance characteristics. Other techniques include using temperature-sensitive materials[50] or incorporating micro-thermal sensors directly on the chip [51].

on-chip temperature sensing provides compact, integrated, and scalable solutions for temperature monitoring in a variety of applications. However, it still faces challenges such as accuracy, detection range and cross-sensitivity to other environmental factors. Novel sensing mechanisms and materials, as well as enhanced signal processing algorithms, are desired to improve the accuracy, sensitivity, and reliability of on-chip temperature sensors. Here, we propose two novel PICs for temperature sensing. One takes the advantages of both distributed optical fibre sensing (DOFS) and PIC and achieves ultra-high spatial resolution. The other one utilizes the concept of mode localization in micro-electro-mechanical system (MEMS) and realizes ultra-sensitive temperature sensing.

2.2.1 Distributed optical fibre sensing

The distributed optical fibre sensing (DOFS) is a technique that can measure the physical parameters along the fibre distributively. Unlike traditional fibre senors that only measure at specific positions, DOFS can continuously measure the physical parameters on the entire optical fibre [10].

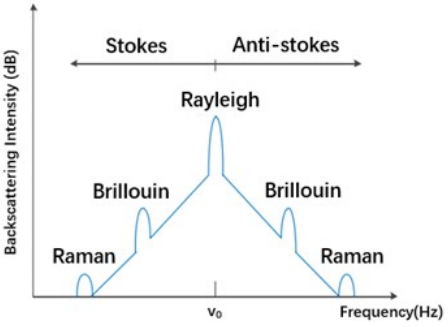

Figure 2.1: Typical spontaneous scattering spectrum from solid state matter

When a high-power laser is incident into the optical fiber, the light scattering occurs with a random statistical process in all angular directions [52]. The spectrum of these scattering is illustrated in fig. 2.1, which includes Rayleigh, Brillouin and Raman scattering. Rayleigh scattering is the strongest scattering process, which comes from

the elastic scattering between the incident light and the scattering center (formed by the random fluctuation of optical fiber density). The most prominent feature is that the frequency of the scattered light is equal to the frequency of the incident laser. Raman scattering is an inelastic scattering, which is derived from the inelastic collision between the incident light and the optical phonon, and generates a new frequency component, where the frequency less than the incident light is called Stokes light, and the frequency greater than the incident light is called anti-Stokes light. Brillouin scattering is also an inelastic scattering, which comes from the inelastic collision between the incident light and the acoustic phonon. The mechanism of Brillouin scattering can be regarded as the Doppler effect of the incident light on a moving grating, which produces a frequency shift component that is different from the frequency of the incident light.

Based on different scattering schemes, massive optical fibre sensing systems are available for extracting temperate and strain information, including the optical frequency domain reflectometer (OFDR)[25], the Brillouin optical time domain reflectometry (BOTDR)[53], the Brillouin optical time domain analysis (BOTDA)[10], etc. Due to the flexibility and multi-point measurable features of DOFS, it has been widely used for the safety monitoring of batteries[54], gas pipelines[55], tunnels[56], etc.

The performance of a DOFS system can be evaluated by the following parameters: spatial resolution, sensing resolution, sensing distance and measurement time. The sensing resolution is the minimum detectable wavelength-shift casued by external environment changes. The spatial resolution refers to the smallest distance between two adjacent points that the sensing system can distinguish. Typical DOFS system such as OFDR can reach very high spatial resolution with the order of μm [11]. The sensing distance is the maximum detectable distance that a system can reach, which is dependent on the laser source. The measurement time is the time required for DOFS to produce corresponding output, various data processing techniques and data acquisition approaches can be used to improve the data processing effectiveness, which significantly reduce the measurement time.

However, these systems cannot escape the complexity and high cost of the optical circuits required. The emergence of photonic integrated circuits (PIC) could change this picture. By spreading the cost of a mass production facility across a wide range of market applications, it is possible to achieve relatively cheap, complex optical chips that could replace much more expensive, piece-by-piece optical systems [53].

Among all DOFS, OFDR system is the one that is all set up by passive optical components, which makes it easier to be monolithically integrated [25]. Despite its simplicity, it still have high sensitivity, measurement distance and spatial resolution [57]. OFDR is a powerful tool for distributed measurement, capable of accurately

measuring reflection [58], temperature[11], strain[11], stress[59], pressure [60] and 3D shape[61].

Therefore, we take the advantages of both OFDR and PICs to design an integrated OFDR system using silicon photonics technology on an SOI platform. The integration of the system on an SOI platform offers advantages such as high integration density, reduced power consumption, and compatibility with standard complementary metal-oxide-semiconductor (CMOS) technology. The details are discussed in Chapter four.

2.2.2 Mode localization sensing

The phenomenon of the mode localization is widely utilized in coupled micro-electro-mechanical system (MEMS) resonators [62]. When two identical resonators are weakly coupled, the perturbation of a small stiffness or mass in one resonator will result in the uneven distribution of the vibration energy of the whole system [62, 26]. The unevenly-distributed energy is reflected by the resonant amplitude, which is strongly dependent on the magnitude of the perturbation. Compared with measuring the resonant frequency shifts in resonators, measuring the amplitudes variations of eigenstates caused by vibration localization in weakly coupled resonators provides two unique advantages for sensing applications. Firstly, The parametric sensitivity in terms of variation rate is enhanced by at least three orders of magnitudes [62, 26, 27, 63, 64, 65]. Secondly, the intrinsic common mode rejection due to the differential measurement techniques significantly reduces the impact of the environmental perturbations, which leads to better temperature stability [65, 66].

2.2.2.1 Mechanical mode localization

MEMS (Micro-Electro-Mechanical Systems) represents tiny devices that combine electrical and mechanical components on a very small scale, typically ranging from a few micrometers to millimeters in size. Its main advantages include small size, low power consumption, low cost, integration, etc. These advantages make MEMS technology attractive for a wide range of sensing applications such as accelerometers [67], gyroscopes [68], pressure sensors [69], microphones [70],etc.

Among all MEMS-based sensing method, resonant sensing is a promising technique used for sensing various physical quantities such as mass, strain, gravity, etc [71]. In resonant MEMS sensor, the microstructure is designed to have a specific resonant frequency that will change in response to the external measurand. This change in frequency can be measured and used to determine the magnitude of the measurand

changes. Resonant sensing provides high sensitivity, as even small changes in resonant frequency can be measured accurately. Also, it can provide a wide dynamic range, allowing the sensor to measure a broad range of measurands such as strain, temperature, mass, etc[71].

Also based on resonant-MEMS sensing, the proposal of mode localization has increased the sensitivity of resonant-MEMS sensors by over three orders of magnitude [62, 26, 27, 63, 64, 65]. The phenomenon of the mode localization was first studied in 1958 [72]. It describes that for a symmetric systems, all the mechanical modes vibrate with the same frequency and amplitude. When a small perturbation is induced, the symmetry of the system will be broken, which causes the mechanical vibrations to become localized in certain regions [73]. This phenomenon has been used to design MEMS resonator sensor with high sensitivity.

Compared to traditional resonant-MEMS sensing that only use one resonator, mode-localization-based MEMS sensor uses two identical resonators that are weakly coupled. Instead of measuring frequency shift, the vibration amplitude of the resonators are measured according to the external measurand. The sensitivity is improved by over three orders of magnitude compared with the traditional MEMS resonator sensor based on frequency shift [62, 26, 27]. In addition, compared with measuring the response of a single resonator, mode-localization-based MEMS sensor measures relative amplitude changes between resonant modes. This effectively reduces the common mode signals, which reduces the influence of noise and improves the sensor stability [65, 66].

2.2.2.2 The model of mechanical mode localization sensing

The behavior of the mode-localization-MEMS sensor is similar to a 2-DoF (Degree of Freedom) oscillator with spring (K), mass (M) and damping (C), which is shown in fig. 2.2. In this system, the stiffness (K_0), damping (C) and mass (M_0) of each resonator is equal to ensure that a symmetric system is generated, K_c is the spring connected with the two resonators, which is small in the condition of weak coupling. Any tiny perturbations to the stiffness of the spring or mass will break the symmetry of the system.

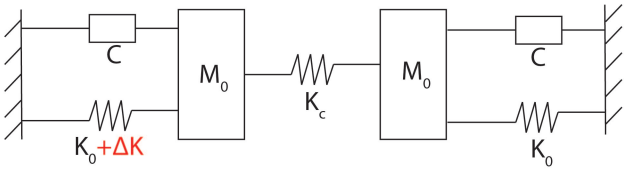

Figure 2.2: The model of a mechanical-coupled-ring resonators. It is represented by a 2-DoF system that is connected by dampers, springs and mass. Any small perturbations in stiffness or mass will break the symmetry of the system.

The equations of motion for the system can be expressed as [74]:

$$\begin{cases} M_0\ddot{x}_1(t) + C\dot{x}_1(t) + (K_0 + \Delta K)x_1(t) + K_c(x_1 - x_2) = F_0(t) \\ M_0\ddot{x}_2(t) + C\dot{x}_2(t) + K_0x_2(t) + K_c(x_2 - x_1) = F_1(t) \end{cases} \tag{2.9}$$

where x_1 and x_2 represent the displacements of the mass M_0 in the two resonators, respectively. ΔK represents a tiny stiffness perturbation added to one of the resonator. Then, the transfer functions that describe the relation between the mass displacements (x_1 and x_2) and forces (F_0 and F_1) can be expressed as:

$$T_1 = \frac{X_1(j\omega)}{F_0(j\omega)} = \frac{-\omega^2 M_0 + (K_0 + \Delta K) + K_c}{\omega^4 M_0 - \omega^2(K_0 + \Delta K + K_c)M_0 + (K_0 + \Delta K + K_c)^2 - K_c^2} \tag{2.10}$$

$$T_2 = \frac{X_2(j\omega)}{F_1(j\omega)} = \frac{K_c}{\omega^4 M_0 - \omega^2(K_0 + \Delta K + K_c)M_0 + (K_0 + \Delta K + K_c)^2 - K_c^2} \tag{2.11}$$

Eq. 2.10 and Eq. 2.11 are the transfer functions for each resonators. The corresponding characteristic equation is represented by the denominator of Eqs. 2.10 and 2.11:

$$\omega^4 M_0 - \omega^2(K_0 + \Delta K + K_c)M_0 + (K_0 + \Delta K + K_c)^2 - K_c^2 = 0. \tag{2.12}$$

The solutions of Eq. 2.12 are the mode frequencies of the two resonators, which can be given as:

$$\omega^{\pm} = \frac{(K_0 + \Delta K + K_c)2M \pm \sqrt{(2K_c^2 + \Delta K) - 4K_c\Delta K}}{2} \tag{2.13}$$

where ω^+ and ω^- are called in-phase mode frequencies and out-of-phase mode frequencies, respectively [74]. In the system, the in-phase mode and out-of-phase mode are coupled with different coupling strengths, which means any perturbation induced to one of the resonator will break the symmetry of the coupling and results in different mode coupling ratios. As an example, fig. 2.3 shows the transmission spectrum of a 2-DoF-coupled-ring system based on Eq. 2.10. Initially, two modes are symmetrically coupled (Red line) when there is no perturbation induced ($\Delta K = 0$). Two resonant modes show equal amplitudes at the resonant frequencies. After the stiffness perturbation is induced ($\Delta K \neq 0$), the symmetry of the coupling between two modes are broken. As shown by the black line, it is observed that the amplitudes of both modes are changed. With different quantities of perturbation, the modal amplitude ratio between the two modes are changed, which can be used for high-sensitivity sensing.

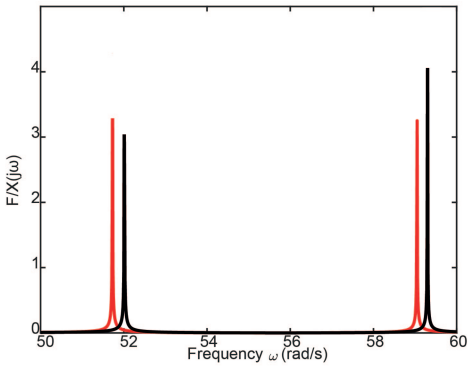

Figure 2.3: Transmission spectrum of the 2-DoF- coupled-ring resonators. $K_0 = 800$, $M_0 = 0.5$, $K_c = 20$, $C = 0.05$. Red line: $\Delta K = 0$. Black line: $\Delta K = 200$

In general, mode localization can be understood as the coupling between two vibration modes. Initially, the energy is evenly distributed to the two modes due to the symmetry of the system. Once the symmetry is broken, the energy distribution will become imbalanced, which leads to modal amplitude difference between the two modes. Actually, the same effect can also be observed in optical system.

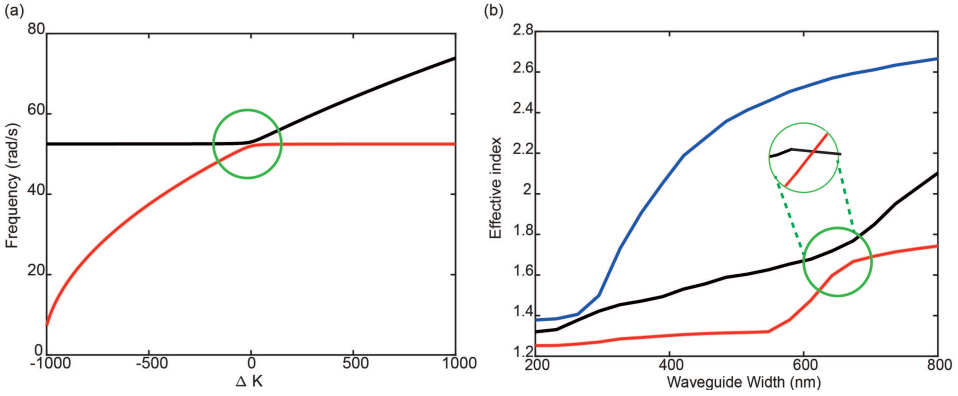

Figure 2.4: Mode couplings between MEMS system and optical waveguide. (a) Mode frequency curve veering in 2-DoF coupled resonators. Red line: out-of-phase mode. Black line: In-phase mode (b) Optical modes varying with waveguide width. Blue line: TE_{00} mode. Black line: TM_{00} mode. Red line: TE_{01} mode.

The mode coupling in MEMS system is characterized by the veering phenomenon [71]. The veering can be understood as a situation where the eigenvalues of the system moves away from each other as the level of disorder or perturbation in the system increases. In fig. 2.4 (a), the veering of the mode frequencies are varying with the change of stiffness perturbation (ΔK). At $\Delta K = 0$, the system reaches 100 % symmetry and two modes are evenly coupled. The same phenomenon is also observed in a optical waveguide. As shown in fig. 2.4 (b), for a 220-nm-height strip waveguide based on SOI platform, TE_{01} mode and TM_{00} are equally coupled when the width of the waveguide is 680 nm (green circle). As the waveguide width is increasing, TM_{00} mode is gradually converted to TE_{01} mode. The vertical axis shows the corresponding effect index of each mode. When the waveguide width continues to increase, the

effective index of TE_{01} keeps increasing and moves away from TM_{00} mode, which means mode energy is coupled from TM_{00} to TE_{01} mode.

In conclusion, mode localization can be observed in both MEMS and optical system. For MEMS system, the perturbation such as external changes of stiffness or mass will result in an uneven coupling between the in-phase mode and out-of-phase mode. For optical system, the changes in geometries will also affect the coupling between different waveguide modes. However, for optical strip waveguide, the mode localization effect is hard to be tuned because the geometries of the waveguide are difficult to be modified by external physical quantities. Therefore, an optical system that can amplify the effect of mode localization is needed.

Compared with MEMS resonators, optical resonators exhibit several advantages. Optical ring or disk resonators can achieve high quality factors without using vibration structures and vacuum conditions [28, 29, 30]. In addition, the resonance response in optical resonator is also very sensitive to the external condition changes. We believe the coupling between resonance modes in optical resonator also follows the effect of mode localization in MEMS system. Therefore, in chapter six, we start by studying the effect of the mode localization in optical ring resonators and design novel PIC temperature sensor.

2.3 Photonic inverse design

Traditional PICs are typically designed using manual parameter selection or semi-analytical models, resulting in nanophotonic devices with limited functionality (single function) and large footprints, often reaching hundreds of microns[75, 76]. This limitation highlights the potential benefits of nanophotonic devices with high densities, which can potentially merge photonics and electronics at the nano-scale. Recently, novel ultra-compact nanophotonic devices that employ inverse design algorithms achieve great success, the exhibited footprints are only a few microns in size [77, 78, 79, 80], some of them also achieve multi-functionalities[81].

Compared with traditional structures, the structures with inverse design algorithms can search full parameter space. These algorithms provide significantly increased degree of design freedom, which ultimately allows for the maximization of device performance. We believe that with the rapid progress being made in inverse design algorithms, coupled with the improvement of nano-fabrication, the nanophotonic devices with inverse design algorithms will play a key role in the development of PIC.

Therefore, For each PIC, we utilize different photonic inverse design algorithms for the optimization of the optical components. Generally, the inverse design algorithms can be categorized into four groups: Brute-force searching, Heuristic optimization

algorithms, Gradient-based algorithms and deep learning. The main purpose of these algorithms is to achieve an optimized refractive index distributions within the design area, which in turn satisfies the specific design requirements. In the following sections, each algorithm will be discussed one by one.

2.3.1 Brute-force searching

2.3.1.1 Direct binary search

Direct binary search (DBS) is the most frequently-used method in Brute-force searching. It was first introduced in 1987 [77], and was first applied to nanophotonic design by Bing Shen in 2015 [78]. In this method, the device is discretized into pixels, the initial state of these pixels can be either randomly generated or specifically designed. Next, a single pixel is randomly selected and its state is flipped. The corresponding figure of merit (FOM) that evaluates the performance of the device is then calculated. If the FOM has improved compared to the original value, the state of the flipped pixel will be retained. Otherwise, the pixel will return to its previous state, indicating that the device's performance has not been enhanced. This process is shown in fig. 2.5(a). One iteration finishes when all the pixels are inspected, and the iterations will stop when the FOM stops growing.

Due to its simplicity and wide range of applications, many photonic devices have been designed using DBS algorithm, such as mode converter [79, 80] (fig. 2.5(b-c)), polarization rotator [82] (fig. 2.5(d)), power splitter [83] (fig. 2.5(e)), wavelength demultiplexer [84] (fig. 2.5(f)), waveguide crossing [85] (fig. 2.5(g). Besides the device with single function, researches also design a multi-functional device using a modified DBS algorithm. Each pixel is rotatable so that one more design freedom is added, the device achieves mode conversion and power splitting simultaneously.

In fig. 2.5(d,e,g), photonic-crystal (PhC)-like nano-hole pixels replace the original square piexl, this suppress the lag effect caused by reactive ion etching (RIE) [2]. RIE lag refers to the dependence of the etching rate on the feature size. A smaller feature size results in a shallower etching depth during a single etch process, which is the most common and typical fabrication error in the plasma etching process [86]. Proposed devices show that PhC-like structures is in-sensitive to the RIE lag and therefore improve the fabrication tolerances.

However, due to the intrinsic pixel-by-pixel scanning feature of the DBS algorithm, the optimization process will be high-likely stuck into a local-maximum solution. The effect of this issue can be reduced by parallel computations starting with different initial patterns [87], but this will also induce high computational costs. Therefore, it is better suited for the optimizations within a limited parameter space.

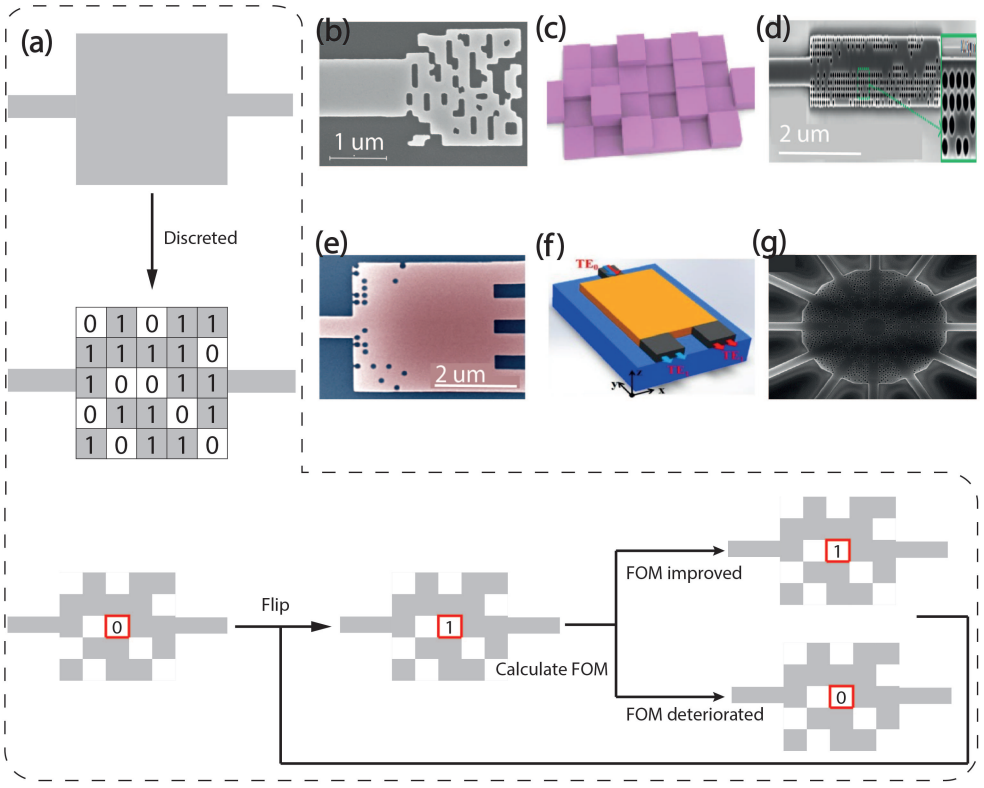

Figure 2.5: (a) Illustration of the DBS algorithm. (b)-(f) Nanophotonic devices that using DBS method. (b,c)Mode converter [79, 80]. (d) Polarization rotator [82]. (e) Power splitter [83]. (f) Wavelength demultiplexer [84]. (g) Waveguide crossing [85].

2.3.2 Heuristic optimization algorithms

2.3.2.1 Genetic algorithm

Genetic Algorithm (GA) is a computational model of biological evolution that simulates the natural selection and Genetic mechanism of Darwinian biological evolution. It is a method to search for the optimal solution by simulating the natural evolution process [88]. The GA process is shown in the fig. 2.6(a-left), which can be summarized in six steps:

Step 1: Randomly generate a population as the initial solution of the problem (usually, the initial solution may differ greatly from the optimal solution, which is tolerable, as long as the initial solution is randomly generated to ensure the diversity of individual genes);

Step 2: Find a suitable encoding scheme to encode the individuals in the population. Common encoding schemes such as floating point encoding or binary encoding can be selected (it should be pointed out that different encoding schemes directly affect the implementation details of subsequent genetic operators).

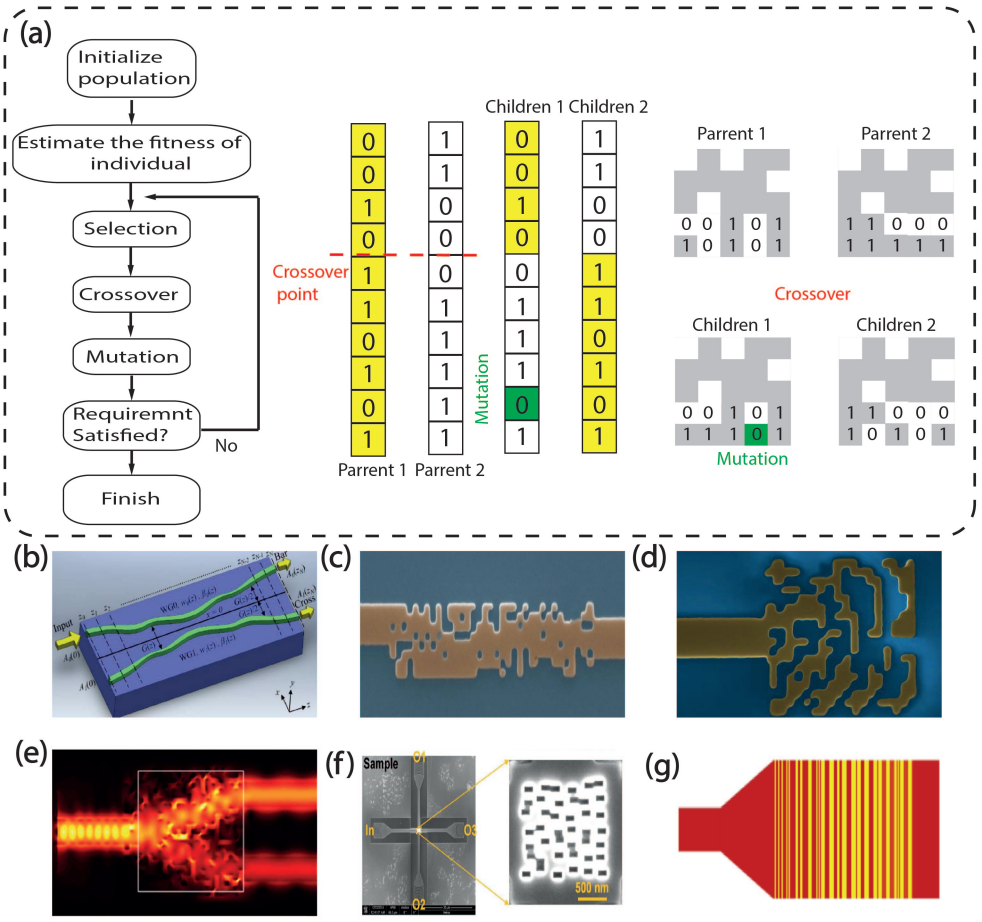

Figure 2.6: (a-left) Illustration of GA process. (a-right) GA process for nanophotonic design. (b)-(g) photonic applications based on GA: (b) Waveguide coupler[1]. (c) Polarization rotator [89]. (d) Reflector [90]. (e) Power splitter [91]. (f) Wavelength router [92]. (g) Grating coupler [93]

Step 3: Take the function value of multi-peak function as the fitness of individuals, and calculate the fitness of each individual in the population (the calculated fitness will provide basis for subsequent individual selection);

Step 4: Select the parent bodies to participate in reproduction according to the fitness level. The selection principle is that the higher the fitness level is, the more likely the individual will be selected (thus continuously eliminating the individual with lower fitness level).

Step 5: Carry out genetic operation on the selected parent bodies, that is, copy the genes of the parent bodies and use crossover, mutation and other operators to produce offspring (on the basis of retaining excellent genes to a large extent, mutation increases the diversity of genes, thus improving the probability of finding the optimal solution).

Step 6: According to certain criteria, decide whether to continue the algorithm or find out the individual with the highest fitness among all descendants as the solution to

return and end the program (criteria can be solution threshold, the specified number of iterations, etc.).

GA has been widely used in the field of communication for optimizing radar and antenna structures [94]. In recent years, this computational technique has been introduced into the inverse design of nanophotonic devices [1, 89, 90, 91, 92, 93, 88, 94].

For GA-based nonaphotonic design, the encoding scheme is basically binary encoding, the value can be either '0' (represents an etched pixel) or '1' (represents an unetched pixel). As shown in fig. 2.6 (a-right), the initial population is randomly generated, each individual contains an array of '0' '1' distribution, the length of each array equals the total number of pixels. After that, a fitness function evaluating the performance of the individual is calculated, the higher the score is, the higher chance that the individual will be selected for the next generation. During the crossover section, each individual of the selected population is assigned a specific or random probability to undergo crossover with another member, the crossover point is selected randomly. After crossover, the new generated children will replace the parents, and each of them will have a possibility to mutate, which means randomly-selected pixels are flipped. After that, the new generation are formed and each individual will go back to the fitness evaluation to form a complete loop. The iteration will stop when the requirement is satisfied.

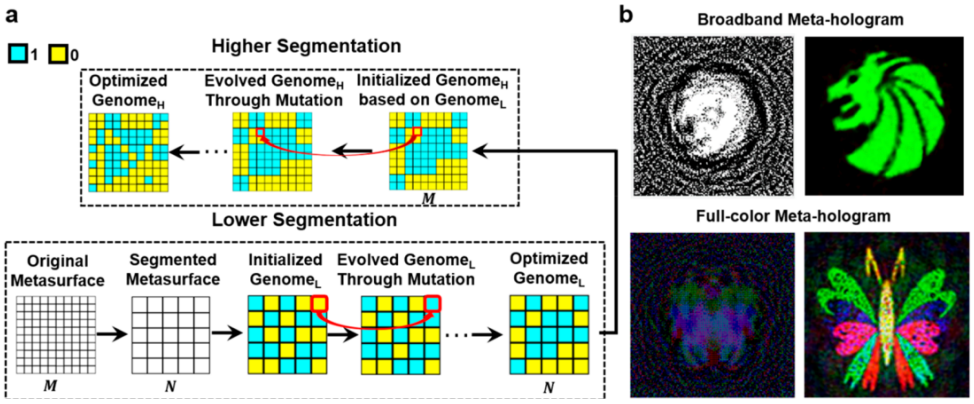

Figure 2.7: Description of segmented hierarchical evolutionary algorithm (SHEA) [95].

Compared with DBS, GA is eligible for designing in large parameter space, which is more suitable for complex and multi-objective photonic design. Fig. 2.6(b) displays a GA-optimized waveguide coupler on the silicon-on-insulator platform, it achieves arbitrary coupling ratios over a broadband wavelength range (100 nm at the central wavelength of 1580 nm), the maximum deviation is only 2%[1]. As shown in fig. 2.6(c-g), GA is also extended to cover a wide range of photonic applications, such as polarization rotator [89], reflector [90], power splitter [91], wavelength router [92] and grating coupler [93].

Genetic algorithm does not rely on the initial patterns, so it can automatically find the global optimal without initially-manual intervention. Based on this feature, it is often used to design devices with unknown initial patterns. Fig. 2.7 shows a segmented genetic algorithm, which is utilized to optimize large-scale structures. The metasurface is composed of many pixels, each pixel contains two states of ”1” and ”0”, where the ”1” state indicates that the pixel contributes to the far-field diffraction pattern, and the ”0” state represents that no light from that pixel can contribute to the diffraction pattern of the device. In the first stage, the entire metasurface is divided into sections of equal size, and then the pixels in each small section are mutated (i.e. switch between ”0” and ”1”) to satisfy the fitness function. When the fitness function of the first stage meets the convergence conditions, the final optimization results of the first stage are integrated and used as the initial structure of the second stage. In the second stage, the entire metasurface are mutated until the optimal result reaches the threshold.

This method significantly improves the speed of GA for designing large-scale photonic devices. Although the GA performs well in the design of photonic devices, it still has problems, such as limited optimization variables, sensitive optimization parameters, long optimization time, etc. When multiple variables are optimized, it is difficult for the GA to obtain ideal results. At the same time, GA is very dependent on the parameter settings, such as the population size, the mutation rate, etc. Therefore, in the optimization of large-scale structures, topology optimization are still more popular, which will be discussed later.

2.3.2.2 Other algorithms

in addition to GA, other heuristic optimization algorithm such as particle swarming optimization (PSO) is also applied to design nanophotonic devices. PSO optimization is a technique that involves a population of candidate solutions (particles) moving in the search space towards the best position, referred to as the global optimum. This process continues until the desired FOM is satisfied [96, 97, 98]. The idea of particle swarm algorithm is similar to genetic algorithm, but the difference between them is that in particle swarm algorithm, each particle will search for the optimal solution individually in the parameter space, and update its velocity and position based on the individual and global optimum values of the fitness function. Many photonic devices are designed based on PSO algorithm, such as 2×2 power splitters [99], polarization beam splitter [100], grating couplers [101],etc. In [101], The amorphous silicon grating optimized by particle swarm algorithm can achieve broadband and polarization-insensitive light coupling in the visible light range, with an absorption efficiency of over 80%.

on the other hand, the simulated annealing algorithm is also found to be an efficient way for the photonic design. In [102], researchers combined simulated annealing and GA to optimize a structure of an ultra-broadband twisted light emitter, which is an essential component for the orbital angular momentum (OAM) communication devices [103, 104].

However, the limitations of these heuristic optimization algorithms are similar, including the number of variables, parameter settings, and computational time. Therefore, when optimizing a small number of variables, heuristic optimization algorithms can guide the direction of parameter optimization, but for the optimization problems with high degree of design freedom, more efficient and flexible design methods are still needed.

2.3.3 Gradient-descent based algorithm

For an initial structure, a common inverse design process can be summarised by three steps: 1. Calculate the corresponding FOM using numerical simulation. 2. Updates the structure through the feedback of the FOM. 3. iterate the above process multiple times to achieve the optimized structure design. In gradient descent algorithms, the gradient information of the FOM is calculated to provide a feedback for the optimization. Compared with heuristic optimization algorithms, the pixels to be optimized for gradient-descent based algorithms are significantly small, which provide tremendous degrees of design freedom. However, this seems impossible for traditional optimization process because each pixel requires one simulation to get the gradient information, the computational cost will be significantly high if using this one-by-one calculation. To tackle this problem, the gradient-based topology optimization (TO) is introduced [105]. TO uses adjoint methods to obtain the gradient information, it is feasible for systems consisting thousands or millions of pixels because it only needs two simulations for each iteration [32].

2.3.3.1 Topology optimization

Topology optimization was introduced in 1988 [106], it allows the permittivity distribution in the design region to adopt arbitrary topological geometries [107]. TO is eligible to manipulate light at a subwavelength scale sine the discrete pixels in the design can be reduced to any extent. In addition, the gradient information of the objective function is considered, leading to strong directional control during the optimization.

2.3.3.2 Adjoint method

Calculating the gradient information is the fundamental difficulty for TO because each pixel needs to perform one simulation, which is extremely inefficient. Fortunately, the emergence of adjoint method effectively solved this problem. By using adjoint method, only two simulations are needed (forward simulation and adjoint simulation [108]) to obtain the gradients of all the parameters.

Adjoint method has been widely used in the optimization of some linear problems such as fluid dynamics, particularly for aeronautical applications [109], etc. In photonic design, much of the electric field distribution is solved linearly by Helmholtz equations. The frequency domain Helmholtz equation can be expressed as:

$$\nabla^2 \times \boldsymbol{E} - \omega^2 \epsilon \mu_0 \boldsymbol{E} = -j\omega\mu_0 \boldsymbol{J} \tag{2.14}$$

where $\boldsymbol{E}$ is the electric field, $\boldsymbol{J}$ is the current density, ϵ is the permittivity, μ_0 is the permeability in free space and ω is the frequency. The optimization problem in photonic design is to find an optimal permittivity distribution $\epsilon(\boldsymbol{r})$ that can minimize the objective function $f(\boldsymbol{E})$ related to the electric field $\boldsymbol{E}$ [108]. To use adjoint method, the Helmholtz equation must convert to the form of linear algebra:

$$\nabla^2 \times \boldsymbol{E} - \omega^2 \epsilon \mu_0 \boldsymbol{E} = -j\omega\mu_0 \boldsymbol{J} \rightarrow A(z)x = b \tag{2.15}$$

Therefore the following transformations are made:

$$\boldsymbol{E} \rightarrow x \tag{2.16}$$

$$-j\omega\mu_0 \boldsymbol{J} \rightarrow b \tag{2.17}$$

$$\nabla^2 \times -\omega^2 \epsilon \mu_0 \rightarrow A(z) \tag{2.18}$$

$$\epsilon(\boldsymbol{r}) \rightarrow z \tag{2.19}$$

For an objective function $f(x)$, its gradient with respect to the permittivity distribution $\epsilon(\boldsymbol{r})$ can be expressed by using the chain rule:

$$\frac{df}{dz} = \frac{df}{dx} \cdot \frac{dx}{dz} \tag{2.20}$$

where $\frac{dx}{dz}$ can be obtained by taking the derivative of both side of Eq. 2.15 with respect to the permittivity distribution z:

$$\frac{\partial A}{\partial z_i}x + A\frac{\partial x}{\partial z_i} = \frac{\partial b}{\partial z_i} \rightarrow \frac{\partial x}{\partial z_i} = A^{-1}(\frac{\partial b}{\partial z_i} - \frac{\partial A}{\partial z_i}x) \tag{2.21}$$

Then,

$$\frac{dx}{dz} = [\frac{\partial x}{\partial z_1} \cdots \frac{\partial x}{\partial z_n}] = A^{-1}([\frac{\partial b}{\partial z_i} \cdots \frac{\partial b}{\partial z_n}] - [\frac{\partial A}{\partial z_1}x \cdots \frac{\partial A}{\partial z_n}x]) \tag{2.22}$$

The gradient of $f(x)$ becomes

$$\begin{aligned} \frac{df}{dz} &= \frac{df}{dx} \cdot \frac{dx}{dz} \\ &= \frac{df}{dx}A^{-1}([\frac{\partial b}{\partial z_i} \cdots \frac{\partial b}{\partial z_n}] - [\frac{\partial A}{\partial z_1}x \cdots \frac{\partial A}{\partial z_n}x]) \\ &= (A^{-T}\frac{df}{dx}^T)^T([\frac{\partial b}{\partial z_i} \cdots \frac{\partial b}{\partial z_n}] - [\frac{\partial A}{\partial z_1}x \cdots \frac{\partial A}{\partial z_n}x]) \end{aligned} \tag{2.23}$$

In Eq. 2.23, $\frac{\partial b}{\partial z_i} = 0$ because b is independent to the permittivity distribution (it can be seen from Eq. 2.17). Finally, Eq. 2.23 can be simplified as:

$$\frac{df}{dz} = (A^{-T}\frac{df}{dx}^T)^T[\frac{\partial A}{\partial z_1}x \cdots \frac{\partial A}{\partial z_n}x] \tag{2.24}$$

The gradient of $f(x)$ can then be solved by running two simulations. One is the forward simulation to solve the second term of the right-hand-side of Eq. 2.24:

$$[\frac{\partial A}{\partial z_1}x \cdots \frac{\partial A}{\partial z_n}x] \rightarrow (\nabla^2 \times -\omega^2\epsilon\mu_0)\boldsymbol{E} \tag{2.25}$$

The forward simulation uses the incident light as the source, and it has the following relation:

$$(\nabla^2 \times -\omega^2\epsilon\mu_0)\boldsymbol{E} = i\omega\mu_0\boldsymbol{J} \tag{2.26}$$

The other one is the adjoint simulation to solve the first term of the right-hand-side of Eq. 2.24:

$$(A^{-T}\frac{df}{dx}^T)^T \rightarrow (\nabla^2 \times -\omega^2\epsilon\mu_0)\boldsymbol{E_{adj}} \tag{2.27}$$

The adjoint simulation uses the derivative of the objective function with respect to electric field $\boldsymbol{E}$ as the source, it has the following relation:

$$(\nabla^2 \times -\omega^2 \epsilon \mu_0) \boldsymbol{E_{adj}} = (\frac{\partial FOM}{\partial \boldsymbol{E}})^T \tag{2.28}$$

Finally, the gradient of the objective function with respect to the permittivity distribution is solved by combining the forward simulation and the adjoint simulation. As shown in fig. 2.8, the electric fields $\boldsymbol{E}$ and $\boldsymbol{E_{adj}}$ are obtained by the forward simulation (left) and adjoint simulation (right), respectively. The gradient information at a certain point is

$$\frac{dFOM}{d\epsilon} \propto Re[\boldsymbol{E}(\boldsymbol{x}) \cdot \boldsymbol{E_{adj}}(\boldsymbol{x})] \tag{2.29}$$

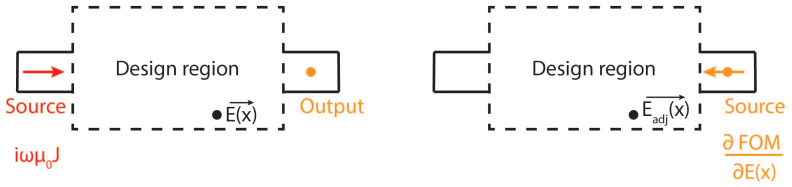

Figure 2.8: Schematic of the adjoint method: Forward simulation and adjoint simulation are needed for each iteration. The forward simulation uses incident light as the source and the adjoint simulation uses the derivative of the objective function as the source.

2.3.3.3 Optimization process

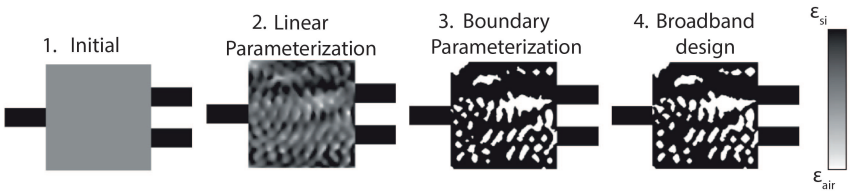

Figure 2.9: Overview of the TO process [110]

A typical optimization process for TO is shown in fig. 2.9. To start with, the permittivity distribution of the design region is randomly set, the value of the permittivity in the area can be changed continuously within in the range between ϵ_{Si} and ϵ_{air}, where ϵ_{Si} is the permittivity of Si and ϵ_{air} is the permittivity of air. Then the FOM is calcualted based on the permittivity value, the gradient information is obtained by adjoint method, which is used to adjust the permittivity value of each pixel according to the gradient. After that, the updated continuous permittivity values are binarized, which means only ϵ_{Si} or ϵ_{air} can be choosen. The FOM is re-calculated after the binarization, The iteration continues towards the direction of gradient descent, and will stop when FOM satisfies the requirement.

The result obtained by gradient-descent based algorithms is the local maximum within the parameter range. It will be more easily converge to the global optimum if a reasonable initial structure can be given. From fig. 2.9, it can be seen that the inverse-designed structure based on gradient-descent algorithms has an abstract pattern distribution, which is difficult for human to design directly.

2.3.3.4 Photonic applications based on TO

Initially, the studies of TO are most linear devices, which satisfies the Hermitian condition [32]. These studies include Y-branches with arbitrary power splitting ratios [111], wavelength (de)multiplexer [112, 110], wavelength demultiplexing grating coupler [113], single-mode 3 dB power divider [114], 90° bends [115], mode converter [116], metagratings [117],etc.

In [117], the authors designed a Large-angle, multi-functional metagrating by using TO, which is shown in fig. 2.10 (i). During the optimization, an initial random-continuous distribution is used, the gradient is calculated using forward simulation and adjoint simulation. The permittivity of each pixel is updated multiple times to optimize the deflection efficiency of the entire structure. Compared with other diffraction gratings, the TO-optimized gratings exhibit extremely high efficiency in large-angle deflection (40° to 80°).

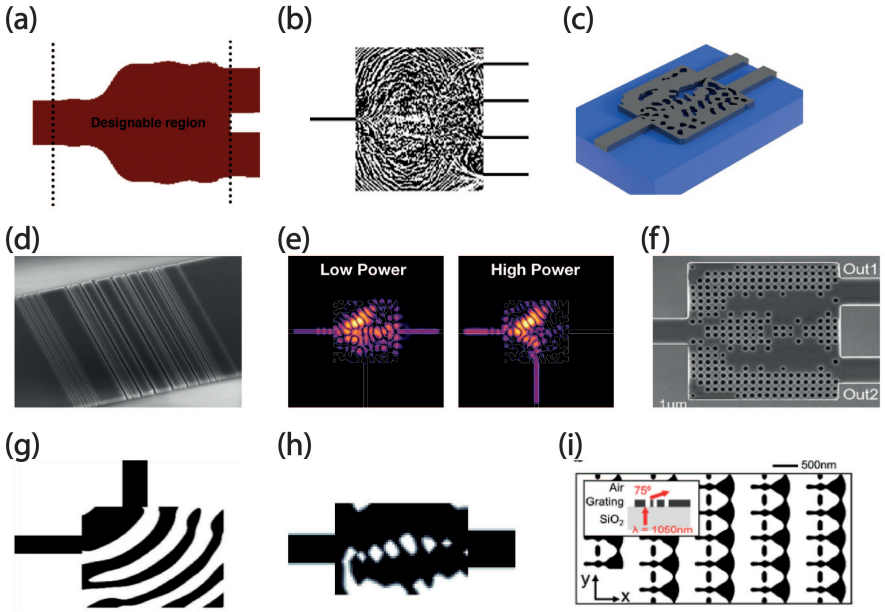

Figure 2.10: Inverse designed photonic devices using TO: (a)Y-branches with arbitrary power splitting ratios [111], (b,c) Wavelength (de)multiplexer [112, 110], (d) Wavelength demultiplexing grating coupler [113], (e) Power switch [118], (f) Single-mode 3 dB power divider [114], (g) 90○ bends [115], (h) mode converter [116], (i) metagratings [117].

Although the TO has been used in the design of many photonic devices, the forward simulation and adjoint calculations in the algorithm will still increase the optimization time, especially for large-scale photonic devices. Even if using GPU acceleration, the method still cannot compress the optimization time to an ideal range. In [119], the authors effectively solved this problem by using segmented optimization method. As shown in fig. 2.11, the required phase distribution is discretized into a series of linear parts under the wavelength scale. Then each part is designed separately using TO so that the phase distribution of each part approaches to the expected value. Finally all the optimized elements are combined to form the complete structure. It was found that the segmented optimization method can be used to generate millimeter-scale topology-optimized metasurfaces in a day (using a personal laptop), while the conventional optimization takes about a year.

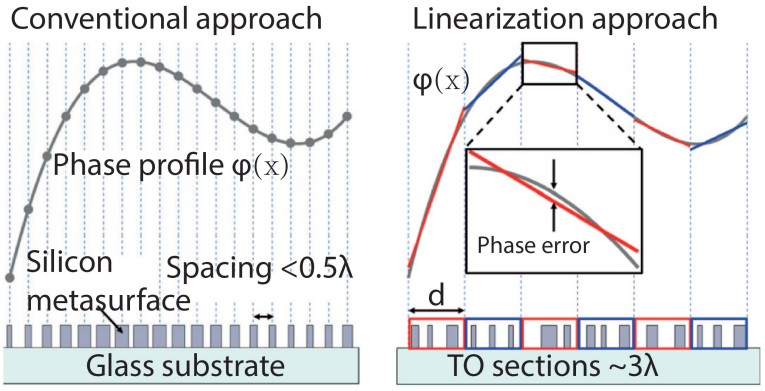

Figure 2.11: Introduction of the section optimization method based on TO [119]

2.3.4 Deep learning

The design of nanophotonic devices often relies on time-consuming electromagnetic simulations. The most commonly used methods are Finite difference time domain method (FDTD) and Finite Element Method (FEM). Nanophotonic devices usually contain multiple structural parameters, designers need to continuously use algorithms to simulate and iterate each parameter until a satisfactory structure is obtained. This is the well-known forward design process. Obviously, this is a long process. For given input structure parameters, can we build a model that can avoid time-consuming electromagnetic simulation, and directly output the predicted results? Or for a given optical spectrum expected by the user, can a model directly output the structure corresponding to that spectrum? Even, given user-defined responses, let the model generate structures with arbitrary shapes. With the development in the deep learning for photonic inverse design, all these ideas can be achieved. In deep-leaning-assist inverse design, the models can be categorized into two types: one is to predict the

optical spectrum according to the given input structure, the other one is to generate the corresponding structure using the given spectrum.

It is relatively easy for the model to predict optical response based on the given input structure parameters. Usually a fully-connected artificial neural network (ANN) is used to solve these problems. As shown in fig. 2.12 (a), the model contains an input layer, an output layer and multiple hidden layers. Each node in the input layer represents the parameter that needs to be trained, and each node in the hidden layer is connected to the node in the previous layer through a weighted connection. There are two propagation methods for information between layers, namely forward propagation and backward propagation. During forward propagation, each node accepts the output from the upper layer, and processes it through the logistic function, and continues to propagate to the next layer. In the backward propagation, the error between the results from the network and the real data is calculated by a cost function, and will be propagated backward based on the chain rule, which is used to update the weight of each node. The whole network is trained after a certain number of iterations.

Fig. 2.13 (a)-(c) show examples of using fully-connected ANN to train models for specific photonic applications. In fig. 2.13 (c), the authors proposed a model that can accurately predict the effective index and power confinement according to the input waveguide parameters (width, height and gap of a slot waveguide). The training set is obtained by using Comsol simulation, the model can directly predict the result once it is trained, which is several orders of magnitude faster than conventional design methods. In addition to predict single value, the ANN-optimized model can also predict spectrum [120] and image [121]. In fig. 2.13 (a), spectrum information consisting 81 wavelength points can be predicted according to the input parameters (height, diameter and period of the plasmonic metasurface). In fig. 2.13 (b), the model can predict the electric filed of a plasmonic nanoparticle. The comparison between the simulated and predicted electric filed is shown in the bottom of fig. 2.13 (b), which is totally the same.

ANN are often used to optimized the footprint of a structure with known shape and structure. Taking the optimization of multi-layer thin firm as an example [124] . The thin film consists multiple layers of silicon dioxide and silicon nitride, the goal of the optimization is to quickly obtain the thickness parameters of each layer for a given transmission spectrum distribution. However, during the optimization, there will be situations where multiple sets of thickness parameters correspond to one set of transmission spectrum. This is called one-to-many mapping problem, which results in hard convergence for the optimization [32]. Therefore, a tandem architecture is introduced [124], which is shown in fig. 2.12 (b). The model firstly fixes the weights between the structure parameters and the spectrum. Then it uses the structure parameters as the middle layer and spectrum as the input layer. The error between the target spectrum and the predicted spectrum are used to train the model. This method

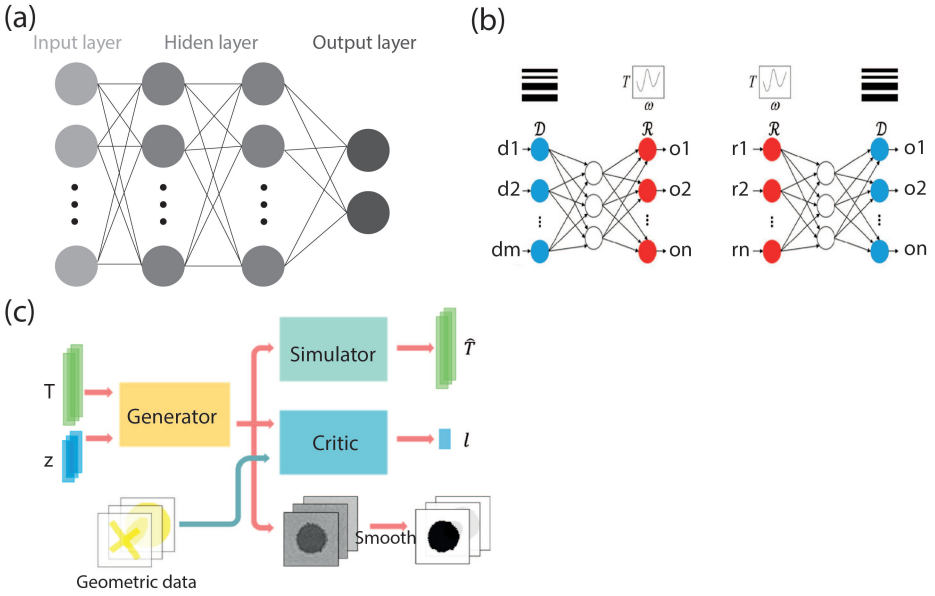

Figure 2.12: (a) Fully-connected ANN [120, 122, 123]. (b) Fully-connected tandem architecture [124]. (c) generative adversarial network (GAN) [125].

converts the mapping between spectrum and structure to the mapping between spectrum and spectrum, which improves the convergence of the network.

In the examples shown above, the models are based on a single structure, that is, for a given spectrum, the output structure is limited by the design parameters and it can not be any shapes. In [125], authors used generative adversarial network (GAN) to inversely design metersurfaces with arbitrary shapes. The model consists of a critic, a generator and a simulator. The term " adversarial" comes from the training process between the critic and the generator. The generator can generate arbitrary shapes according to the given input spectrum, the generated shape will then be judged by the critic, who has the actual shapes that required by users. The critic will give feedback to the generator for the updates of the required shapes until the generator outputs the required shapes. At the same time, the spectrum generated by the updated shapes from the generator will be compared with the predicted spectrum from the simulator, which is a trained model that can predict the spectrum according to a given shape. The error between the spectrum from the generator and the predicted spectrum from the simulator will be used to updates the generator until it can generate the required spectrum. Finally, the generator can generate arbitrary shapes that defined by users according to the input spectrum. Fig. 2.13 (e) shows the required spectrum defined by users (left), and the shape generated by the generator and its spectrum (right), respectively. This black irregular shape is evolved from multiple shapes from the critic.

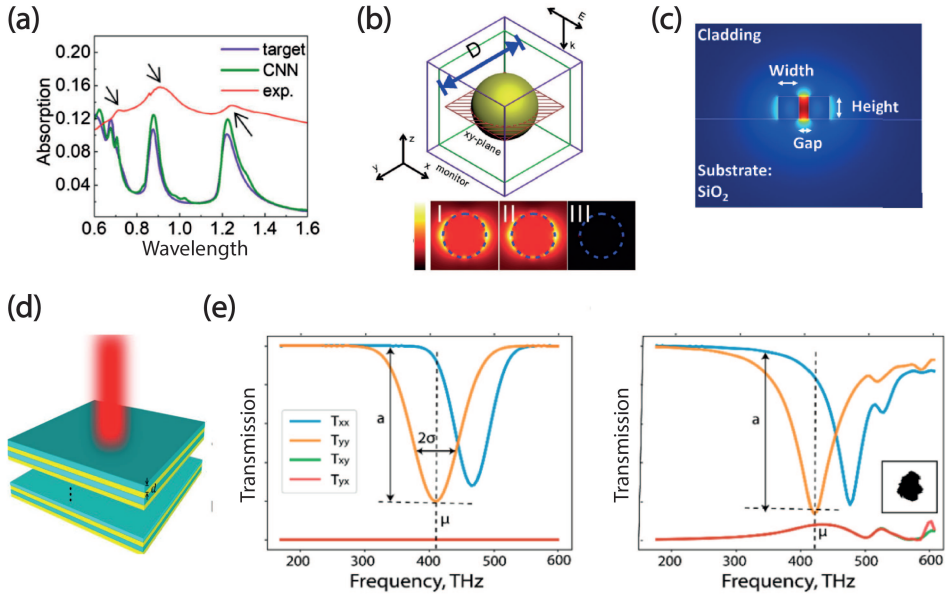

Figure 2.13: The photonic applications based on ANN. (a) Spectrum of a inverse-designed plasmonic metasurfaces based on convolutional neural network [120]. (b) Inverse-designed plasmonic nanoparticle and its electric field distribution [121]. (c) The nanophotonic waveguide by fully-connected ANN [122]. (d) A thin film composed of m layers of SiO_2 and Si_3N_4, the thicknesses are optimized by tandem ANN [124]. (e) Generating arbitrary-shapes metasurfaces using GAN [125].

2.3.5 Discussion

In this chapter, PICs in nonlinear optics, temperature sensing and a specific optimization approach for optical component design, which is the photonic inverse design, are discussed with typical examples. In nonlinear optics, typically in SBS, the SBS gain is increased by designing structures with specific parameters and materials. However, most of the structures are suspended to avoid mechanical leakage into the substrate, which increase the complexity of fabrication. Also, the release of the waveguide reduce the mechanical stability and thermal conduction, which increase the loss. Therefore, an unsuspended structure that also realizes high SBS gain is desired. In chapter two, a novel unsuspended silicon waveguide for enhanced stimulated Brillouin scattering is designed by using GA, which is CMOS fabricatable and only requires single etching step. The optimized SBS gain reaches $2462W^{-1}m^{-1}$, which is 8 times larger than the recent result [37].

In temperature sensing, the current on-chip temperature sensors still face challenges such as accuracy, detection range and cross-sensitivity to other environmental factors. New materials or sensing mechanisms are needed. In chapter three and five, two novel on-chip sensing systems which utilize DOFS and mode localization, respectively, are demonstrated, which exhibit high spatial resolution and ultra-sensitive sensing resolution.

As an optimization approach for components design, the photonic inverse design algorithms based on brute-force searching, heuristic optimization, gradient-descent based algorithms and deep learning are discussed with typical examples. The design of photonic devices based on intelligent algorithms is an innovation of traditional design methods. The so-called traditional design method is a general term for a class of methods that require artificial optimization of parameters. In practice, numerical simulations are often used to find the ideal geometric parameters of structures (or experimental tests). In order to improve the efficiency of simulation calculations, it is necessary to select appropriate simulation methods and select appropriate boundary conditions. After the model is built, the shape and parameters of the structure need to be optimized to get the ideal output. parameters that are optimized manually needs the simulation to sweep the full parameter range. So the calculation time is usually long, but the efficiency is fine when the parameter range is small.

gradient-descent based algorithms and heuristic optimization algorithms provide a direction for parameter optimization, so it is beneficial to accelerate the design of the structure. Although the model trained by deep learning can replace the numerical simulation process, the training process is not out of the physical model. It needs to learn from the extracted features of the simulated data sets (or experimental data sets). Therefore, the photonic inverse design method is an optimization of the traditional method, it is not independent from the physical model.

Traditional design methods are limited by structural periods, material distribution, calculation time, etc. The inverse design method can realize fast and high-degree-of-freedom parameter optimization in the full parameter space. It is more likely to obtain a structure close to the extreme performance. According to the analysis of the existing inverse-designed applications, the inverse design method is flexible, which means it can be changed with different optimization target, and it can also achieve multi-objective optimization.

However, there are still challenges for the photonic inverse design. Firstly, most inverse design algorithms become less efficient when dealing with large designing space [32, 126, 127, 128]. For brute-force searching, the optimization efficiency is greatly dependent on the number of pixels in the design area. For example, for a design area with 400 pixels, the time needed for brute-force searching to exhaust all the possibilities is $t \cdot 2^{400}$, where t is the time needed for one simulation. The heuristic algorithms also faces the same problem. When the number of input parameters becomes larger, the convergence will be significantly slow down, also even stuck in the local-maximum.

Secondly, although the optimized structure shows great performance, there still does not have sophisticated physical model to explain why the structure exhibits that result. The design parameters and the size of the design region are almost selected by

intuition, different initial patterns or sizes of the structures will have totally different performance even using the same method. A physical modal is needed to help with choosing appropriate parameters and size to design structures with ultimate performance. Therefore, when choosing an inverse design method, it is necessary to evaluate the calculation time and the number of design freedom.

Chapter 3

GA-optimized unsuspended silicon waveguide for enhanced stimulated Brillouin scattering

In this chapter, we propose Si-AlN-Sapphire platform for realizing large SBS gain without suspending the Si waveguide. We leverage the genetic algorithm to optimize the waveguide structure so that the SBS gain coefficient can be maximized. By limiting the maximum etching step to two during the GA process, a simple and fabricable non-suspended structure is obtained. The best gain coefficient comes from the forward SBS of fundamental TE-like mode with the value of $2462 W^{-1} m^{-1}$. This gain value is 8 times larger than the recent result [37]. Our platform can enable Brillouin-related phenomena in centimetre-scale waveguide. Our findings could pave the way toward large-area unreleased opto-mechanics on silicon.

One critical limitation of the unsuspended structure is the reduced Brillouin gain coefficient due to the sacrifice of the contribution from the moving boundary effect. Genetic algorithm (GA) has been used to develop novel structures for giant SBS gain coefficient [41]. However, most designs require complex fabrication processes, making them almost impossible to be fabricated.

Here, we apply the GA to optimize the core silicon waveguide structure to maximum the SBS gain coefficient. We limit the maximum etching step number to two so that the optimized structure is not too complicated to be fabricated. In the following part, the fundamental theory and the implementation of the GA will be introduced.

3.1 GA work flow

For a GA, there are typically five stages to consider: initial population, fitness function, selection, crossover and mutation. First our initial population consists of 100 random samples. We discrete each sample into a series of 50 nm $\times$ 50 nm squares with the properties corresponding to the material of that part. There are two reasons for this rasterized method: first 50 nm is possible to the lithographically pattern; second this method allows us to keep the same mesh for all mutated samples. Via this method, we are able to change the structure design without affecting boundary conditions for both optical and acoustical waves.

The optimization area is limited within the silicon layer with an area of $1\mu m \times 1\mu m$ to reduce the computational time. The maximum etching step number is limited to two so that the optimized structure is not too complicated to be fabricated.

Each sample is decided by an array with eight parameters. These parameters are: waveguide width W, waveguide height H, number of first etching #$EP1$, number of second etching #$EP2$, the first etching position EP1, the second etching position EP2, etch depth for first etching ED1, and etch depth for second etching ED2. Fig. 3.1 illustrates the process of generating one random initial population. The detailed parameters used for GA in this work are summarized in Table 3.1.

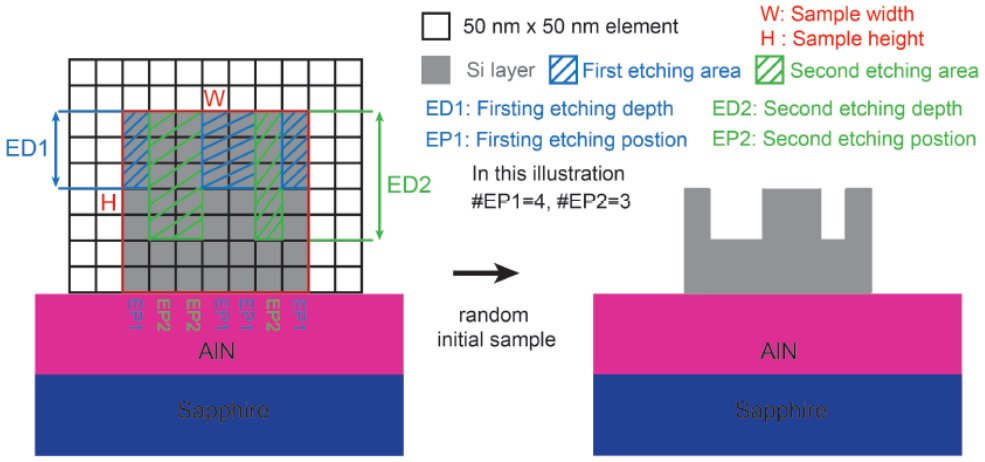

Figure 3.1: The schematic illustration of generating an initial random sample: A total simulation area of $1\mu m \times 1\mu m$ is discretized into a series of $50nm \times 50nm$ squares. The simulation area is limited within silicon layer. Each sample is decided by eight parameters: Waveguide width W, waveguide height H, First etching position #$EP1$, Second etching position #$EP2$, Number of EP1 #$EP1$, Number of EP2 #$EP2$, First etching depth #$ED1$, Second etching depth #$ED2$

A set of optical and mechanical modes is first calculated by COMSOL and these data are exported to calculate the SBS gain for each mode pair via Eq. 2.7 in Matlab. Q_m used in Eq. 2.7 are based on the material loss calculated with the viscosity and anchor loss simulated via PML in COMSOL. The gain coefficient is used as the fitness score.

TABLE 3.1: The parameters used for genetic algorithm

Optimization space	$1\mu m \times 1\mu m$
Element area	50nm $\times$ 50nm
FEM mesh	Triangular
FEM mesh resolution	15 nodes per element
Number of EP1 #$EP1$	Randomly select from (1:N), N=W/50 nm
Number of EP2 #$EP2$	N-#$EP1$
First etching position #$EP1$	Randomly select number of #$EP1$ positions from (1:N)
Second etching position #$EP2$	The rest positions after #$EP1$
First etching depth #$ED1$	Randomly select from (50 nm:50 nm: H)
Second etching depth #$ED2$	Randomly select from (50 nm:50 nm: H)
Initial size of population	100
Size of selection	50
Probability of mirror mutation (%)	20
Probability of reassign mutation (%)	20

The selection method is elitist, which means the samples with the highest gain (top 50) are selected for the next iteration. However, all results are saved no matter whether they are selected or not.

After the selection, the crossover phase will happen where new samples are generated until the population is as large as the initial population. As shown in fig. 3.2, to generate a new pair of samples (child α and β), two parents samples (Parent A and B) with their individual unique parameters are randomly chosen from the selected samples. During the crossover, the width and height of the parents will be swapped, generating two new combinations(W1 H2 and W2 H1). However, the remaining parameters will automatically follow the change of width and height. For example, the etching depth ED1 and ED2 will follow the swap of H1 and H2, the etching position and etching number will follow the swap of the width. As shown in fig. 3.2, Child α is generated with Parent A's width and Parent B's height. Therefore the etching position and etching numbers are taken from parent A and etching depth is taken from Parent B.

After the crossover stage, there is a certain mutation possibility for new generated samplers. The mutation phase in this work includes two mechanisms. one mechanism is called mirrored mutation, as shown in fig. 3.3 (a). The original sample is mirrored

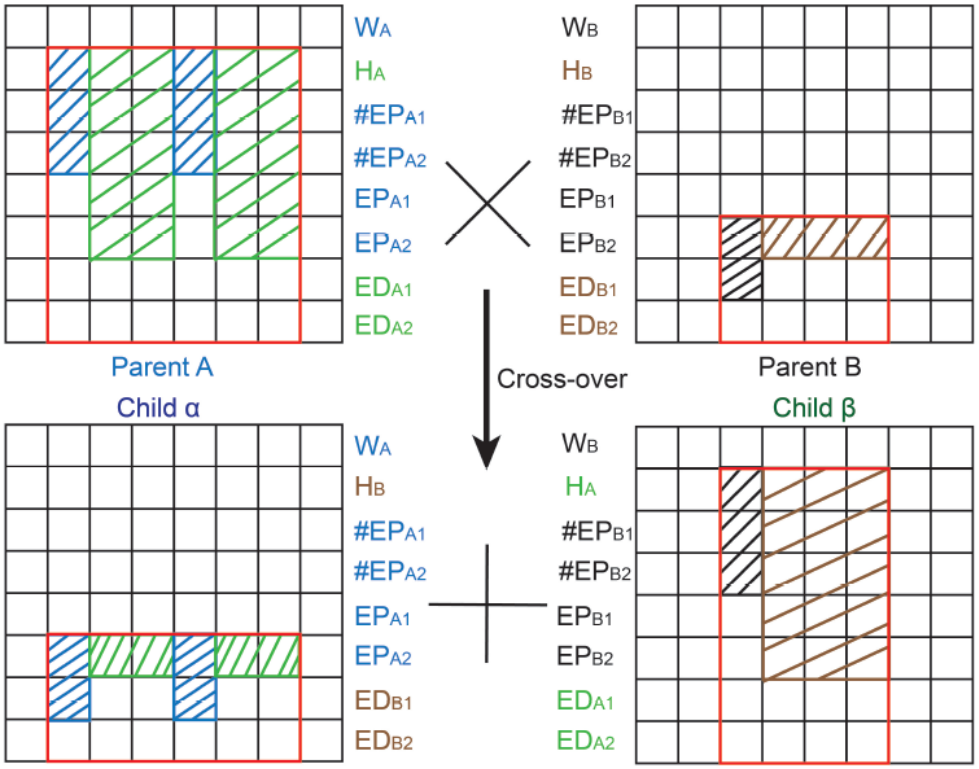

Figure 3.2: The schematic illustration of the crossover stage: the width and height of the parents will be swapped, generating two new children. However, the etching depth ED1 and ED2 will follow the swap of H1 and H2, the etching position EP1 EP2 and etching number #*EP*1 #*EP*2 will follow the swap of thw width.

across a randomly located axis. Then two new mutated samples are generated. One is mirrored from the right side of the axis and the other one from the left side of the axis. This mutation benefits symmetric waveguides.

The other mechanism is parameter re-assignation, as shown in fig. 3.3 (b), one of the eight parameters will have the probability of being randomly re-assigned. If the re-assigned parameter is one of the etching-related parameters, no other parameter will be changed. However, if the mutated parameter is the waveguide height or width, similar to the crossover stage, the parameters related with W or H will also mutate. For example, if the waveguide width is changed, then the etching numbers and positions will also be modified accordingly.

Afterwards, the new population is then re-evaluated to calculate the SBS gain, the best samples are selected for the next generation, and the loop continues. When there is no further change in the sample with the highest gain coefficient, the algorithm will stop.

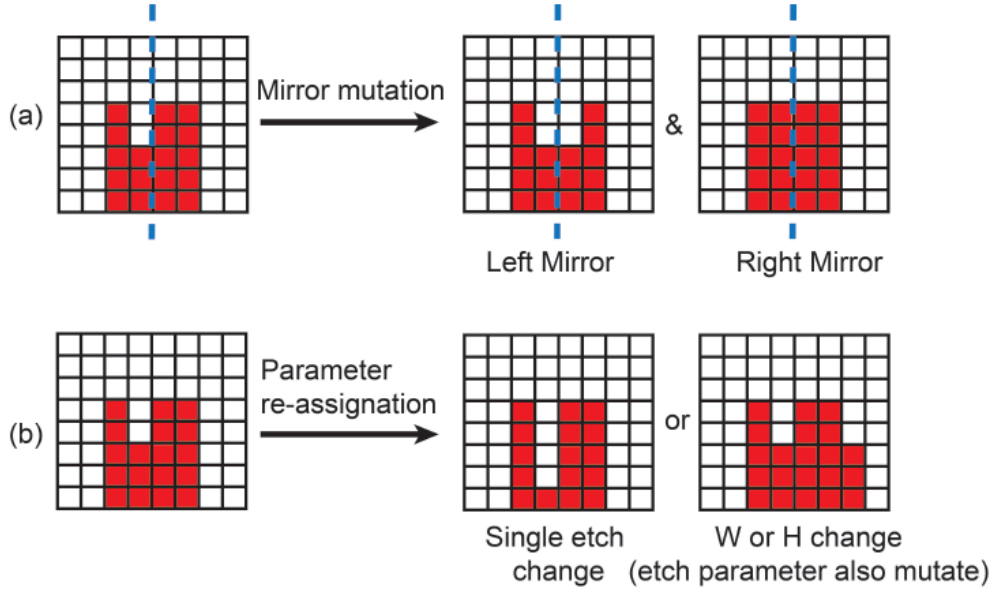

Figure 3.3: The illustration of two mutation mechanisms: (a) is the mirror mutation. Where the original sample is mirrored across a randomly located axis. Two new mutated samples are generated. (b) is the parameter re-assignation, where one parameter will be randomly reassigned. However, if the mutated parameter is the waveguide height or width, similar to the crossover stage, the related parameters will also mutate.

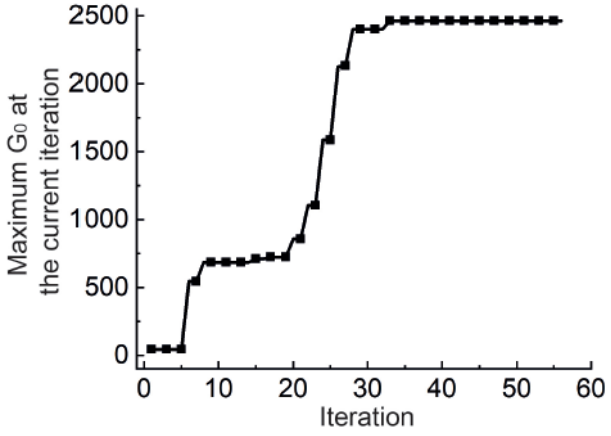

Figure 3.4: The convergence progress for the optimized structure. It converges into the SBS gain around 2500 after 32 iterations.

3.1.1 Convergence progress of the GA for Optimized structure

In this project, the GA was run five times parallel from Iridis high performance supercomputer. Each time initial population will consist of different seeds. All the seeds are generated randomly, with the constraints that the structure is limited within silicon layer and the maximum etching steps are two. Also, we focus on the fundamental optical modes of each generated structure.

For each run, the GA would arrive at slightly different results. This is due to the the

variation of the initial population and the uncontrolled crossover and mutation process during the optimization. However, each run would converge into a final SBS gain around 2000. The best result is what we reported in the fig. 3.5 (a). Fig. 3.4 shows the convergence progress for the optimized structure. It converges into the optimized structure after 32 iterations, which takes $\sim$ 48 hours.

3.2 Results and Discussions

3.2.1 Optimized waveguide structure for realizing large gain coefficient

Fig. 3.5 (a) shows the structure of the final optimized silicon waveguide. It is a thin and tall silicon waveguide with a shallow trench etched in the middle. The total thickness T of the waveguide is 620 nm, and the width W is 300 nm. The width a and height b of the trench is 100 nm and 105 nm, respectively. In this model, the thickness of AlN and sapphire are 600 nm and 700 nm, respectively. These values are the typical values from the commercial AlN wafer [24]. PML is designed to be 600 nm, which is thick enough to absorb the evanescent acoustic wave [129].

TABLE 3.2: The comparison between other works and this work.

Ref.	Structure	Material	SBS gain $W^{-1}m^{-1}$	Year
[37]	unsuspended	Si-Si_3N_4-SiO_2	300	2021
[48]	suspended	AlN-SiO_2	1311	2022
[19]	unsuspended	Si_3N_4-SiO_2	4x10-13	2020
[21]	unsuspended	$Ge_{25}Sb_{10}S_{65}$-SiO_2	56	2021
[20]	unsuspended	AlGaAs-SiO_2	1.2	2020
this work	unsuspended	Si-AlN-Sapphire	2462	2023

The fundamental TE-like and TM-like modes are shown in fig. 3.5 (b) and (c). It can be seen that TM-like mode is better confined within the silicon waveguide, while TE-like mode has stronger intensity on the boundary, which can be beneficial for increasing the SBS gain. Fig. 3.5 (d) shows the horizontal component of the selected acoustic mode. There is little energy leaking into the substrate, indicating strong confinement of the acoustic wave. In addition, the acoustic wave distribution matches with the TE-like mode optical mode distribution. Thus, it is expected that there is a strong coupling between the TE-like mode and the selected acoustic mode.

The best result we obtained is that for TE-like mode, the total Brillouin gain coefficient is $2462W^{-1}m^{-1}$ with the quality factor Q_m of 323. This quality factor has reached the

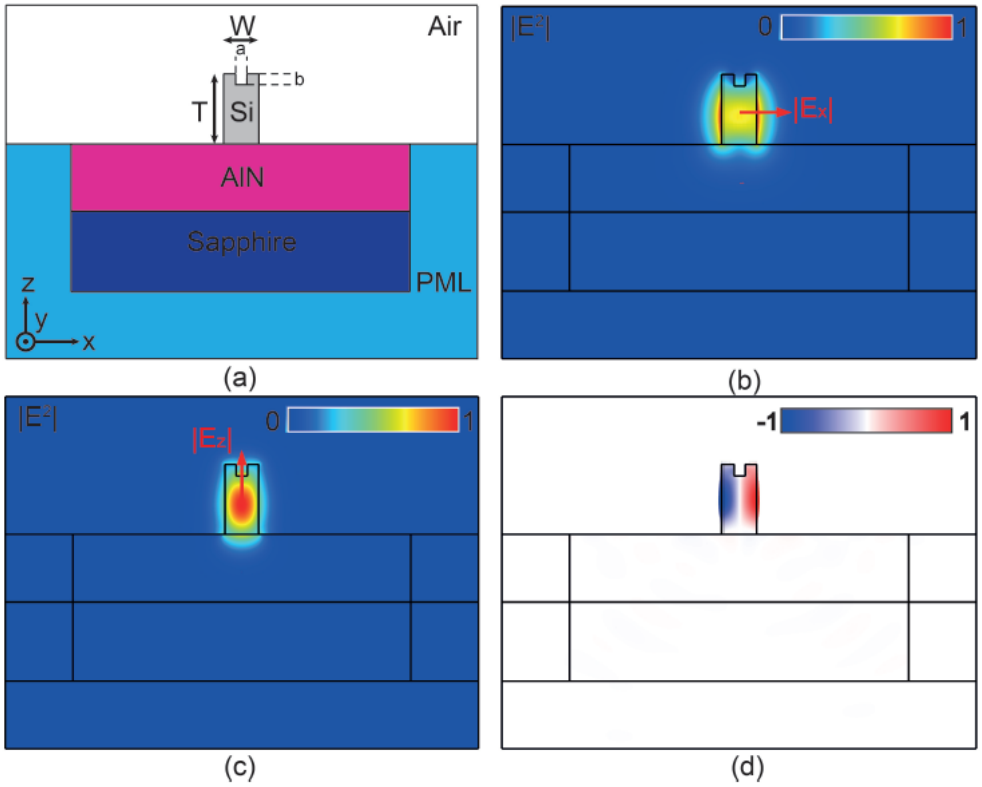

Figure 3.5: The schematic illustration of Si-AlN-Sapphire platform: (a) The cross-section of the optimized waveguide structure, the total thickness of silicon waveguide T is 620 nm, width W is 300 nm. The trench is located at the centre of the silicon waveguide. The dimensions of the trench is that width a=100 nm, and etch depth b=105 nm.(b) and (c) show the computed normalized E_x and E_z components of the optical TE-like and TM-like modes. (d) is the horizontal component of the selected acoustic mode.

measured quality factor limited by the material loss [19]. For TM-like mode, the highest gain is only around $200W^{-1}m^{-1}$ due to the mismatch of field distributions. The comparison between other works and this work is shown in Table 3.2. Our result is 8 times larger than the recently reported result in unsuspended silicon waveguide [37].

3.2.2 Influence of trench depth and width

Although the structure is found by the algorithm, the authors investigated the influences of trench depth and width to see how the additional trench improves the gain coefficient.

First, we study the influence of the trench depth. From Eq. 2.7, it can be seen that the final gain coefficient is decided by mechanical quality factor Q_m and normalized gain coefficient g_0. As shown in fig. 3.6 (a) and (b), with the change of etch depth, the normalized gain coefficient g_0 does not change dramatically for TE-like mode. While

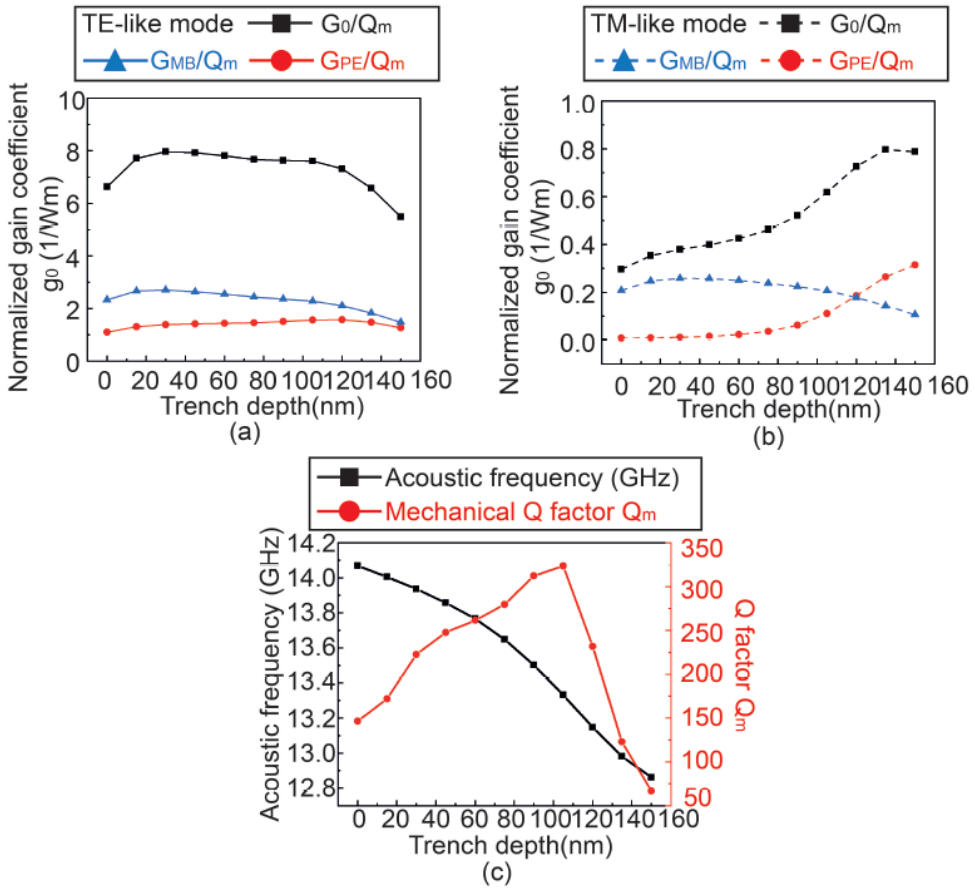

Figure 3.6: The results of intramodal FSBS for TE-like and TM-like modes: (a) shows the variation of the normalized gain coefficient g_0 for TE-like mode against the trench depth. There is no obvious boost for g_0. (b) shows the g_0 for TM-like mode. Although it has the tendency to grow with deeper trench depth, overall g_0 remains under $1W^{-1}m^{-1}$ due to the field distributions mismatch. (c) The acoustic frequency and Q_m as a function of trench depth. It can be seen that the main improvement that the trench brings in is to improve Q_m. A peak value of 323 is reached at the etch depth of 105 nm. This phenomenon can be explained by the node point theory [130]

for TM-like mode, although g_0 has the tendency to grow, it remains under $1W^{-1}m^{-1}$ due to the field distributions mismatch. Besides, the moving boundary term is the main contribution for TE-like mode as a result of higher optical intensity on the boundary. While for the TM-like mode, photoelastic effect becomes more dominant due to better confinement of the optical mode.

What makes a difference here is the Q_m. As shown in fig. 3.6 (c), compared to a typical slot waveguide ($b = 0$), the additional etch depth improves the confinement of the acoustic mode. The mechanical Q factor of the selected acoustic mode reaches a peak value of 323 at the etch depth of 105 nm. This phenomenon can be explained by the node point theory [130].

Fig. 3.7 (a-c) show the mode distributions of selected modes at different etch depth. The acoustic wave distribution is slightly modified with the change of etch depth. As

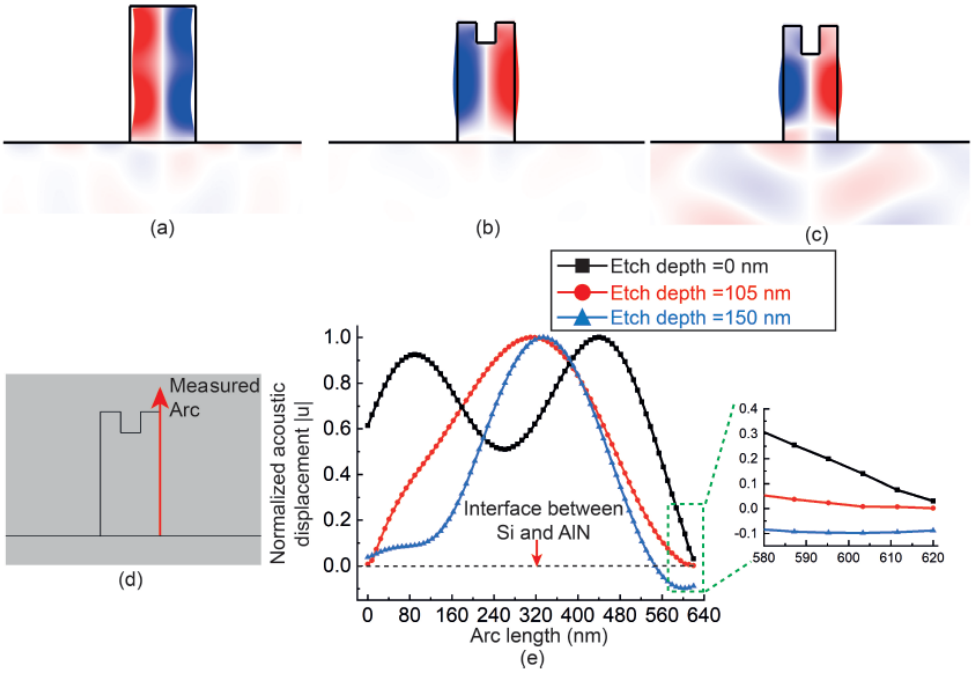

Figure 3.7: The influence of etching depth on acoustic wave: (a)-(c) shows the acoustic displacement at etch depth b of 0 nm, 105 nm and 150 nm, respectively. The energy leaking into the substrate at 105 nm is minimum, corresponding to the peak of Q_m. (d) illustrates the set-up for analysing the node point at the interface between Si and AlN. A measured arc is placed on the side wall of the waveguide. The displacement is collected along the measured arc. (e) shows the normalized acoustic displacement along the measured arc at different b. From the zoom-in inset figure, it can be seen that when b changes from 0 to 105, the displacement at the interface gradually decreases to zero, corresponding to the increase of the Q_m. After 105 nm, the displacement at the interface quickly goes to the other direction, leading to the leakage of the acoustic wave.

shown in fig. 3.7 (d), a measured arc is placed on the side wall of the waveguide, the acoustic wave displacement on the arc is extracted. The collected data is shown in fig. 3.7 (e). It can be seen that when the etch depth changes from 0 to 105 nm, the displacement at the interface between Si and AlN is gradually decreasing to zero, corresponding to the increase of the Q_m. After 105 nm, the displacement at the interface quickly goes to the other direction, leading to the leakage of the acoustic wave.

This is because at 105 nm, the acoustic mode distribution resembles the in-plane, out-of-phase fundamental mechanical mode of a tuning fork structure [130]. This form would enable the total force and moment at the outer end of the clamps to be zero, resulting in a lower anchor loss [130].

To provide a better understanding of what happens in the substrate, the authors also plot an absolute mechanical field on a logarithmic scale ($log|u|$), which is shown in fig. 3.8. It can be seen that at the optimized etch depth, the acoustic field leaked into the substrate is almost negligible, indicating the strong confinement of the acoustic

mode. Meanwhile, the leakage at 150 nm etch depth is stronger than that of 0 nm etch depth. This matches with the results from fig. 3.6 (c) that the Q_m at 150 nm is smaller than that at 0 nm.

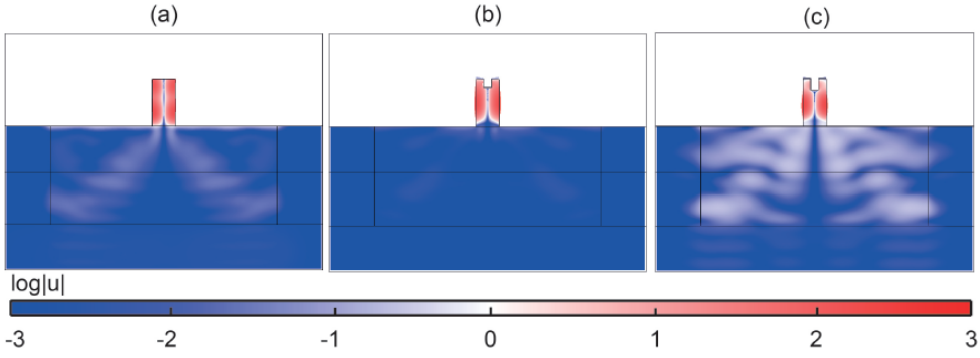

Figure 3.8: The absolute mechanical mode distribution on on a logarithmic scale ($log|u|$) at different etch depth: (a) to (c) corresponds to etch depth of 0 nm, 105 nm, 150 nm, respectively. At optimized etch depth, the acoustic field leaked into the substrate is almost negligible, indicating the strong confinement of the acoustic mode. Meanwhile, the leakage at 150 nm etch depth is stronger than that of 0 nm etch depth.

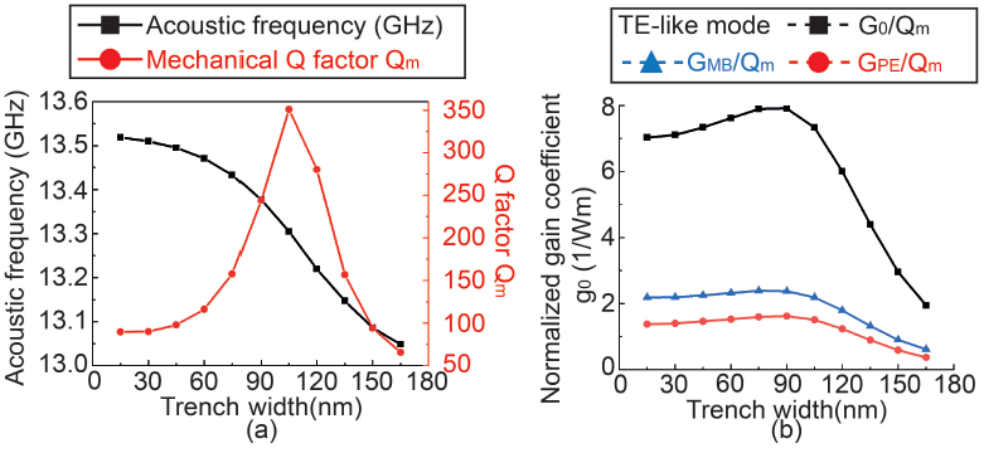

Figure 3.9: The influence of etching width on the Brillouin gain coefficient: (a) is the acoustic frequency and Q_m as a function of trench width. With fixed trench depth, there is a matched trench width to achieve the maximum of Q_m . (b) shows the variation of normalized gain coefficient g_0 with the change of trench width. g_0 is more sensitive to the change of trench width than depth. It will first slightly increase and after around 100 nm it will quickly drop due to a weaker confinement of the optical mode.

To conclude, at the optimized etch depth, the acoustic displacement at the interface of Si and AlN can be zero (a node point), leading to a reduced anchor loss and enhanced Q_m, thus enhanced total Brillouin gain coefficient.

The influence of the trench width on the final gain coefficient is also studied. The results are summarized in fig. 3.9. Similar to the etch depth, there is a optimized Q_m with the change of trench width. However, the normalized gain coefficient g_0 is more sensitive to the change of trench width. g_0 will first slightly increase and after around 100 nm it will quickly decline. This is because with the trench getting wider, the

confinement of the optical mode is also getting weaker, leading to a decrease in both the photoelastic effect and moving boundary.

3.3 Fabrication feasibility and tolerance analysis

To fabricate the structure, mature silicon photonic etching recipes can be applied and it only requires 2 etching steps. Alignments between these two etching steps is important. Similar etching procedure has been demonstrated in a micro ring resonator with shallow-etched periodic grating on the top of the waveguide [131]. Fig. 3.10 shows the tolerance for the misalignment of the trench, it can be seen that if the trench is off the centre by roughly 15 nm, the total gain coefficient will drop by half.

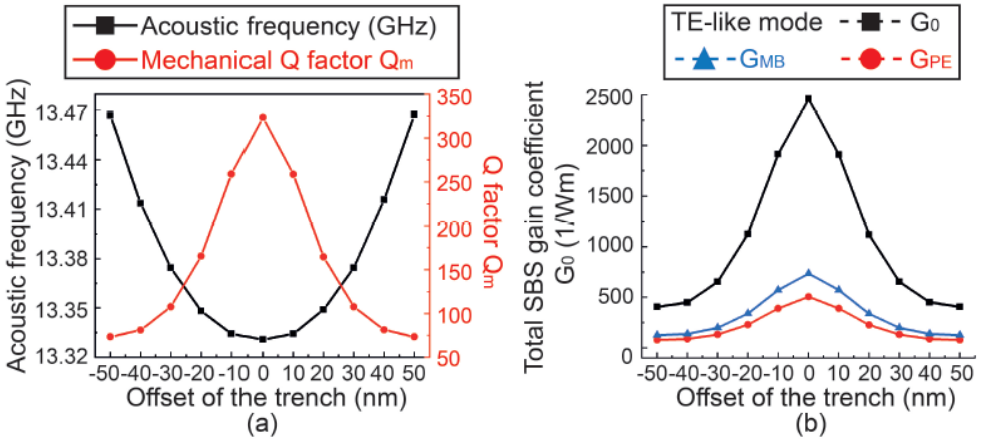

Figure 3.10: The tolerance analysis of the offset of the trench: (a) shows the acoustic frequency and Q_m versus the offset of the trench. (b) shows the changes of the total Brillouin gain coefficient and two contributions when the trench shifts away from the centre. it can be seen that if the trench is off the centre by roughly 15 nm, the total gain coefficient will drop by half.

3.4 Conclusion

We propose a novel Si-AlN-Sapphire platform for realizing a strong Brillouin scattering interaction without suspending the silicon core waveguide. This platform can not only improve the mechanical and thermal stability, but can also simplify the fabrication difficulty without sacrificing the crystal quality of the platform. To compensate for the reduction in the total gain coefficient in unsuspended structure due to the decreased moving boundary contribution, genetic algorithm is applied to optimize the waveguide structure and total gain coefficient. During the optimization, the maximum etching step is limited to two so that the final structure can be fabricable. A final structure with a shallow trench on the top of the silicon waveguide is found. This design can realize a total gain value of $2462 W^{-1} m^{-1}$, which is 8 times

larger than the recently reported result in unsuspended silicon waveguide. Further analysis found that the additional trench can create a node point at the interface between Si and AlN interface. This phenomenon will greatly suppress the anchor loss and can improve the Q_m to a level that limited by the fundamental material loss. We envisage that this system would be useful for the application in growing massive integrated photonic circuit and on-chip signal processing.

Chapter 4

On-chip OFDR system: Optical components and system design

4.1 OFDR theoretical model

OFDR technology was first proposed by Eickhoff in 1981 [132]. A typical structure of OFDR system is shown in fig. 4.1. The continuous light emitted by the tunable laser source (TLS) is separated into two ways after passing through the optical coupler 1 (OC1). One way enters the fiber under test (FUT) through the circulator and serves as the test arm. The other way serves as a reference arm and is connected to the optical coupler 2 (OC2) at the end. The backward Rayleigh scattering signal returned from the test arm interferes with the reference arm signal in the OC2, generates the beat signal which is then converted into electrical signal by photodetector (PD) and then analyzed in the signal processing unit.

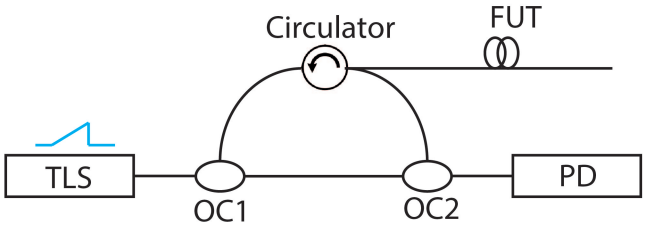

Figure 4.1: OFDR working principle

4.1.1 Linear frequency sweep

The OFDR system uses a periodic linear sweep light source. In order to simplify the derivation, the light source is assumed to be completely linear sweep. Therefore, the instantaneous optical frequency with a sweep period can be expressed as:

$$v(t) = v_0 + \gamma t, 0 \leq t \leq T. \tag{4.1}$$

where v_0 is the start frequency and γ is the linear frequency sweeping speed. Then the light field intensity emitted by the light source can be expressed as:

$$E_r(t) = E_0 e^{j2\pi(v_0+\gamma t)t}. \tag{4.2}$$

If the time delay between the test light returned from the position z of the FUT and the reference light is τ_z, and the optical path difference between the origin of the FUT and the end of the reference arm is set to zero, then z and τ_z have such a relationship:

$$\tau_z = \frac{2n_g z}{c}. \tag{4.3}$$

where n_g is the group index of the FUT and c is the speed of light in vacuum.

Suppose the attenuation coefficient of the FUT is α, and the reflection coefficient at position z is R_z, then the equivalent reflection coefficient at the position z of the FUT is:

$$R_{z_{eff}} = R_z e^{-\frac{\alpha \tau_z c}{n_g}}. \tag{4.4}$$

At this time, the test optical signal can be expressed as:

$$E_t(t) = E_0 \sqrt{R_{z_{eff}}} e^{j2\pi[v_0+\gamma(t-\tau_z)](t-\tau_z)}. \tag{4.5}$$

Beat frequency interference occurs between the test signal from the FUT and the reference signal from the reference arm, this process is shown in fig. 4.2.

The frequency of the beat signal is equal to the difference between the frequency of the reference signal and the test signal, which is

$$f_b = \gamma \tau_z = \frac{2n_g \gamma z}{c}. \tag{4.6}$$

The beat signal is then detected by the photo detector, the voltage can be expressed as:

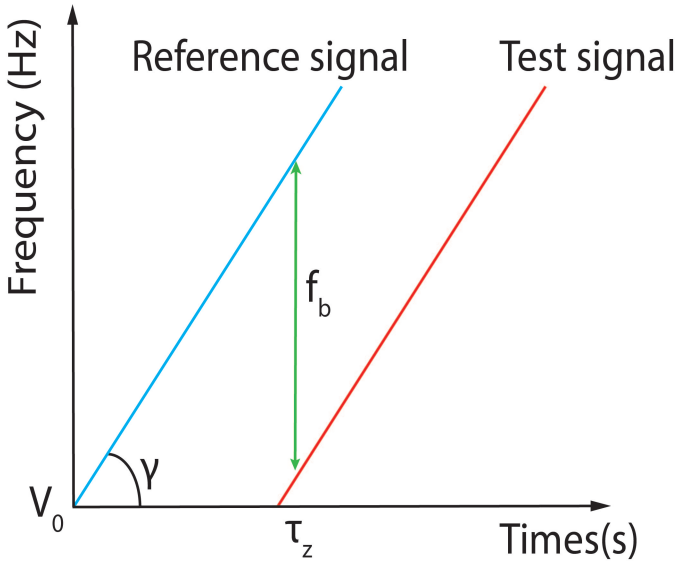

Figure 4.2: Beating interference during linear frequency sweep

$$U_{PD}(t) = \sigma|E_r(t) + E_s(t)|^2 \tag{4.7}$$

$$= \sigma E_0^2[1 + R_{z_{eff}} + 2\sqrt{R_{z_{eff}}}cos[2\pi(\gamma\tau_z t + v_0\tau_z - \frac{1}{2}\gamma\tau_z^2)]] \tag{4.8}$$

$$= \sigma E_0^2[1 + R_{z_{eff}} + 2\sqrt{R_{z_{eff}}}cos[2\pi(\gamma\tau_z t + \phi_{oz})]] \tag{4.9}$$

Where σ is the sensitivity of the PD, $\phi_{oz} = v_0\tau_z - \frac{1}{2}\gamma\tau_z^2$ is time independent variable.

Generally, only AC turn is considered, we remove the DC term and keep the AC term:

$$U_{PD}(t) = 2U_0\sqrt{R_{z_{eff}}}cos[2\pi(\gamma\tau_z t + \phi_{oz})]. \tag{4.10}$$

Where $U_0 = \sigma E_0^2$. It can be seen from Eq. 4.10 that the phase of the beat signal consists of two parts, one part is $\gamma\tau_z t$, which is a time linear term; the other part is ϕ_{oz}, which is a time-independent term. Therefore, for an ideal linear frequency sweep, the frequency of the beat signal is proportional to the time delay τ_z.

By substituting Eq. 4.1 into Eq. 4.10, the beat signal then can be regarded as a function of frequency v:

$$U_{PD}(t) = 2U_0\sqrt{R_{z_{eff}}}cos(2\pi v\tau_z t + \phi_z). \tag{4.11}$$

Where $\phi_z = -\pi\gamma\tau_z^2$ is a frequency independent term. From Eq. 4.11, it is found that Fourier transform can be used to transform the beat signal from the frequency domain

v to the spatial domain τ_z. Therefore, by using Fast Fourier Transform (FFT) algorithm, the frequency domain v is converted to the spatial domain τ_z, which is what we need for distributed sensing.

4.1.2 Nonlinear frequency sweep

In the previous discussion, it is assumed that the frequency is swept perfectly linearly with time. But this is impossible for any TLSs on the market. The frequency tuning speed $\gamma = \gamma(t)$ is not a constant due to tuning nonlinearity, which means $v = \gamma(t)\tau_z$ is not linear with τ_z anymore.

Generally, the reference signal from the TLS can be expressed as:

$$E_r(t) = E_0 e^{j\phi(t)}. \tag{4.12}$$

The corresponding instantaneous frequency is:

$$v(t) = \frac{1}{2\pi}\frac{d\phi(t)}{dt}. \tag{4.13}$$

Expend Eq. 4.12 into Fourier series:

$$E_r(t) = \int_{-\infty}^{+\infty} E_r(v) e^{-j2\pi vt} dv. \tag{4.14}$$

After the light travels back and forth through a FUT of length z, the test signal can be expressed as:

$$E_s(t) = \sqrt{R_{zeff}} \int_{-\infty}^{+\infty} E_r(v) e^{-j2\pi vt} e^{j\beta(v)2z} dv. \tag{4.15}$$

The propagation constant $\beta(v)$ can be expanded in terms of frequency v according to Taylor expansion, and we only take the first order approximation:

$$\beta(v) = \beta(v_0) + \beta'(v_0)(v - v_0). \tag{4.16}$$

The terms $\beta(v)$ and $\beta'(v_0)$ can be related with the phase velocity v_{mph} and group velocity v_{mgr}, respectively:

$$\begin{cases} \beta(v) \cdot v_{mph} = 2\pi v_0 \\ \beta'(v_0) \cdot v_{mgr} = 2\pi \end{cases} \tag{4.17}$$

Phase velocity v_{mph} and group velocity v_{mgr} also can be expressed by group delay τ_{mgr} and phase delay τ_{mph}:

$$\begin{cases} v_{mph} = \frac{2z}{\tau_{mph}} \\ v_{mgr} = \frac{2z}{\tau_{mgr}} \end{cases} \tag{4.18}$$

The reference signal and the test signals returned from different positions z interfere and the beat signals are generated in the optical coupler. After being detected by the photodetector, the beat signal can be expressed as:

$$U_{PD}(t) = \sigma |E_r(t) + \sum_{m=1}^{M} E_{ms}(t)|^2. \tag{4.19}$$

Combining Eq. 4.12- 4.18, the Eq. 4.19 is finally simplified as:

$$U_{PD}(t) = 2U_0 \sum_{m=1}^{M} \sqrt{R_{z_m eff}} cos[2\pi v \tau_{mgr} + \Phi_m]. \tag{4.20}$$

Where $\Phi_m = -2\pi v_0(\tau_{mph} - \tau_{mgr})$ is the frequency-independent term. Comparing Eq. 4.11 and Eq. 4.20, it is found that regardless of whether the TLS is an ideal linear frequency sweep, as long as the measured instantaneous frequency v is accurate, the Fourier transform can be used to transform the signal from frequency domain to the desired spatial domain, which corresponds to the positions of the FUT.

However, since the TLS is not a complete linear frequency sweep, the obtained frequency v is no longer at equal intervals. The signal required by the FFT algorithm must be a discrete signal distributed at equal intervals. If FFT is still performed at this time, it will lead to a decrease in the spatial resolution, so that positioning and sensing cannot be performed [133].

The impact of the nonlinear frequency sweep can be explained by the frequency sweeping speed γ. When the TLS cannot achieve a complete linear frequency sweep, the frequency sweeping speed γ will be no longer a constant, but a function of t:

$$\gamma = \gamma(t). \tag{4.21}$$

Then Eq. 4.6 will be modified as:

$$f_b = \gamma(t)\tau_z = \frac{2n_g\gamma(t)z}{c}. \tag{4.22}$$

From Eq. 4.22, it is found that due to the nonlinear frequency sweep, the frequency of the beat signal f_b obtained at the same position z is no longer a constant but a time-dependent variable. If OFDR still use the linear relation between f_b and z for positioning, the frequency of the beat signal will be broadened and the system's spatial resolution will be deteriorated.

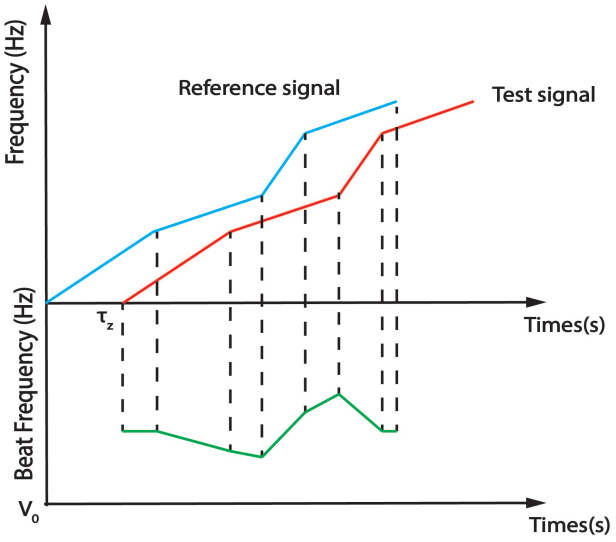

Figure 4.3: The beating frequency under nonlinear frequency sweep

As shown in fig. 4.3, the blue curve is the reference signal under nonlinear frequency sweep, its slope is changing with time. The red line is the test signal returned from a certain position z of the FUT. The green curve is the beat signal signal. Due to the nonlinear frequency sweep, the beating frequency is no longer constant, its bandwidth is broadened and this will lead to the reduction of the peak amplitude of the reflected signal, energy leakage, which significantly deteriorate the spatial resolution of the system.

4.1.3 Compensation of nonlinear frequency sweep

As previously mentioned, an equal frequency interval is required in order to operate FFT algorithm correctly and obtain decent spatial resolution. One approach is to employ an unbalanced Mach-Zehnder interferometer (MZI) as an external trigger to sample the beat signal at equal frequency interval, which is shown in fig. 4.4. The set-up contains two MZIs: one is the main interferometer (MI) which collects the signal from FUT and generate the beat signal; the other one is the auxiliary interferometer (AI), which is used as an external trigger.

Once the beat signal is generated by the MI, it will be resampled by the triggering signal from the AI. This process avoids the impact of the sweep nonlinearity of the TLS since both signals of MI and AI come from the same laser source.

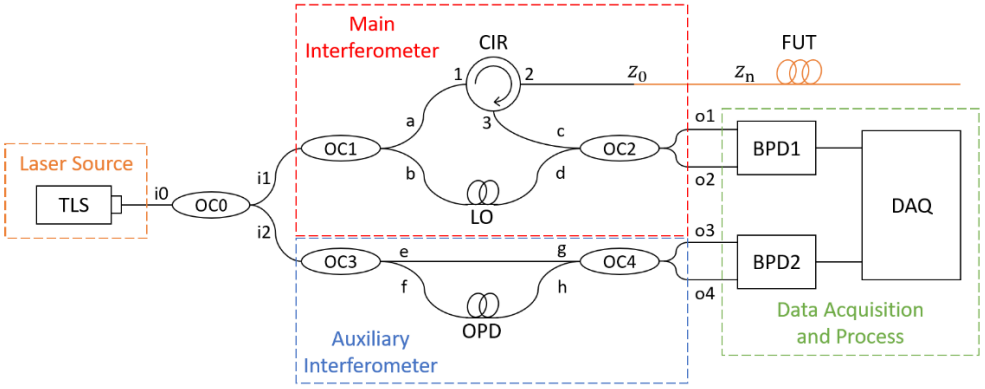

Figure 4.4: Schematic of the OFDR set up

4.1.4 Main parameters

4.1.4.1 Spatial resolution

Spatial resolution generally refers to the smallest distance between two adjacent points that the sensing system can distinguish. OFDR can reach very high spatial resolution, even on the order of μm. According to the theory of digital signal processing, the frequency resolution in the FFT has an inverse relationship with the total sampling time. The beat signal can be transformed from the frequency domain v to the spatial domain τ using FFT, thus:

$$\Delta\tau = \frac{1}{\Delta v}. \tag{4.23}$$

Where Δv is the frequency sweeping range of the light source, $\Delta\tau$ is the resolution of the time delay. The relationship between $\Delta\tau$ and the spatial resolution Δz can be obtained by differentiating both side of Eq. 4.3:

$$\Delta z = \frac{c\Delta\tau}{2n_g}. \tag{4.24}$$

Substitute Eq. 4.23 into Eq. 4.24:

$$\Delta z = \frac{c}{2n_g\Delta v}. \tag{4.25}$$

Also, since the frequency and the wavelength have the following relation:

$$v = \frac{c}{\lambda}. \tag{4.26}$$

Differentiate both side of Eq. 4.26:

$$\Delta v = \frac{c\Delta\lambda}{\lambda^2}. \tag{4.27}$$

Finally, substitute Eq. 4.27 into Eq. 4.25:

$$\Delta z = \frac{\lambda^2}{2n_g\Delta\lambda}. \tag{4.28}$$

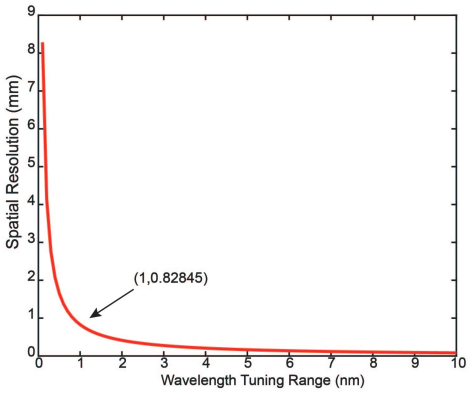

Figure 4.5: The relationship between the spatial resolution and the wavelength tuning range

Eq. 4.28 describes the relationship between the spatial resolution and the wavelength tuning range $\Delta\lambda$. As shown in fig. 4.5, when the centre wavelength λ is selected, a larger wavelength tuning range corresponds to a better spatial resolution. Assuming the group refractive index of the FUT $n_g = 1.45$, and the laser works in the communication band ($\lambda = 1550mn$), the spatial resolution can reach 0.83 mm when the wavelength tuning range is 1 nm.

4.1.4.2 Laser linewidth

The laser linewidth refers to the the full width at half-maximum (FWHM) of a single mode, which is an important parameter to measure the quality of the laser. OFDR uses a coherent optical heterodyne detection scheme, which requires high laser coherence. In order to ensure that the Rayleigh scattered light returned from the FUT can be coherent with the reference light, the coherence length of the laser must exceed the optical path difference between the two arms of the interferometer. When a laser with linewidth Δf is transmitted in to optical fiber, its coherence length is:

$$L_c = v_g \cdot \tau_c = \frac{c}{n_g} \cdot \frac{1}{\Delta f}. \tag{4.29}$$

Where $\tau_c = \frac{1}{\Delta f}$ is the coherent time of the laser.To ensure high visibility of the beat signal, the round-trip length of the light in the fiber should be smaller than the coherent length of the light source, that is:

$$Z_{max} \leq \frac{L_c}{2}. \tag{4.30}$$

Substitute Eq. 4.29 into Substitute Eq. 4.30:

$$Z_{max} \leq \frac{c}{2n_g \Delta f}. \tag{4.31}$$

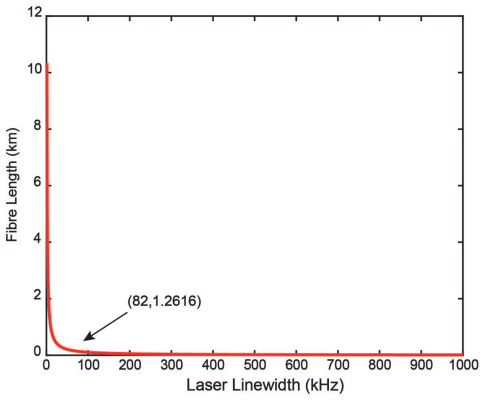

Figure 4.6: The relationship between sensing distance and the laser lindewidth

Eq. 4.31 describes the relationship between the maximum sensing distance Z_{max} and the laser linewidth Δf, which is shown in fig. 4.6. For 1.2 km-long fibre, the required laser linewidth $\Delta f \leq 82kHz$. In conclusion, to realize long-distance sensing, a light source with a narrow linewidth should be selected.

4.1.4.3 Sampling frequency

The electrical signal collected by the photodetector needs to undergo an alog-to-digital conversion before it can be processed by the subsequent digital signal processing unit. According to the Nyquist sampling theorem, in order to restore the original signal, the sampling frequency must be greater than twice the frequency of the analog signal, that is to say, the sampling frequency of the data acquisition card must be more than twice the frequency of the beat signal. After the light traverses the FUT of length z, the frequency of the beat signal is:

$$f_b = \gamma \tau_z = \gamma \frac{2n_g z}{c}. \tag{4.32}$$

The frequency sweeping rate γ can be expressed as:

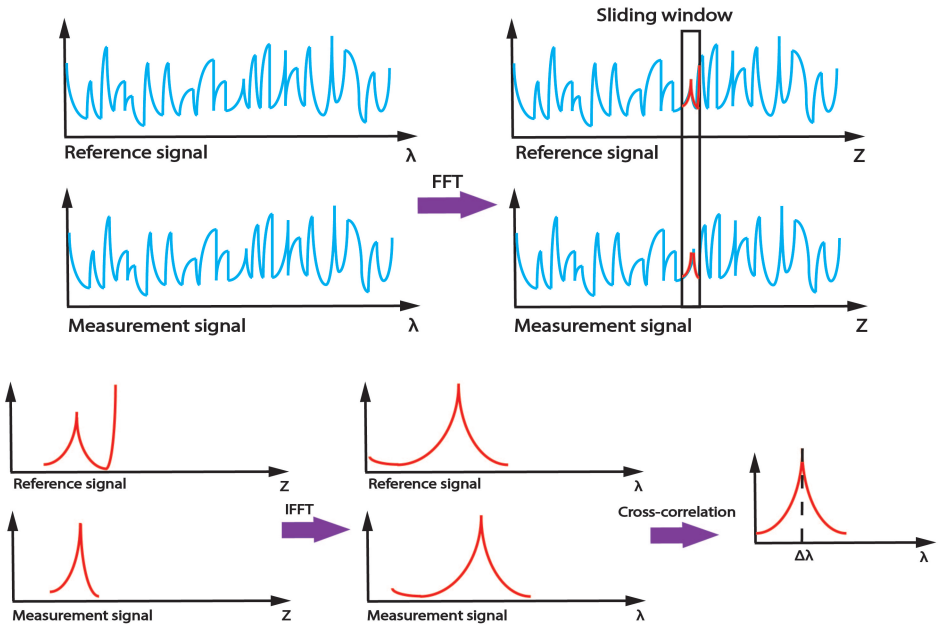

Figure 4.7: The calculation process of OFDR sensing

$$\gamma = \frac{\Delta v}{\Delta t} = \frac{c}{\lambda^2}\frac{\Delta \lambda}{\Delta t}. \tag{4.33}$$

And substitute Eq. 4.33 into Eq. 4.32:

$$f_b = 2n_g z \frac{\Delta \lambda / \Delta t}{\lambda^2}. \tag{4.34}$$

From Eq. 4.34, when the centre wavelength is selected, a faster wavelength sweeping rate or a longer fibre length will bring a larger beat frequency, which requires a larger sampling frequency. Assume that the centre wavelength is 1550 nm and the wavelength sweeping rate 1nm/s, the beat frequency corresponding to a 1 km-long FUT is about 1.25 MHz, the minimum sampling frequency of the data acquisition card is then 2.5MS/s.

4.1.5 Rayleigh scattering spectroscopy theory

OFDR realizes the positioning of the measurands based on the beat frequency, while Rayleigh scattering spectroscopy theory helps the quantitative measurement of the external stress or temperature. Combining OFDR and Rayleigh scattering spectroscopy theory can realize distributed stress and temperature sensing. This process is shown in fig. 4.7[134]:

Step 1: Taking two measurements under different temperature or strain conditions, the collected signals are considered as the reference signal and the measurement signal, respectively.

Step 2: Transforming the two signals from frequency domain to the spatial domain by FFT.

Step 3: A sliding window with a length Δx is used to intercept the reference signal and the measurement signal at the same position.

Step 4: Inverse-FFT is performed on the intercepted measurement and reference signals, where the signals are converted back to the wavelength domain.

Step 5: Cross-correlation is performed between the Rayleigh scattering spectra of the intercepted measurement and reference signals. The original point of the cross-correlation peak will shift when the external stress or temperature is different.

Repeat step 3-5, the distributed temperature or stress information along the fibre is obtained.

4.2 On-chip OFDR system

Based on the theoretical model of OFDR, we design an on-chip OFDR system, which is shown in fig. 4.8. The optical signal from the TLS is coupled into the system by grating coupler (GC). Then it is divided into two paths by a 10:90 power splitter, in which, 10 % of the signal is sent to the auxiliary interferometer (AI), which provides an external trigger to sample the beat signal from the main interferometer (MI). 90% of the signal is sent to the MI for testing the FUT.

In this design, FUT is represented by a strip waveguide. In order to test the performance of the system, two grooves with the same size are etched at different positions of the waveguide, the detectable minimum distance between the two grooves corresponds to the maximum spatial resolution of the system. The reflected Rayleigh scattering signal from the grooves enters the MI and interferes with the reference signal to generate the beat signal. The beat signal is then coupled out and detected by an external photodetector.

In conventional OFDR system, an optical circulator is used to lead the reflected light back to the MI. However, it becomes challenging in on-chip OFDR system because of the reciprocity of the light. Using active component such as magneto-optical device is an alternative, but it also increase the complexity of the system. Therefore, we decide to use a 50:50 power splitter to replace the circulator at the expense of 3 dB loss of the reflected signal. In order to avoid the damage to the light source from the reflected signal, an external isolator is arranged behind the input GC.

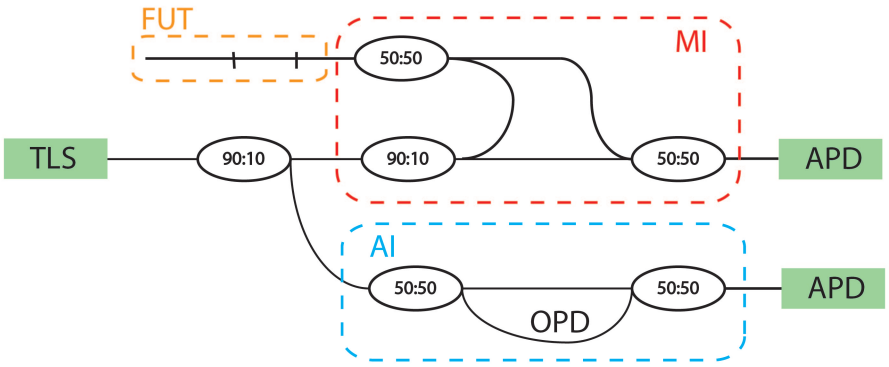

Figure 4.8: Schematic view of the on-chip OFDR system

4.2.1 Power splitter design

The function of power splitter is the same as the optical coupler in the fibre system. Here, two power ratios are needed: one is used to separatae the MI and the AI, where 90% of the signal comes to the MI and the rest 10% comes to the AI. The other one is used to separate the test arm and the reference arm, both occupy 50% of the input signal. There are several photonic devices that can be utilized to fulfil the function of power splitting, such as Y-junction [135], multimode interferometer (MMI) [75], inverse-design-based power splitter [87] and directional coupler [76]. Here, MMI with the power ratio of 10:90 and 50:50 are designed, respectively. After that, power splitters that achieve arbitrary power ratios are designed using DBS algorithm.

4.2.1.1 MMI

MMI is an optical multimode interference device based on Self-Imaging theory [75]. As shown in fig. 4.9(a). When a single-mode input enters the multi-mode region of a waveguide, high-order modes will be excited and they will interfere at a certain distance to form the self-imaging of the input mode. Self-imaging will occur when all the modes in the multimode area arrive in phase at the same point [75]. Therefore, different splitting ratios can be achieved by positioning the output waveguides at different self-imaging points. Typically, for 50:50 MMI, the length of the multi-mode region is $\frac{3}{8}L_\pi$, where $L_\pi = \frac{4n_e W_e^2}{3\lambda}$ is the length over which a π phase shift is realized between the first two guided modes, W_e is the effective width of the multi-mode region.

Fig. 4.9 (b)-(c) display the simulated MMIs for the 50:50 and 10:90 power ratios, respectively. The devices are based on an SOI platform with a 220-nm-thick top silicon layer. For both MMIs, 20μm-long taper waveguides are used as the input and output waveguides. The start and end width of the taper waveguide are 450nm and 2.6μm, respectively.

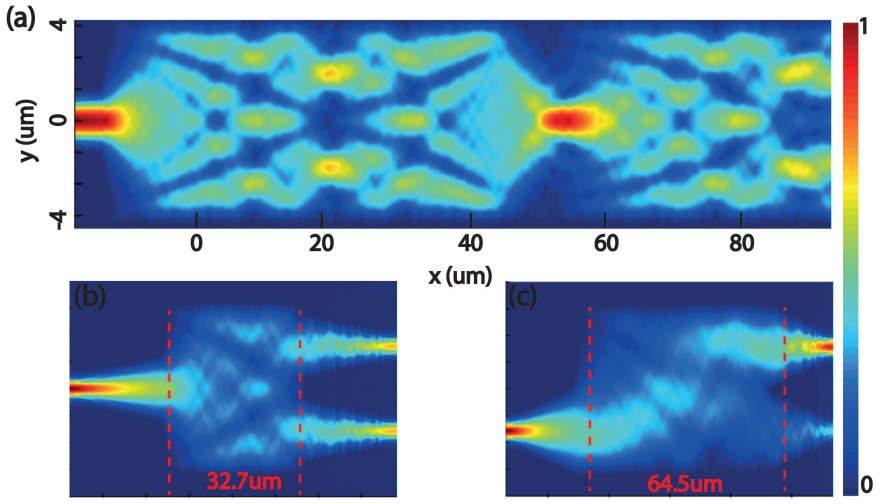

Figure 4.9: (a) The simulated Self-Imaging effect in MMI. For a 6-um-width MMI, the self-imaging point of the input fundamental TE mode is at 55um. (b,c) The simulated MMI with 50:50 and 10:90 power splitting ratios, respectively.

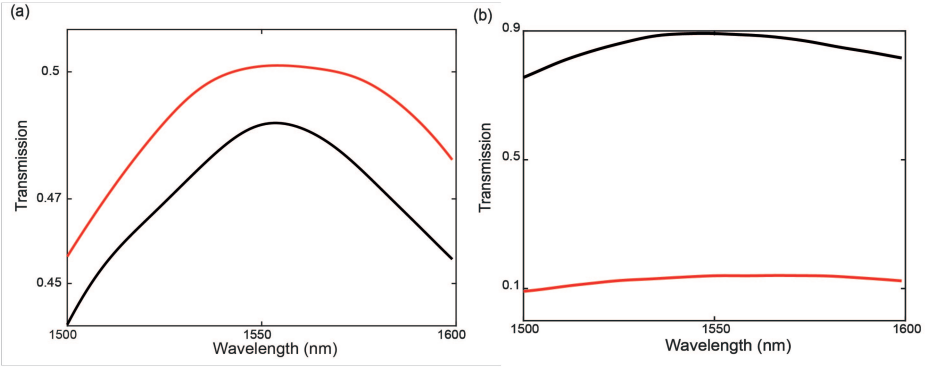

Figure 4.10: The simulated transmissions over the wavelength of 1500 nm-1600nm. The black and red lines represent the transmissions at the upper and bottom ports, respectively. (a) 50:50. (b) 10:90

For 50:50 MMI as shown in fig. 4.9 (b), the width and length are $6\mu m$ and $32.7\mu m$, respectively. For 10:90 MMI as shown in fig. 4.9 (c), an asymmetric structure is designed to achieve asymmetric distribution of the self-imagining points. 10:90 power ratio is achieve when the length of the multi-mode region is $64.5\mu m$. Fig. 4.10 shows the transmission of the device over the wavelength range from 1500nm to 1600nm. The black and red lines represent the transmissions at the upper and bottom ports, respectively. For both splitting schemes, the errors are within 10%.

4.2.1.2 DBS-optimized power splitters with arbitrary power splitting ratios

One of the disadvantages of MMI is its large footprint, which is over tens of micro meters. It is necessary to design sub-wavelength ultra-compact photonic devices to realize high-dense PICs. Photonic inverse designs provide a way for designing

ultra-compact devices by searching the full-parameter space. Here, we aims to design power splitters with arbitrary power splitting ratios using DBS algorithm, which will replace the MMIs to reduce the size of the system.

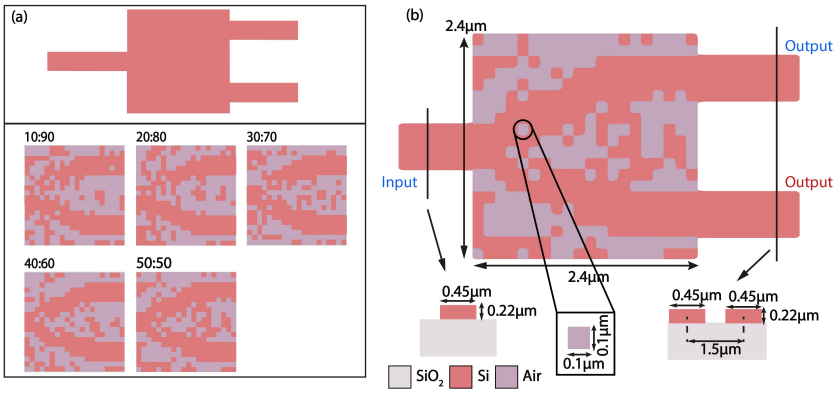

Figure 4.11: (a) The initial pattern is shown on the top. The optimized patterns for different splitting ratios are shown below. (b) The optimized structure for 50:50 power splitter.

Fig. 4.11 (a) shows the initial pattern and the optimized patterns for different splitting ratios. Here, the power ratios of 10:90, 20:80, 30:70, 40:60 and 50:50 are presented. The detailed structure information is shown in fig. 4.11 (b). The whole device is also based on an SOI platform and the height of the silicon layer is 220 nm. The widths of the input and output waveguides are 450 nm, and the gap between the two output waveguides are designed to be 1.5 μm to avoid crosstalk. The footprint of the design region is $2.4 \times 2.4 \mu m^2$, which is discretized into 100 nm $\times$ 100 nm pixels. Each pixel has two states: "0" represents silicon, and "1" represents air. The etching depth of the pixel is 220 nm.

The 3D finite-difference time-domain (FDTD) method is utilized to calculate the FOM using Lumerical FDTD Solutions. The simulations finish when the FOM growth falls below 1%. The optimization time for each power splitting ratio is within 10 hours, where the FOMs converge before the 10th iteration. The optimizations are operated on the IRIDIS High Performance Computer Cluster.

Fig. 4.12 (a) shows the electric field distributions for the optimized structures. a high intensity can be observed at the core of the waveguide, which means most the output modes are the fundamental TE mode, which is as our expectation. Fig. 4.12 (b) is the corresponding transmission spectrum for each splitting ratio. The dashed and solid line represent the outputs from the upper and bottom ports, respectively. The results show good performance over a bandwidth of 100 nm, the maximum error is within 5% for each splitting ratio. Compared with MMIs, the splitting ratios of the DBS-optimized power splitters do not rely on the designing length of the device, the footprints are massively reduced.

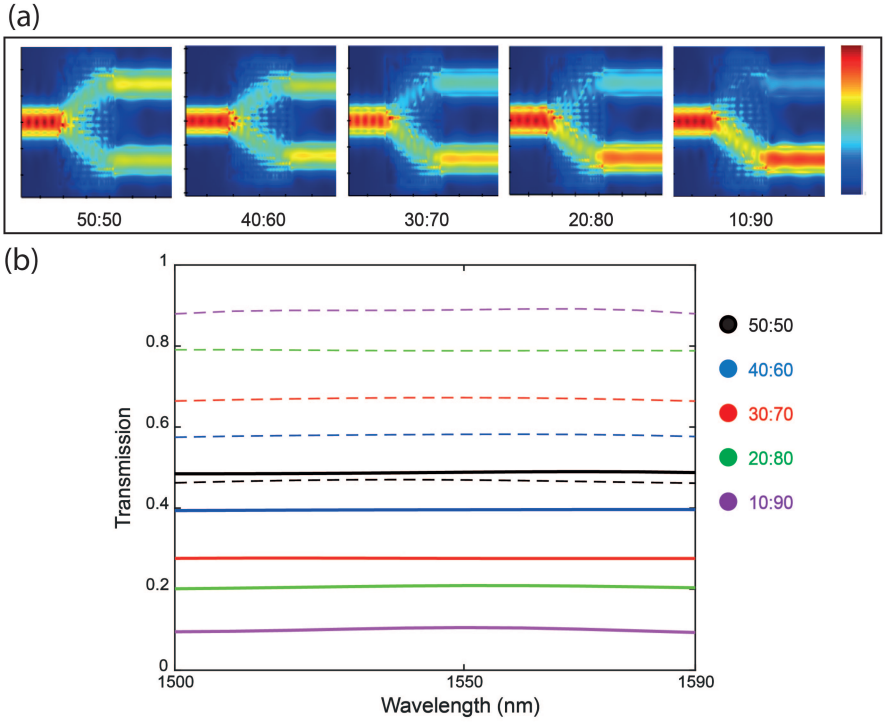

Figure 4.12: (a) The simulated electric field distribution for each splitting ratio.(b) The simulated transmission spectrums over the wavelength of 1500nm-1600nm. The dashed line and the solid line represent the outputs from the upper and bottom ports, respectively. Black: 50/50, blue: 40/60, red: 30/70, green: 2080 and purple: 10/90.

4.2.2 Experimental verification

4.2.2.1 Fabrication process

The devices are based on a $3cm \times 4cm$ SOI platform with $2\mu m$-thick BOX layer and $220nm$-thick silicon layer. The chip is first soaked in acetone and IPA solvents for 10 minutes, respectively, to remove the S1813 photoresist, which protects the chip during dicing. After that, blow dry is conducted before the photoresist coating. Then ZEP-520A electron beam photoresist is coated onto the top of the silicon layer, which is shown in fig. 4.13(b). Following the pre-bake at 180° for 3 mins, Espacer is coated onto the ZEP-520A resist to increase its conductivity during the E-beam lithography process.

E-beam lithography is then utilized to write the designed patterns onto the chip. After that, the exposed photoresist is developed using ZED-N50 developer (fig. 4.13(c)): The chip is first rinsed with DI water to remove the Espacer. Then the chip is soaked in the ZEP-N50 solutions for developing. During the developing, hard shaking is needed to ensure the full interaction between the solvent and the photoresist, the developing lasts 100 seconds. After that, the chip is soak in IPA for 45 seconds to remove the developer and ready for the next step.

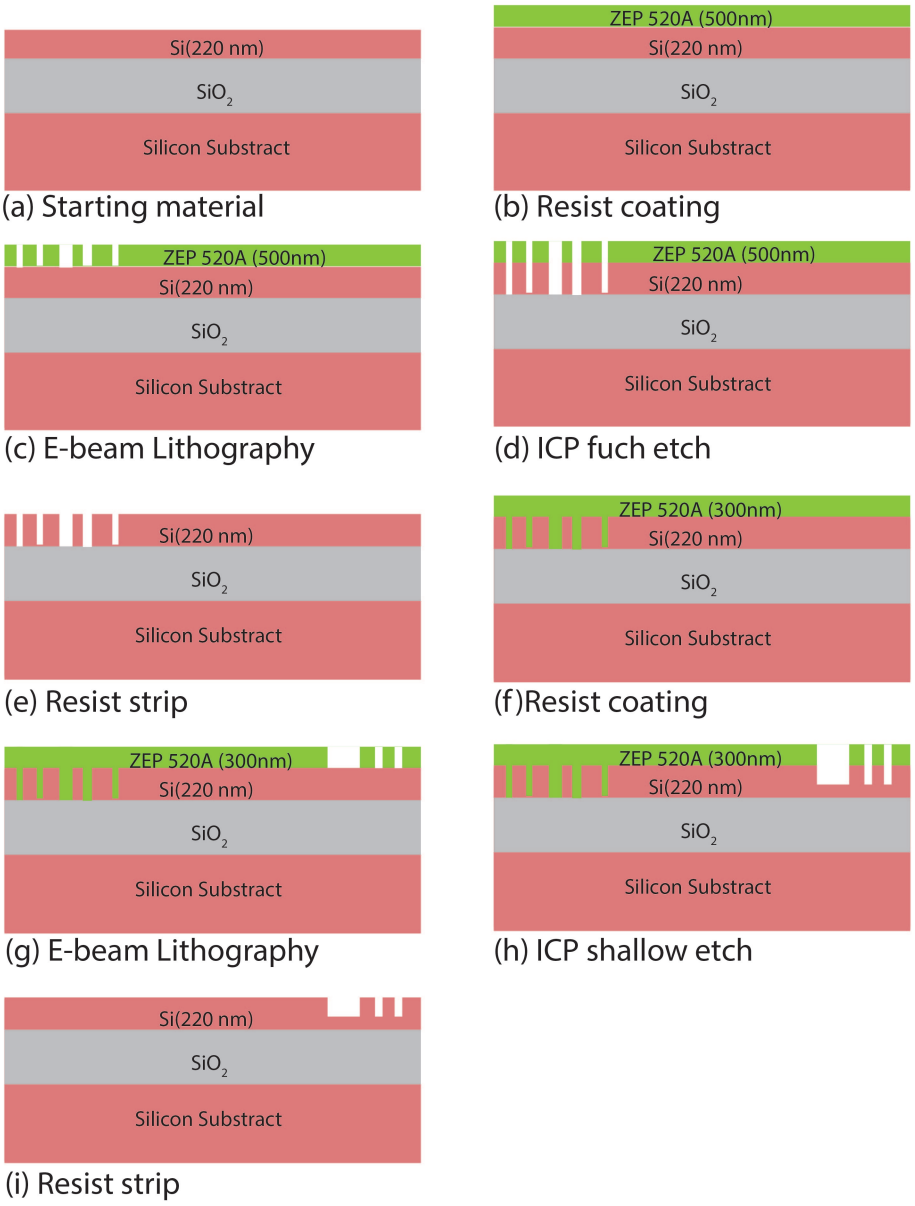

Figure 4.13: The fabrication process. Two etching steps are needed in this experiment. (a-e) The fabrication of the waveguides. (f-i) The fabrication of the grating couplers.

There are two etching steps needed in this design. As shown in fig. 4.13(d), a full etching of 220nm is performed first using inductively coupled plasma (ICP) etching to etch the waveguides, since the full etching helps the alignment marks be distinguished during the E-beam lithography process, which increases the accuracy of calibration for the second etching step. Then, a plasma asher is utilized to strip the remaining resist, the result is shown in fig. 4.13(e). The etching of the grating couplers follow the same process as the first etching (fig. 4.13(f-i)), shallow etch is used, where the etching depth is 70nm.

4.2.2.2 Measurement setup

The measurement setup for characterising the photonic devices is shown in fig. 4.14. Keysight 81940A is used as the tunable laser source. The light is first passing through the polarization controller, which is adjusted to excite the transverse electric (TE) mode into the devices. After that, the light is coupled in and out from the devices by grating couplers. During the test, the alignments between the cleaved fibre and the grating couplers on the devices are achieved by finely tuning the 3-axis stages and the angles of the fibre arms, the best alignment is achieved when the highest transmitted power is obtained. The light that is coupled out from the device is then detected by Keysight 81634B monitor.

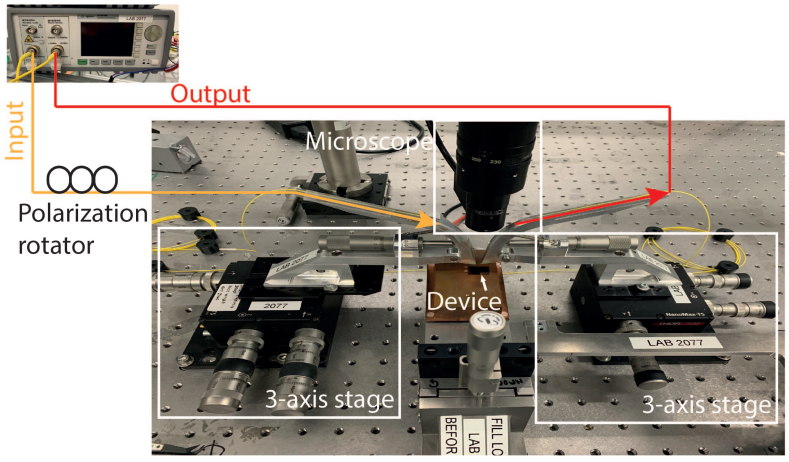

Figure 4.14: The measurement setup.

4.2.3 Experiment results

4.2.3.1 MMI

The fabricated 50:50 and 10:90 MMIs and their transmission responses are shown in fig. 4.15 (a) and (b), respectively. For 10:90 MMI, an asymmetric structure is designed to generate asymmetric electrical field distributions, which means only one of the left-side ports will be used as the input for power splitting. The maximum transmissions for the upper and lower ports are -1 dB and -9.5 dB at 1550 nm, which correspond to 0.794 and 0.112 of the total power, respectively. Therefore, the actual power splitting ratio is $\sim 11:80$, the loss is $\sim -0.3dB$. For 50:50 MMI, a symmetric stricture is used. The transmission responses for both ports are roughly the same, which are very close to the designed 3 dB splitting ratio, the loss at 1550nm is $\sim -0.5dB$.

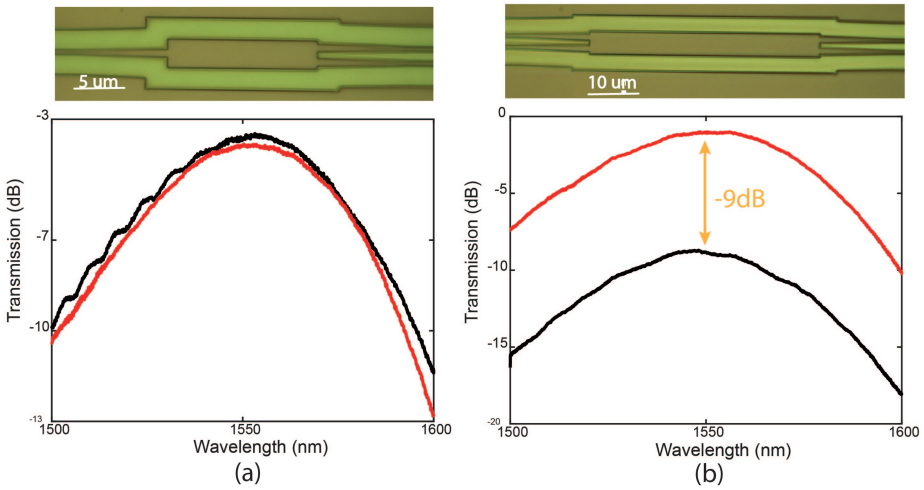

Figure 4.15: The fabricated MMI and its corresponding transmission. The red and black lines represent the transmissions from the upper and bottom ports, respectively. (a) 50:50. (b) 10:90.

4.2.3.2 DBS-optimized power splitters

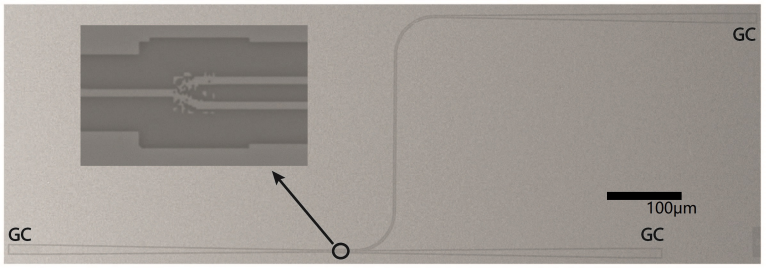

Figure 4.16: The SEM image of the whole device. The insert is the main part of the power splitter.

The top view of Scanning Electron Microscopes (SEM) of a whole power splitter is shown in fig. 4.16. TE-polarized grating couplers are used as the input and output of the device. Bend waveguides are used to separate two outputs by enough distance, which makes it easy for the alignments between the fibres and the GCs during the test. The light is coupled in and out at 18° tilt, and the coupling loss of for each GC is 6 dB at 1550 nm. The top view SEM image of each fabricated pattern is shown in the insert of fig. 4.17. Due to the imperfection of the fabrication process, it can be seen that some of the square pixels become round pixels and some pixels disappear. However, the experiment results still show good agreements with the simulations, which indicates a high fabrication tolerance of the devices.

Fig. 4.17 shows the transmission responses of the designed power ratios. The maximum error is observed in short wavelength range, where the transmission from the upper port of the 30:70 power splitter drops from -1 dB to -3 dB at 1545 nm. For other splitter ratios, flat transmissions are obtained over a wavelength range from

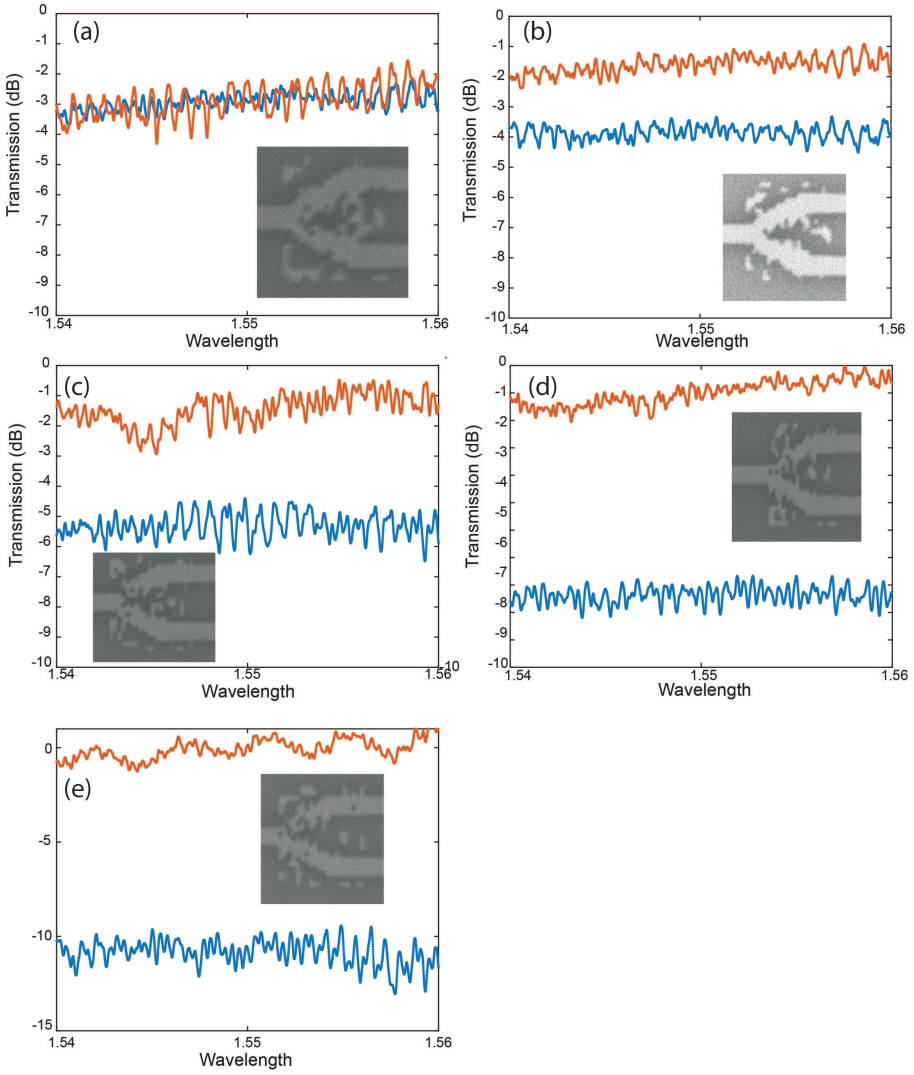

Figure 4.17: The measured spectrum of the fabricated power splitters using DBS algorithm. The red and blue lines represent the transmissions from the upper and bottom ports, respectively. The insets are the zoomed-in SEM images of the devices. (a) 50:50. (b) 40:60. (c) 30:70. (d) 20:80. (e) 10:90.

1540 nm to 1560 nm. During the measurement, it is also found that some ripples can be observed from the spectrum. There are several reasons for the appearance of these ripples. Firstly, during the fabrication process, there can be imperfections or variations in the physical structures that deviate from the ideal design. These imperfections can lead to scattering or mode coupling, introducing additional noise in the spectral response of the device. Inverse design methods often create intricate and complex structures that are highly sensitive to fabrication tolerances. Small variations in material properties, dimensions, or etching depths can lead to deviations from the desired device performance, resulting in increased noise in the spectral response. In this design, the minimum feature size is 100 μm, which requires highly accurate fabrication process. Any miss-etching or over-etching of pixels will lead to the reduction of the performance. Secondly, a bend waveguide is used when measuring

one of the output ports of the device, as shown in fig. 4.16. The mode mismatch between the straight and bend waveguides will also lead to the increase of the noise.

4.2.3.3 Distance measurement between two tiny grooves

Fig. 4.18 (a) is the microscope image of the on-chip OFDR system. The FUT, MI adn AI are marked on the figure, respectively. The FUT consists of a 400μm-long straight waveguide and a GC, the waveguide is etched with two tiny grooves, the distance between them are varied from 4.23μm to 19.88μm, which are shown in Fig. 4.18 (c)-(e). When the light signal from the MI enters the FUT and interacts with the defects from the waveguide, the back-reflected signal will be generated and transferred back to the MMI in the MI. As shown in fig. 4.18 (b), the back-reflected signal (red) and the signal from the reference arm (blue) will interfere at the MMI and generate the beat signal, which will be coupled out and captured by photodetector.

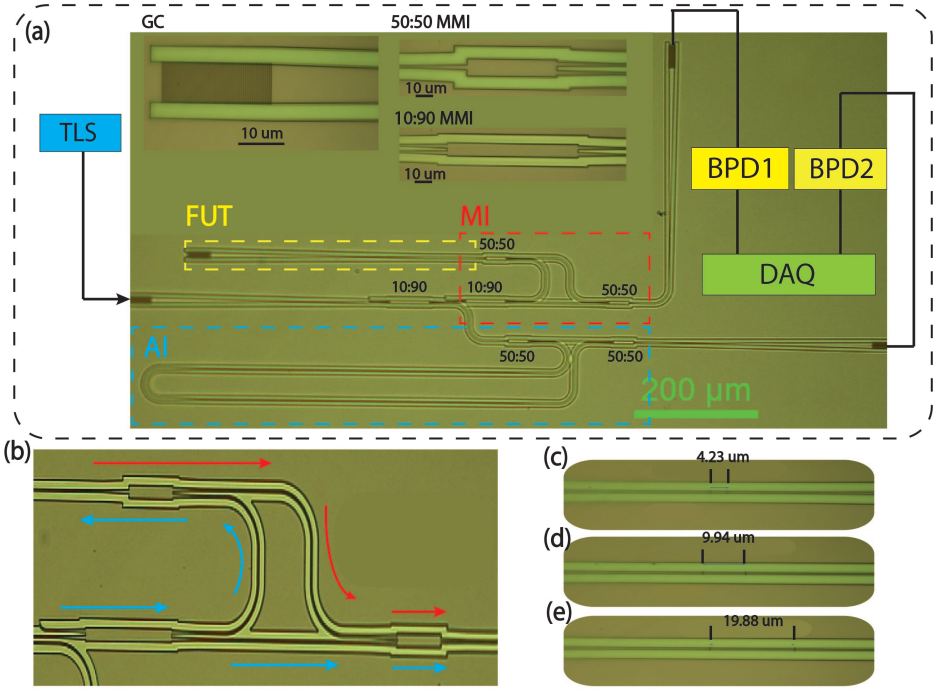

Figure 4.18: Microscope image of the on-chip OFDR system. (a) The system overview. The light from a tunable laser source (TLS) is coupled to the waveguide using grating couplers (GC). Two output signals, one from MI and one from AI, are captured by two photodetectors (BPD 1 and 2), respectively. The inserts in (a) are the zoomed-in image of the fabricated GC and MMI. (b) The zoomed-in image of MI. The blue arrow represents the signal from the TLS and the red arrow represents the back-reflected signal from the grooves and GC. (c-e). The zoomed-in images of the etched grooves. The distance between grooves are (c) 4.23μm, (d) 9.94μm and (e) (c) 19.88μm, respectively.

In the experiment, a tunable laser source (TLS) with the wavelength sweeping range of 43nm is used. The tuning speed is 100nm/s. According to Eq. 4.28, the theoretical

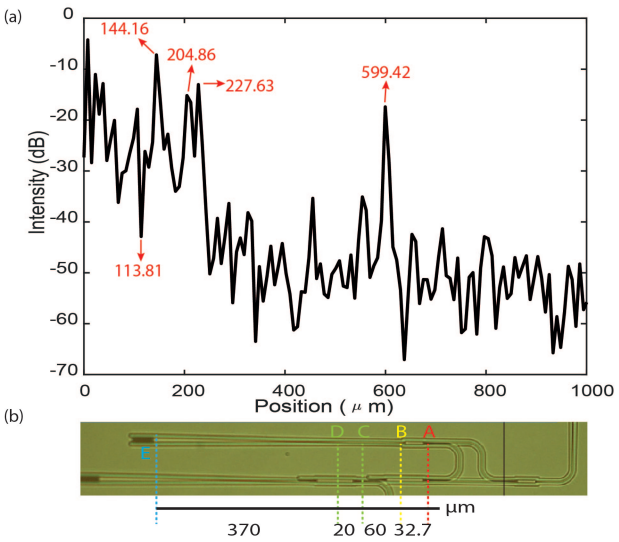

Figure 4.19: (a) Spatial domain distribution. Peaks at 113.81μm, 144.16μm, 204.86μm, 227.63μm and 599.42μm are the positions A, B, C, D and E shown in (b), respectively. (b)The actual measured distance between specific positions. A: The right side of MMI. B: The left side of MMI. C: The first groove. D: The second Groove. E: the right side of GC.

spatial resolution is 7.5um. The beating signal from MI and the clock signal from AI are then processed using the signal processing method from section. 4.1.5 [136] to obtain the spatial domain distribution. The result is shown in fig. 4.19 (a), the first peak appears at 113.81μm, which is equal to half of the optical path difference between the test arm and the reference arm. Therefore it represents the starting point of the FUT, which is the right-side of MMI (position A in fig. 4.19(b)). The next peek appears after 30.35μm, which corresponds to the length of the MMI (position B in fig. 4.19(b)). Then, after 60.7μm, two peaks with a distance of 22.77μm are observed, which are the two grooves etched on the waveguide (position C and D in fig. 4.19(b)). The last peaks appears at 599.42μm, which corresponds to the right-side of GC (position E in fig. 4.19(b)). The results show great agreement with the actual measured distance shown in fig. 4.19(b).

In fig. 4.19 (a), there are three data points exiting between 204.86μm and 227.63μm, therefore the spatial resolution is 7.59μm, which is very close to our theoretical result. The spatial resolution can be improved by expanding the wavelength sweeping range of laser. However, it will also induce more noise to the system.

4.3 Conclusion

In this section, starting from theoretical analysis, we study the working principle of traditional OFDR system first. Based on that, a novel on-chip OFDR system is designed and fabricated. The device is based on a standard 220nm- SOI platform, the

footprint is under $100\mu m^2$. The experiment results shows that the system achieves a spatial resolution of $7.9\mu m$, which is very close to the theoretical results. The components in the system are designed by traditional methods and photonic inverse design approach, respectively. The measured results show that both methods achieve great performances, but the footprint of the inverse-designed-components is at least 20 times smaller than the devices designed by traditional methods, which is very essential for ultra-compact photonic circuit.

Chapter 5

Monolithically integrated polarization rotator and splitter with designed power ratio

From chapter one, we have seen the advancements of the photonic inverse design and its feasibility for designing ultra-compact PIC. In this chapter, this method will be further discussed. Focusing on the main defects of this method, which is the cost of high computation power, we introduce the Gereral Stoke's theorem to improve the optimization efficiency of the inverse design method. As a result, we design a monolithically integrated polarization rotator and splitter with designed power ratio using the modified DBS algorithm. They potentially provides our on-chip OFDR system with a new detecting scheme, which will further reduce the footprint and the cost of our device.

Inverse designs have been widely used to design nanophotonic devices [32, 126, 83, 127]. The design algorithms allow the users to "design by specification" [128]. Some common algorithms include gradient-based adjoint method [137, 111], non-linear direct binary search (DBS) [138, 87], genetic algorithm [91, 89] and neural network [139]. Compared with conventional designs which strongly depend on physical theory and intuition of researchers [140], the inverse designs can optimize larger parameter space without being over-dependent on physics intuition [141]. These designs allow the realization of ultra-compact photonic devices with sophisticated functionalities [32, 83, 126, 127, 128, 137, 111, 138, 139, 140, 141]. The reported devices, such as power splitters [83, 127, 141, 87, 91, 139], polarization rotators [142, 89, 82], mode converters[126, 79, 80, 81], have been realized within a footprint under 10 μm^2. [81] achieved multi-functionalities and integrated mode conversion and power splitting into one device using a modified rotatable DBS. However, when two or more functions are integrated into one photonic device, it can be difficult to optimize the

design for the whole device, due to slower convergence or being stuck in a "local-maximum" [81]. In addition, the time complexity of DBS grows exponentially with the device scale and can be very time-consuming [112].

To reduce the design complexity, we use General Stoke's theorem to simplify the design space in the inverse designs. This method is widely used in fibre optical systems [11, 143], which divides a complicated system into several building blocks with individual functionalities, and then suitable optical components are selected to realise the objectives of the functionalities. The optical components are selected based on physical intuition and understanding of the system architecture. The individual functional component is connected by fibre connectors [52]. We propose to apply similar physical design intuition of the macro-system to the on-chip photonic design, which divides the device into several embedded inverse-designed sub-regions(mini building blocks), where General Stoke's theorem underlines the physical principle. Each sub-region is optimized by DBS independently to achieve the desired functionality, which will then be used as building blocks to achieve the complete multiple functionalities. Therefore, the whole area-design space optimization is replaced by parallel optimizations of sub-regions, which effectively reduces the optimization complexity and computation time.

To validate our method, we design, fabricate and test a monolithically integrated polarization rotator and splitter with a designed power ratio. The device can fulfil both polarization rotation (TE_{00} to TE_{00} and TM_{00} modes) and power splitting with a designed power ratio. The initial optimization area is separated into three sub-regions; the performance of each sub-region is measured by a figure of merit (FOM), which is optimized using DBS independently. The same constraints are applied to the adjacent boundaries of the sub-regions as design objectives. In this paper, TE_{00}:TM_{00}=1:1, 1:3 and 3:1 are designed and simulated with the largest footprint of $5.6 \times 2\mu m^2$. The device with TE_{00}:TM_{00}=1:1 is fabricated as an experimental demonstration, the measured maximum insertion loss is 1 dB and the crosstalk between TE_{00} and TM_{00} modes is less than -9.5 dB. Moreover, the overall computation time for sub-regions optimization is around five times shorter than the whole area optimization via the conventional method. Our method is proven to be an effective method for integrating multi-functionalities into a single photonic device with significantly reduced computational time.

5.1 Design principle

In vector calculus and differential geometry, the Generalized Stoke's theorem discusses the integration of differential forms on manifolds, which both simplifies and generalizes several theorems from vector calculus. It underlines a design process of

breaking down a relatively complex system into a series of simple ones, or a process of merging these simple pieces into the original one. The theorem says that the integral of a differential form over the boundary of some orientable manifold is equal to the integral of its exterior derivative over the whole of the manifold. For example, the 2-D Green's theorem as one special case of the generalized Stoke's theorem defines that the integral of the curl of a vector over the area equals the line integral of this vector around the perimeter.As shown in fig. 5.1, the block is cut into small pieces and each has its own circulations. The circulations with reversed directions can cancel each other. Therefore, the circulations from all internal edges cancel out, and on the boundary all the arrows add together to form a giant circulation.

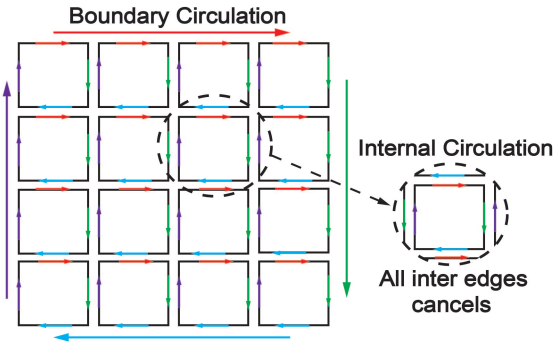

Figure 5.1: Green's theorem describes the external boundary and internal circulation

Mathematically, the General Stoke's theorem is given by [144]:

$$\int_{\partial M} \omega = \int_{M} d\omega. \tag{5.1}$$

M is the region where a function ω is defined and ∂M is the boundary of this region. Eq. (5.1) indicates that the integral of the derivative of ω over M is equal to the integral of ω over the boundary of M. Taking the electrostatic field as an example, dω represents the change in electric field of a single charge, which is the divergence. If there is a closed surface ∂M, the sum of all electric field changes from the charges inside the region M, represented as $\int_M d\omega$, is always equal to the total changes on its surface ∂M, namely the flux. The divergence is a local property, which zooms in and focuses on small changes. While the flux is a global property and describes the changes overall. The General Stoke's theorem governs the relationship between these two properties.

Additionally, assuming that the region M is the superposition of n sub-regions, the right-hand side of Eq. (5.1) can be rewritten as:

$$\int_{M} d\omega = \sum_{n=1} \int_{M_n} d\omega_n = \sum_{n=1} \int_{\partial M_n} \omega_n. \tag{5.2}$$

and when combined with the left-hand side, it becomes:

$$\int_{\partial M} \omega = \sum_{n=1} \int_{\partial M_n} \omega_n. \tag{5.3}$$

According to Eq. (5.3), all (k+1)-dimensional derivative terms have been replaced by k-dimensional boundary terms, therefore, the boundary condition of a region can induce the internal field functionalities.

The Generalized Stoke's theorem inspires a novel design methodology to design multiple functional photonic devices. In the method, we focus on the design of the external boundaries and the adjacent boundaries between sub-regions. Therefore, the multiple functionalities of a large design region can be split into several single functionalities with smaller sub-design regions. The optimization complexity can be significantly reduced.

Our design method is applied to DBS design. The optimization complexity is significantly reduced. We discrete the design region into m pixels, and assume each pixel has two states "0" and "1"(in this case, "0" refers to silicon while "1" refers to air). Then, the complexity of optimizing this region is defined as 2^m, which exhausts all the possibilities. Now, assuming the region is divided into n sub-regions, the complexity of optimizing each sub-region will be $2^{\frac{m}{n}}$. Thereby the total complexity is reduced by 2^n times theoretically, which not only improves the overall optimization efficiency but also avoids the "local-maximum" issue effectively.

However, Eq. (5.2) has assumed a linear superposition process, which requires that each sub-region is independent of the other. The term "independent" means the original electric field distribution of each sub-region remains unchanged after the merge of sub-regions. This requirement needs further consideration. The change in the local refractive index introduced by the change in the surrounding environment will inevitably impact the original electric field distribution after the merge. This will affect the originally-designed boundary conditions. Thus, additional constraints must be added to the boundaries of adjacent regions to reduce the impact, which will be discussed in the following sections.

5.1.1 The design of the monolithically integrated polarization rotator and splitter with various power ratios

To validate the proposed method, we design a monolithically integrated polarization rotator and splitter with various power ratios. TE_{00} mode is chosen as the input and three different output ratios of TE_{00}:TM_{00}=1:1, 1:3, 3:1 are numerically demonstrated. Fig. 5.2 (a)-(c) are the schematic views of the three designs. The solid lines represent the boundaries connected to the external environment (air), and the dashed lines are

the boundaries subjected to the inner connections. In the design, the whole region is divided into four sub-sections, including the power splitting section, the mode conversion section, the polarization rotation section and the buffering section.

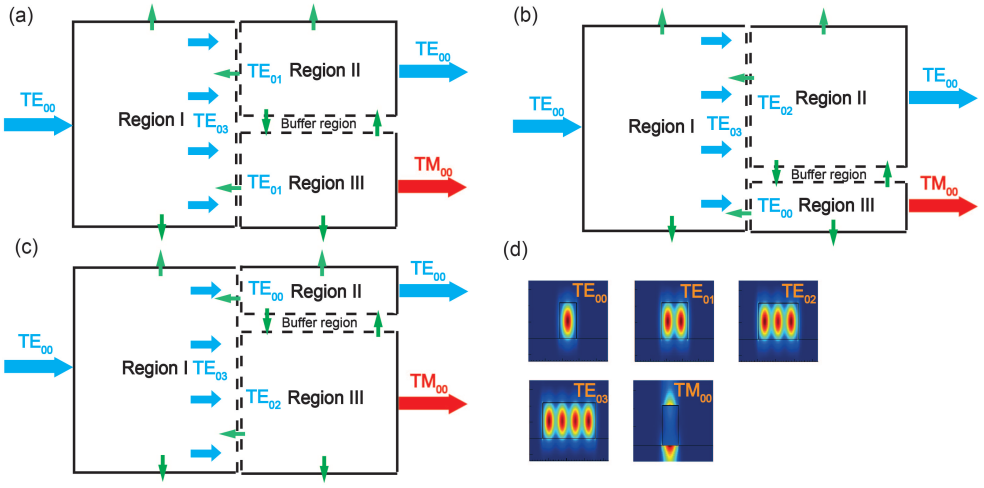

Figure 5.2: (a)-(c) Schematic views for TE_{00}:TM_{00}=1:1, TE_{00}:TM_{00}=3:1 and TE_{00}:TM_{00}=1:3 respectively. Region I is the power splitting section, Region II is the mode conversion section and Region III is the polarization rotation section. The green arrows represent possible light leakages considered in this paper (d). The cross-section of the ideal input and output modes mentioned in (a) to (c).

For the power splitting section, the Region I. TE_{00} mode is injected from the left-side boundary, and the target is to obtain an equally-distributed TE_{03} mode on the right-side boundary. To ensure the target mode is equally distributed, the cross-section of the right-side of Region I is equally divided into four parts, and each of which can be regarded as a separate TE_{00} mode (as shown in Fig. 5.2 (d)). The FOM in this region is defined as:

$$FOM_I = \alpha \cdot E_{TE_{03}} - (1-\alpha)[\sum_{n=4}(E_{TE_{00}^n} - 0.25)]. \tag{5.4}$$

where E is the transmittance of mode power. The α is a parameter used to correct the power ratio of each TE_{00} mode under TE_{03} mode, making each of them 25 % of the total power. In this way, the total power is expected to be equally allocated to the four TE_{00} modes within smaller areas. The different power ratios can be realized by the combined superpositions among these four modes. Light is strongly confined in the core due to the significant refractive index difference between silicon and air, so the losses on the upper and bottom boundaries are assumed to be zero in the simulation.

Mode conversion and polarization rotation are conducted in Region II and Region III, respectively. The equally-distributed TE_{00} modes from Region I are the input for Region II and Region III.

For the designed power ratio of TE_{00}:TM_{00}=1:1, as shown in Fig. 5.2 (a), each small blue arrow represents one equivalent TE_{00} separated from TE_{03} mode. The input mode of each region is defined to be TE_{01}, which is composed of two TE_{00} modes in space. The width of each region is designed to be half of the width of Region I so that the upper and lower two TE_{00} modes, corresponding to 50 % of the total power, can be confined in the two regions, respectively.

For the designed power ratio of TE_{00}:TM_{00}=3:1, as shown in Fig. 5.2 (b), the width of Region II and Region III is designed to be three-quarters and one-quarter of the width of Region I, respectively. The input mode is chosen to be TE_{02} for Region II and TE_{00} for Region III, respectively. Similarly, for TE_{00}:TM_{00}=1:3, we take the same philosophy to divide the boundary, but this time one-quarter of the width of Region I is for Region II. Also the chosen mode for Region II is transfered to TE_{00}. The process is shown in Fig. 5.2 (c).

For Region II and III, different FOMs are used to evaluate the performance of the final outputs:

$$\text{Region II} : FOM_{II} = E_{TE_{00}} - R_1. \tag{5.5}$$

$$\text{Region III} : FOM_{III} = E_{TM_{00}} - R_2. \tag{5.6}$$

The reflections R_1 and R_2 from Region II and Region III to Region I are monitored. The reflections should be minimized to reduce the impact on the output of Region I when the regions are merged. The interaction between Region II and III has not been considered yet, and each region is optimized separately. Light is supposed to be strongly confined in the core region due to the large refractive index difference. The interactions between Region II and Region III will be considered and re-optimized in the buffer region.

After optimizing three regions independently, we merge Region II and Region III, which leads to the merge of adjacent boundaries. The merge results in refractive index change and affects the original light path. To compensate the change, parts of Region II and Region III are re-designated as a buffer region, which will be re-optimized to reduce the impact of the merge. The FOM for buffer region is defined as:

$$FOM_{BR} = E_{TE_{00}} + E_{TM_{00}} - (L_1 + L_2). \tag{5.7}$$

where L_1 and L_2 monitor the light leakage from Region II and Region III to the buffer region respectively. Only the patterns in the buffer region are re-optimized to improve the FOM_{BR}. Then, Region I is added to the front end of Region II and III to form a complete device. Here, a buffer region is not needed between Region I and Region II (III). During merging Region I and the rest regions (Region II, Region III and buffer region), the mode power at the end of Region I and the mode powers at the final outputs are monitored. It is found that the mode power at the end of Region I is

slightly affected, and the overall mode power loss induced by the merge is less than 5 %. Therefore, no added buffer is utilized in the optimization process.

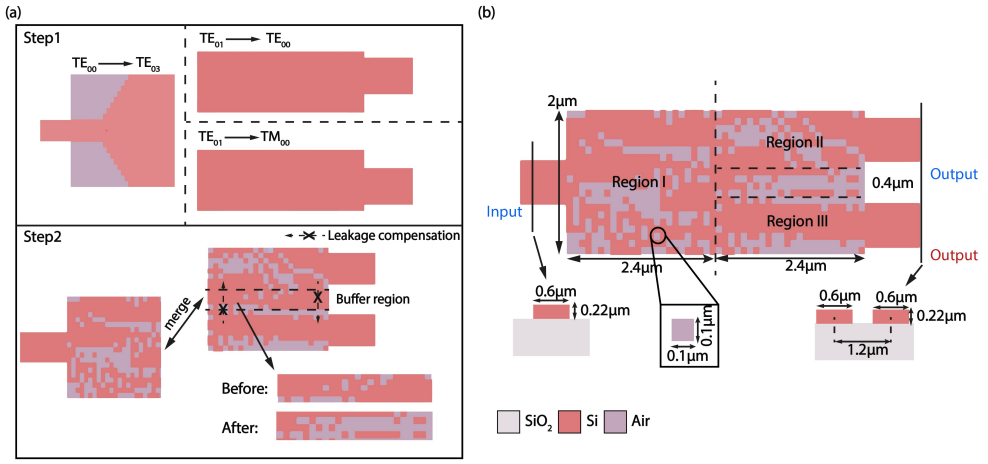

Figure 5.3: (a) The simulation steps for the proposed device. (b) Optimized structure of TE_{00}:TM_{00}=1:1.

The DBS method is employed to complete the optimization process [**11**]. As presented in Fig. 5.3 (a), the proposed structure is optimized by two steps. In step one, three regions are optimized independently to achieve the optimal FOMs mentioned above. For Region I, a manually-set initial pattern is used to avoid local convergence, as the design method is sensitive to the initial patterns [**14**]. Region II and Region III are optimized, starting from all-silicon. In step two, Region II and Region III are connected by the buffer region. When the optimization of the buffer region is completed, all regions are merged to form the final device, as shown in Fig. 5.3 (b).

Fig. 5.3 (b) shows the model of TE_{00}:TM_{00}=1:1. The device is based on an SOI platform with a 220 nm-thick top silicon layer. The widths of the input and output waveguides are 600 nm, and the gap between the two output waveguides are designed to be 1.2 μm to avoid crosstalk. The footprint of the design region is $4.8 \times 2\mu m^2$, which is discretized into 100 nm $\times$ 100 nm pixels. Each pixel has two states: "0" represents silicon, and "1" represents air. The etching depth of the pixel is 220 nm. The design space of Region I is $2.4 \times 2\mu m^2$, which composes of 24$\times$ 20 pixels. For Regions II and III, the widths will fluctuate depending on the corresponding TE_{00}-TM_{00} power ratio. And the lengths can be increased if larger design space is needed. The bigger the difference in effective index between the input and output in Region II(III) is, the larger design space is required. The length for TE_{00}:TM_{00}=1:3 and TE_{00}:TM_{00}=3:1 is set to be 3.2 μm to increase the design space. The overall number of pixels is 32$\times$ 20 .

The 3D finite-difference time-domain (FDTD) method is utilized to calculate the FOM using Lumerical FDTD Solutions. The simulations finish when the FOM growth falls below 1%. The overall optimization time for TE_{00}:TM_{00}=1:1 is 17 hours, and it takes a bit longer for the other two ratios, which are within 20 hours. The optimizations are operated on the IRIDIS High Performance Computer Cluster.

5.2 Results and discussion

5.2.1 Performance evaluation

Fig. 5.4 illustrates the E_y and E_z electric field profiles and the transmission spectra for TE_{00}:TM_{00}=1:1, 1:3 and 3:1, respectively. The initial TE_{00} is gradually evolved into our expected modes with a specific power ratio based on the merged regions. For TE_{00}:TM_{00}=1:3 (Fig. 5.4 (d) and (e)), Region II only has TE_{00} mode transmission, and no mode conversion is happened.

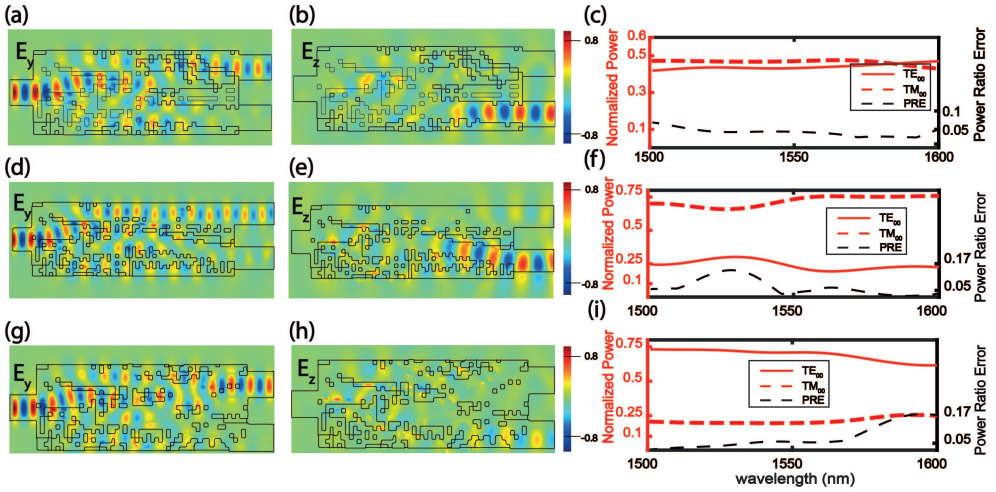

Figure 5.4: The calculated E_y and E_z electric field profiles at 1500 nm and transmission spectra under the wavelength range from 1500 nm-1600 nm for (a)-(c) TE_{00}:TM_{00}=1:1, (d)-(f) TE_{00}:TM_{00}=1:3 and (g)-(i) TE_{00}:TM_{00}=3:1.

To evaluate the accuracy of the designed power ratio, we define the actual power ratio minus the ideal power ratio as the power ratio error (PRE) [91], as summarised in Table 5.1. The PRE for TE_{00}:TM_{00}=1:1 is less than 0.12, and continuously decreases as the wavelength increases from 1500 nm and reduces to zero at 1590 nm. The overall transmission efficiency is above 85% over the wavelength range of 1500 nm-1600 nm.

Table 5.1: PRE of the three design ratios.

Power ratio error (PRE)			
TE:TM Power ratio	1:1	1:3	3:1
Maximum PRE	0.12	0.16	0.16

For both TE_{00}:TM_{00}=1:3 and TE_{00}:TM_{00}=3:1, the PRE is less than 0.16. For TE_{00}:TM_{00}=1:3, the peak of PRE appears within the wavelength of 1500 nm-1550 nm due to the descending transmission for TE_{00}. For TE_{00}:TM_{00}=3:1, the peak of PRE appears within 1550 nm-1600nm. The transmission of TE_{00} within 1550 nm-1600 nm is lower than that wtihin 1500 nm-1550 nm, but the transmission of TM_{00} is relatively

stable within the whole bandwidth. The overall PRE increases within 1550 nm-1600nm.

5.2.2 The effect of the buffer region on merging Region II and Region III

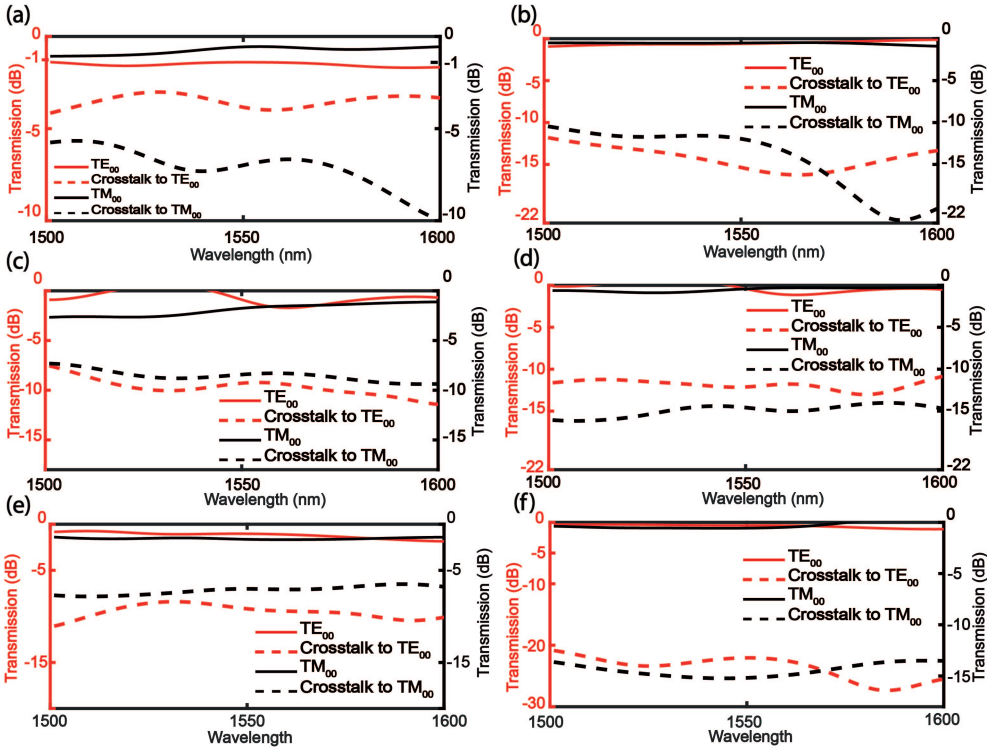

Figure 5.5: The normalized transmission spectra before and after adding the buffer region. (a)-(b) TE_{00}:TM_{00}=1:1. (c)-(d)TE_{00}:TM_{00}=1:3. (e)-(f) TE_{00}:TM_{00}=3:1

In addition, we also investigate the effects of the buffer region. The region width is initially chosen to be 0.4 μm to balance design space and simulation time. As shown in Fig. 5.3 (a), most of the buffer region is removed after the optimization because the buffer region is optimized to isolate Region II and Region III towards the extreme case of being physically separated. Also, most of the upper edge of Region III is removed, the buffer region modifies the bottom edge of Region II so that they can be isolated from each other. It found that buffer region improves the overall transmission by eliminating other higher-order modes introduced by merging Region II and Region III. Fig. 5.5 (a) and (b) illustrate the normalized output transmissions and crosstalks of TE_{00}:TM_{00}=1:1 before and after the buffer region is added. The crosstalk represents the difference between the target mode and the summation of other unwanted modes. The insertion loss is reduced by $\sim$ 0.8 dB for TE_{00} and TM_{00} modes. This is realized through physical isolation and converting other high-order modes to the target modes, where the crosstalk is decreased by at least 5 dB.

The buffer region also plays a vital role similar to the other designed power ratios. Its effect on the mode purity is as shown in Fig. 5.5 (c)-(f): The minimum crosstalk is decreased by 5 dB and 10 dB for TE_{00}:TM_{00}=1:3 and TE_{00}:TM_{00}=3:1, respectively. The merge of Region II and Region III has a relatively more significant impact on Region III. The refractive index of TM_{00} mode is relatively small and easier to be converted from other modes.

5.2.3 The impact of merging Region II and Region III into Region I

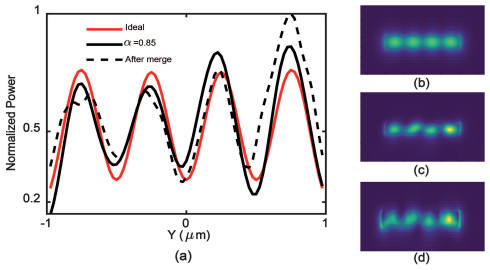

Figure 5.6: (a) The comparisons of normalized power distributions of the cross section at the end of Region I between the ideal, optimized and merged situations. (b)-(d) the corresponding electric field profiles of the cross sections

Despite contributions that have been made to the FOMs when optimizing Region II (III) to decrease the reflections from these regions to Region I, the output TE_{03} mode is still inevitably affected. A wide region of α is scanned for the FOM_I during the optimization of Region I to ensure that the maximum transmission of TE_{03} is obtained and each "small" TE_{00} is equally distributed. Ideally, the four TE_{00} modes are expected to be equally distributed within 0.5 μm width, and each one has 25% of the total net power. As indicated by the red line in Fig. 5.6 (a), each spike represents one separate TE_{00} mode.

The results of different α from 0.5 to 0.9 are analyzed: It is found that the electric field distribution at $\alpha = 0.85$, represented by the solid black line in Fig. 5.6 (a), shows the highest consistency with the ideal result. Electric field profiles of the ideal result and $\alpha = 0.85$ are shown in Fig. 5.6 (b) and (c), respectively. The optimized transmission for TE_{03} is 92%, and the amplitude error of each separated TE_{00} mode is less than 5%. The black dashed line in Fig. 5.6 (a) is the result after Region II and III are added. It shows that the highest amplitude of power of the 4th TE_{00} mode is increased by 5% from the ideal one. This inconsistency will affect the total power distribution and increase power ratio error for TE_{00} and TM_{00} at the outputs. The cross-section shown in Fig. 5.6 (d) indicates that the original elliptical light spots have been slightly deformed, especially for the first and second TE_{00} modes. The widths of these modes are also increased. The overall transmission decreases $\sim$ 6% after Region I is added.

5.2.4 The improved computational time and device performance

For comparison, a reference model of TE_{00}:TM_{00}=1:1 without region separation was optimized in the same design space using the normal DBS method, shown in Fig. 5.7 (b). The FOM of the reference device is defined as the summation of total power under TE_{00} and TM_{00} from the upper and lower output, respectively. Fig. 5.7 (a) shows the calculated FOMs of models with and without region separation, the simulation results are summarized in Table 5.2.

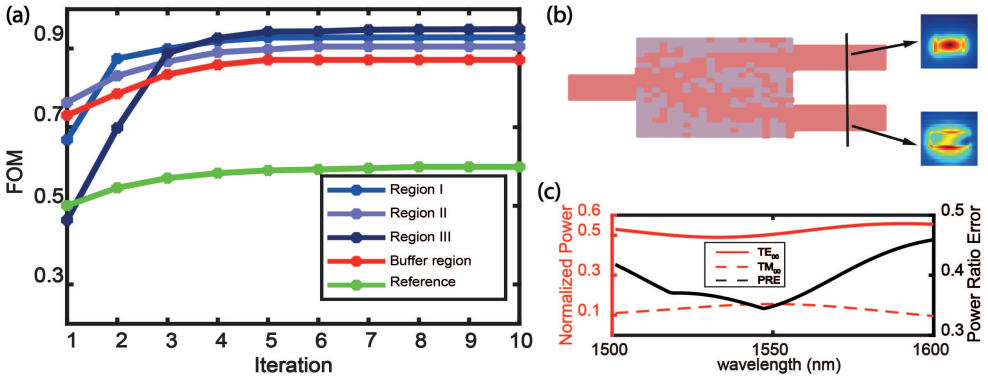

Figure 5.7: (a) The calculated FOMs of the proposed and reference models of TE_{00}:TM_{00}=1:1. The optimization time for Region I, Region II and Region III are 16 hours, 9 hours and 9 hours respectively. The re-optimization of the buffer region took 8 hours for 5 iterations. For the reference device, as the optimization space enlarges, it took 16 hours for only 1 iteration. (b) and (c) The optimized reference model and its transmission spectra. The inserts are the generated TE_{00} and TM_{00} modes, where TM_{00} is affected by high-order modes.

It takes 9 hours to optimize Region II and Region III. The optimization of the buffer region takes 8 hours for 5 iterations. The optimization of Region I takes 16 hours for the pattern to be generated. Using the parallel optimization method, the overall computational time is 17 hours.

The FOMs for the proposed device are above 0.85 after 5 to 6 iterations. The final FOMs for Region II and Region III are 0.91 and 0.93, corresponding to over 90 % of TE_{00} and TM_{00} mode power respectively. When two regions are merged without the buffer region, the overall transmissions for both modes decrease. The FOM_{BR} are by the red line in Fig. 5.7 (a). The initial FOM_{BR} of the buffer region is 0.72, it corresponds to ∼72% of total power, which is ∼ 20% lower than the output before merging. During the optimization of the buffer region, we monitor the mode powers (TE_{00} and TM_{00}) at the outputs. After five iterations, the mode powers for both modes increase ∼ 15%, and the corresponding FOM_{BR} raises from 0.72 to 0.87 and then stabilizes.

For the reference device, as shown by the green line in Fig. 5.7, the maximum FOM is 0.59. The corresponding TE_{00} and TM_{00} power are 48 % and 10 % respectively. The maximum PRE is 0.43, and most of its contribution comes from the error of TM_{00} mode. In contrast, the overall transmission of the reference device is 33% lower than

Table 5.2: The comparison between the proposed and reference models of TE_{00}:TM_{00}=1:1.

Region	Proposed device				Reference device
	I	II	III	Buffer region	
# Iterations before stabilization	5	6	5	5	8
Maximum FOM	0.92	0.91	0.93	0.87	0.59
Time cost (h)	16	9	9	8	80

the proposed one. Moreover, because there is no regional separation, the optimization process cannot be carried out independently. The iteration will require a much longer computational time. E.g. The recorded time for five iterations of the reference device is 80 hours.

5.3 Experimental verification

To evaluate our method, the device with TE_{00}:TM_{00}=1:1 is fabricated based on a SOI wafer with a 220-nm Si layer and 3-μm buried oxide layer. The fabrication process is the same as the power splitter in chapter 1. The wafer is firstly coated by 300-nm ZEP520A photoresist with espacer using resist spinner. Then, electron-beam lithography is used to form the pattern of the waveguide. After that, espacer is removed by DI water and the photoresist is developed using ZED-N50 developer. The inductively coupled plasma etching is then utilized to etch a depth of 220 nm. Finally, ellipsometry is performed to confirm the etching depth after etching. We also fabricate TE-type and TM-type grating couplers for coupling the target modes into or out of optical fibers. The etching depth for both types of grating couplers are 70 nm, and the fabrication process is the same as we mentioned above.

Fig. 5.8 (c)- (e) are the zoomed-in SEM images of the grating couplers and the device, respectively. To make sure TE_{00} mode is converted to TM_{00} mode, a reference device as shown in fig. 5.8 (a) is designed, the output TE_{00} and TM_{00} are coupled out by only TM-type grating couplers. The result is shown in fig. 5.8 (f), where the measured average transmissions for TE_{00} and TM_{00} modes are around -12dB and -3.5dB within the range of 1540nm to 1560nm, respectively. The smallest value for TE_{00} mode is -14 dB at 1560 nm, the average crosstalk is therefore below -9.5 dB when comparing the two modes. After confirming the effectiveness of TE_{00}- TM_{00} conversion, the device is then measured by TE-type and TM-type grating couplers shown in fig. 5.8 (b). The result is shown in fig. 5.8 (g). For TM_{00} mode, the average insertion loss is 0.6dB, the maximum value is around 0.7dB at 1550nm. For TE_{00} mode, the insertion loss is a bit higher within the region of 1540nm to 1546nm, which is around 1dB, the minimum insertion loss is 0.7 dB at 1550nm. Small ripples are also observed, as we mentioned in chapter four, photonic-inverse-designed device has high requirement for fabrication

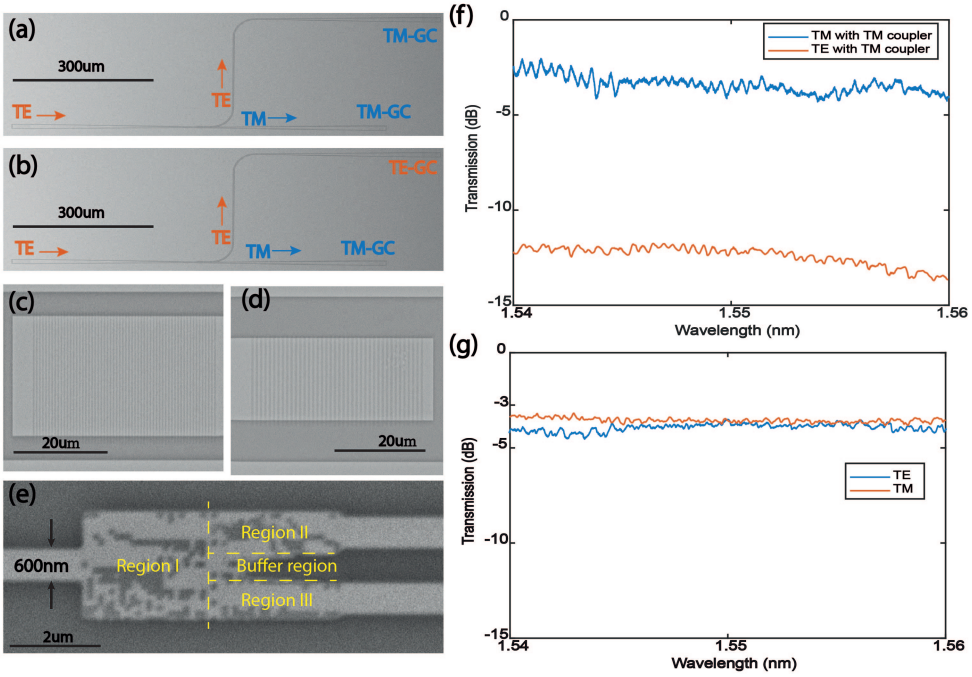

Figure 5.8: SEM of a TE:TM=1:1 device with (a) TE-input and two TM-outputs. (b) TE-input and upper-TE-output, bottom-TM-output. (c) and (d) The zoomed in SEM image of TE and TM grating couplers. (e) The zoomed in SEM image of the device. The experimental spectra for (f) TE-input and two TM-outputs, (g) TE-input and upper-TE-output, bottom-TM-output.

process. The variation of etching depth, or the missing of a single pixel, will lead to the increase of the noise. Overall, the measured data are in good agreement with the simulated results, which validates the feasibility of our method experimentally.

5.4 Conclusion

In conclusion, we combine the General Stoke's theorem and DBS to propose a novel design methodology. Based on the proposed method, the whole design region is separated into several sub-regions, which can be optimized simultaneously. The simulation complexity can be reduced by 2^n times theoretically. When sub-regions are merged, additional constraints are added to the adjacent boundaries to reduce the impact of the merge. Finally, sub-regions are merged to achieve the functionality of the whole device. As a validation, monolithically integrated polarization rotators and splitters with various power ratios are numerically designed. Device with TE_{00}:TM_{00}=1:1 is fabricated in our cleanroom to validate the design method, the measured results show that the maximum insertion loss is 1 dB (TE_{00} mode from 1540nm to 1546nm), and the average crosstalk is below -9.5 dB. There are two potential ways to further improve the crosstalk. Firstly, the size of each sub-region can be further enlarged to increase the design space. Secondly, the pixels can be partially

etched instead of fully etched to increase the mode conversion efficiency. There is a trade-off between the two potential ways, as large size requires longer optimization time and multiple etching steps bring extra fabrication complexity compared with a single etching step.

Different power ratios can be realized by changing the output mode of Region I and different combined superpositions of input modes of Region II and Region III, respectively. As the simulation complexity is decreased, the overall simulation time is 17 hours, which is around five times faster than the reference device. We envisage that our device will have more applications in on-chip pumping and probing system [145] and the generation of arbitrary first-order Poincaré sphere beams [146]. As long as sub-regions are carefully designed so that their boundaries are matched, our proposed method will give a solution for designing other multi-functional photonic devices.

Chapter 6

Optical mode localization sensing based on fibre- and silicon- coupled ring resonators

Compared with MEMS resonators, optical resonators exhibit several advantages. Optical ring or disk resonators can achieve high quality factors without using vibration structures and vacuum conditions [28, 29, 30]. These devices show great diversity in scale, with a variety of sizes from micrometers (waveguide) [147] to meters (fibres) [28], play a key role in integrated photonic circuits [148, 149, 150], sensing [7] and optical communication [3].

For optical resonators, resonant modes will be split when two resonators are weakly coupled [151]. By a localized perturbation, the induced changes in the refractive index and coupling coefficient will change the energy distribution to all resonant modes. These changes thereby result in asymmetrical splitting of the resonant modes. The symmetry feature of the mode splitting can be evaluated by the modal power ratio between two split modes, which can reflect the magnitude of the perturbation. Therefore the localized perturbation can be quantitatively measured by examining the modal powers of the split modes [26, 27, 63, 64].

This sensing mechanism can be embedded in optical waveguide/fibre systems to develop ultra-sensitive sensors. In this chapter, the theory of traditional MEMS-based mode localization sensing is introduced first. Then the optical mode localization is realized theoretically and experimentally in both fibre- and silicon- based coupled ring resonators.

6.1 Optical ring resonator

Optical ring resonator, as the main component to study the optical mode localization, will be discussed in this section. Firstly, a fundamental all-pass ring resonator is discussed. Then, coupled ring resonators, which is utilized for the optical mode localization, will be introduced.

6.1.1 All-pass ring resonator

An all-pass ring resonator contains a ring and a bus waveguide, which is shown in fig. 6.1.

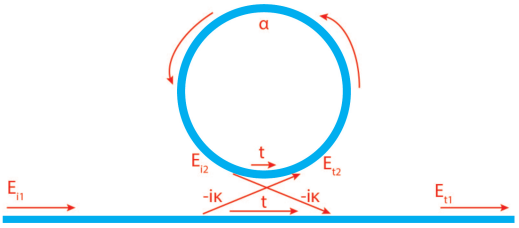

Figure 6.1: The schematic of an all-pass ring resonator

The light signal from the bus waveguide is evanescently coupled to the ring waveguide in the coupling region. The coupling region can be simply described by using a coupling matrix [152]:

$$C = \begin{pmatrix} t & -i\kappa \\ -i\kappa & t \end{pmatrix} \tag{6.1}$$

Then the coupling between the bus waveguide and the ring waveguide can be expressed as:

$$\begin{pmatrix} E_{t1} \\ E_{t2} \end{pmatrix} = \begin{pmatrix} t & -i\kappa \\ -i\kappa & t \end{pmatrix} \begin{pmatrix} E_{i1} \\ E_{i2} \end{pmatrix} \tag{6.2}$$

Where E is the complex mode amplitudes, its squared magnitude represents the modal power. t and κ represent the transmission coefficient and the cross-coupling coefficient, respectively. Assume the loss is zero in the coupling region, then

$$|t^2| + |\kappa^2| = 1 \tag{6.3}$$

The electric field amplitude in the ring waveguide can be expressed as:

$$E_{i2} = \alpha \cdot e^{j\theta} E_{t2} \tag{6.4}$$

Where α is the attenuation coefficient which related to the loss in the ring resonator. $\theta = \omega L/c$ is the phase shift per round trip, ω is the a angular frequency of the light, L and c are the circumference of the ring and the speed of light, respectively.

By combining Eq. 6.1 to Eq. 6.4, the modal amplitudes E_{t2}, E_{i2} and E_{t1} can be obtained:

$$E_{t2} = \frac{-i\kappa e^{i\theta}}{-\alpha t + e^{i\theta}} \tag{6.5}$$

$$E_{i2} = \frac{-i\kappa\alpha}{-\alpha t + e^{i\theta}} \tag{6.6}$$

$$E_{t1} = \frac{-(\kappa^2 + t^2)\alpha + t \cdot e^{i\theta}}{-\alpha t + e^{i\theta}} = \frac{-\alpha + t \cdot e^{i\theta}}{-\alpha t + e^{i\theta}} \tag{6.7}$$

Then the corresponding modal power at the output of the ring resonator can be expressed as:

$$P_{t1} = |E_{t1}|^2 = \frac{\alpha^2 + |t|^2 - 2\alpha|t|cos(\theta + \varphi_t)}{1 + \alpha^2|t|^2 - 2\alpha|t|cos(\theta + \varphi_t)} \tag{6.8}$$

where the phase shift experienced by light as it is coupled from the bus waveguide through the ring resonator is $\varphi_t = 2\pi\frac{d}{\lambda}\Delta n$, d is the length of the waveguide in the coupling region, λ is the wavelength of the light, Δn is the refractive index difference between the waveguide and the surrounding medium.

As an example, the transmission of a $10\mu m$-radius ring resonator over the wavelength from 1.53 μm- 1.57 μm is shown in fig. 6.2. The transmission coefficient t and the attenuation coefficient α are 0.9.

As we can see from the spectrum, sharp resonances and intense buildup of light occur inside the ring resonator at λ_{res} if the light is constructively interfered when the round trip length is an integer multiple of the guided wavelength [4]. In this situation, the transmission becomes:

$$P_{t1} = |E_{t1}|^2 = \frac{(\alpha - |t|)^2}{(1 - \alpha|t|)^2} \tag{6.9}$$

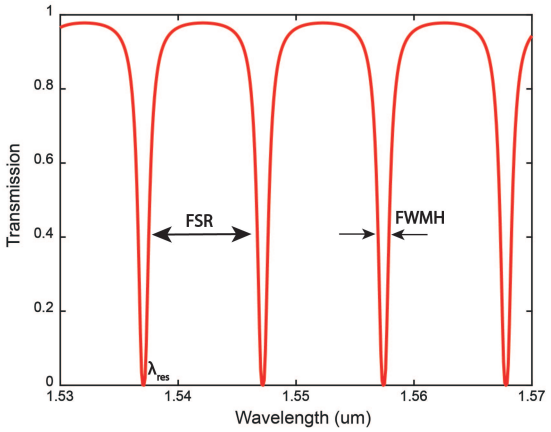

Figure 6.2: The transmission response of an all-pass ring resonator. The parameter is as follow: $\alpha = 0.9$, $t = 0.9$, the radius of the ring is 10 um, $n_{eff} = 3.4$, the surrounding material is air, the coupling length is 9 um.

In Eq. 6.29, one special case will happen if $\alpha = |t|$. When the attenuation coefficient is equal to the coupling coefficient, the transmission will become to 0. This is known as critical coupling [4].

The distance between each resonance peak is called free spectral range (FSR), which is equal to the wavelength changes of a 2π phase shift. The phase shift of a round trip of the ring resonator is:

$$\phi_r = \frac{2\pi n_{eff} L}{\lambda} \tag{6.10}$$

By taking the derivative with respect to the wavelength:

$$\frac{d\phi_r}{d\lambda} = (\frac{dn_{eff}}{d\lambda} - \frac{n_{eff}}{\lambda})\frac{2\pi}{\lambda}L = -n_{eff}\frac{2\pi}{\lambda^2}L \tag{6.11}$$

Then the FSR can be expressed as:

$$FSR = \frac{2\pi}{|d\phi_r/d\lambda|} = \frac{\lambda^2}{n_{eff}L} \tag{6.12}$$

The full width at half maximum (FWHM) evaluates the linewidth of a resonance, it can be expressed as:

$$FWHM = \frac{(1 - t\alpha)\lambda_{res}^2}{\pi n_{eff} L\sqrt{t\alpha}} \tag{6.13}$$

Finally, two parameters are frequently used to evaluate the performance of the ring resonator. One is the quality factor (Q-factor), which represents the ability to store

energy, it can be expressed as the ratio between the resonant wavelength and the FWHM:

$$Q = \frac{\lambda_{res}}{FWHM} = \frac{\pi n_{eff} L \sqrt{t\alpha}}{(1 - t\alpha)\lambda_{res}} \tag{6.14}$$

The other one is the finesse, which describe the occupation of the resonances over the spectrum. It is defined as the ratio between the FSR and the FWHM:

$$Finesse = \frac{FSR}{FWHM} \approx \frac{\pi \sqrt{t\alpha}}{1 - t\alpha} \tag{6.15}$$

6.1.2 Coupled ring resonator

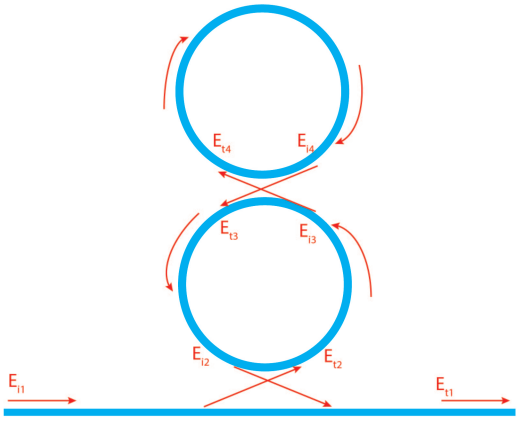

Figure 6.3: The schematic of a coupled ring resonator

A coupled ring resonator contains an all-pass ring resonator coupled by another ring waveguide, which is shown in fig. 6.3. There are two couplings in this schemes, one is the coupling between the bus waveguide and the ring resonator, the other one is the coupling between the two ring resonators. The model of the coupled ring resonator can be derived by using two coupling matrices [153]. One is the coupling matrix between the bus waveguide and the bottom ring resonators, the other one is the coupling matrix between the two ring resonators.

For the coupling between two ring resonators, the coupling matix can be expressed as:

$$\begin{pmatrix} E_{t3} \\ E_{t4} \end{pmatrix} = e^{i\beta L_0 - \alpha L_0} \begin{pmatrix} cos(\kappa_1 L_0) & isin(\kappa_1 L_0) \\ isin(\kappa_1 L_0) & cos(\kappa_1 L_0) \end{pmatrix} \begin{pmatrix} E_{i3} \\ E_{i4} \end{pmatrix} \tag{6.16}$$

Where E_{t3}, E_{t4}, E_{i3} and E_{i4} are the electric field amplitudes at the four ports of the coupling region, respectively. L_0 is the coupling length and β is the effective wave

propagation constant of the coupling area, which is related to the refractive index n_{eff} and the free-space wave vector.

In coupled ring resonator, two new modes are generated due to the coupling between the clockwise and counterclockwise light signals, which is called symmetric (S-) and antisymmetric (AS-) modes. [154]. The corss-coupling coefficient of the two ring resonators can be calculated by using the S- and AS- modes [155]:

$$\kappa_1 = \frac{\pi}{\lambda}(n_{S-} - n_{AS-}) \tag{6.17}$$

Where n_{S-} and n_{AS-} are the effective indices of the S- and AS- modes, respectively.

In addition, the relations between E_{i2} and E_{t3}, E_{i4} and E_{t4}, E_{i3} and E_{t2} can be expressed as:

$$E_{i2} = E_{t3}e^{i\beta L_1 - \alpha L_1} \tag{6.18}$$

$$E_{i4} = E_{t4}e^{i\beta L_2 - \alpha L_2} \tag{6.19}$$

$$E_{i3} = E_{t2}e^{i\beta L_3 - \alpha L_3} \tag{6.20}$$

Where L_1, L_2 and L_3 are the distances between E_{i2} and E_{t3}, E_{i4} and E_{t4}, E_{i3} and E_{t2}, respectively.

The coupling matrix between the bus waveguide and the bottom ring resonator is similar as the coupling for all-pass ring resonator, which can be expressed as:

$$\begin{pmatrix} E_{t1} \\ E_{t2} \end{pmatrix} = \begin{pmatrix} t & -i\kappa_2 \\ -i\kappa_2 & t \end{pmatrix} \begin{pmatrix} E_{i1} \\ E_{i2} \end{pmatrix} \tag{6.21}$$

Combining Eq. 6.16-Eq. 6.21, the output E_{i2} can be expressed as:

$$E_{i2} = \frac{-j\kappa_2(cos(\kappa_1 L_0)e^{i\beta L_0 - \alpha L_0} - e^{-i\beta L_2 + \alpha L_2})}{Det|E|}E_{i1} \tag{6.22}$$

where

$$E = \begin{pmatrix} E_{11} & E_{12} \\ E_{21} & E_{22} \end{pmatrix} \tag{6.23}$$

$$E_{11} = tcos(\kappa_1 L_0)e^{i\beta(L_0+L_1)-\alpha(L_0+L_1)} - e^{-i\beta L_3+\alpha L_3} \tag{6.24}$$

$$E_{12} = itsin(\kappa_1 L_0)e^{i\beta(L_0+L_1)-\alpha(L_0+L_1)} \tag{6.25}$$

$$E_{21} = isin(\kappa_1 L_0)e^{i\beta L_0-\alpha L_0} \tag{6.26}$$

$$E_{22} = cos(\kappa_1 L_0)e^{i\beta L_0-\alpha L_0} - e^{-i\beta L_2+\alpha L_2} \tag{6.27}$$

Finally, the corresponding electric field amplitude at the output of the coupled ring resonator can be derived by combining Eq. 6.21-Eq. 6.27:

$$E_{t1} = \frac{j\kappa_2 E_{i2} e^{-i\beta L_3+\alpha L_3}}{tE_{i1}} + \frac{1}{t} \tag{6.28}$$

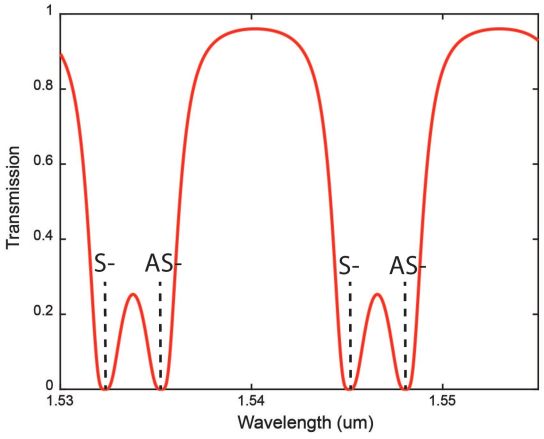

Figure 6.4: The transmission response of an all-pass ring resonator. The simulation is based on the following parameters: $\alpha = 0.5$, $\kappa_1 = \kappa_2 = 0.5$, the circumference of each ring resonator is $r = 70um$, and $L_0 = L_1 = L_2 = L_3 = L_4 = 10um$.

Based on Eq. 6.28, the transmission spectrum at the output of the coupled ring resonator is calculated, which is shown in fig. 6.4. It can be seen that mode splitting occurs and two new modes (S-mode and AS-mode) are generated. According to the coupled mode theory (CMT), the resonant wavelength of the S-mode is smaller than that of the AS-mode [156]. Therefore, the left is the S-mode and the right is the AS-mode. In fig. 6.4, critical coupling is achieved, where the on-resonance transmission drops to zero. The spectrum is based on two identically coupled ring resonators, which results in evenly-split resonant modes. When external perturbations are induced to the resonators, the symmetry of the mode splitting will be broken. This

phenomenon refers to the optical mode localization, which will be discussed in the next sections.

6.2 Optical mode localization sensing based on fibre-coupled ring resonator

In this section, the optical mode localization sensing based on fibre-coupled ring resonator is investigated numerically and experimentally. Two different coupled ring resonators (Device A with the coupling coefficient $\kappa = 0.1$ and Device B with $\kappa = 0.5$. κ refers to the efficiency of power transfer between the resonator and the input/output fibres.) are fabricated. By tuning the thermal perturbation, the variations of the amplitude difference between the split modes are measured. For Device A, the difference can be tuned from -6% to -2% as the temperature variation increases from 0K to 8.5K, the corresponding variation rates are $\sim$ -0.41%/K and $\sim$ 0.39%/K when the upper and bottom rings are heated, respectively. In contrast, For Device B, the difference can be tuned from 2.5% to 22.5% when the temperature variation increases from 0K to 8.5K, the corresponding variation rates are $\sim$ -2.2%/K and $\sim$ 2.4%/K when the upper and bottom rings are heated, respectively. The demonstrated results exhibit three orders of magnitude improvement in the sensitivity in terms of variation rate to the temperature changes comparing with the variation rate of the thermally-induced frequency shift. Combining the advantages of optical fibres, we provide a new way for ultra-sensitive fibre temperature sensing.

6.2.1 Experiment setup

Figure. 6.5 is the experimental setup of the system. The coupled ring resonators are produced by fusion-splicing the output ports of 2×2 single-mode fibre couplers (Thorlabs-TN1550R5F2) to their input ports. The circumference of each ring resonator is around 50 cm. A tunable laser source (PPCL550) with the linewidth of 1 MHz is used to measure the resonance response of the coupled ring resonator. A polarization controller (PC) is placed after the laser to ensure only one eigenmode is excited to the device [28]. The light signal from the output of the coupled ring resonator is captured and measured by a photodetector (TIA525) and an oscilloscope (Pico scope 6404D).

In this experiment, the critical coupling is desired to ensure a high extinction ratio (ER). However, due to the unavoidable losses induced by the fibres, couplers and fusion splices, it is hard to achieve critical coupling by using fibre couplers with fixed coupling coefficients. Here, two coupling coefficients ($\kappa = 0.1$ and $\kappa = 0.5$) are used to form two devices (Device A and B), and their performances are compared.

For a single device, there are two couplings existing in the system, one is the coupling between the input fibre and the resonator, the other one is the coupling between two resonators. Therefore, when $\kappa = 0.1$, it means 10% of power from the input fibre will be coupled into the first resonator, then 10% of power from the first resonator will be coupled into the second resonator. When $\kappa = 0.5$, 50% of power from the input fibre will be coupled into the first resonator, then 50% of power from the first resonator will be coupled into the second resonator.

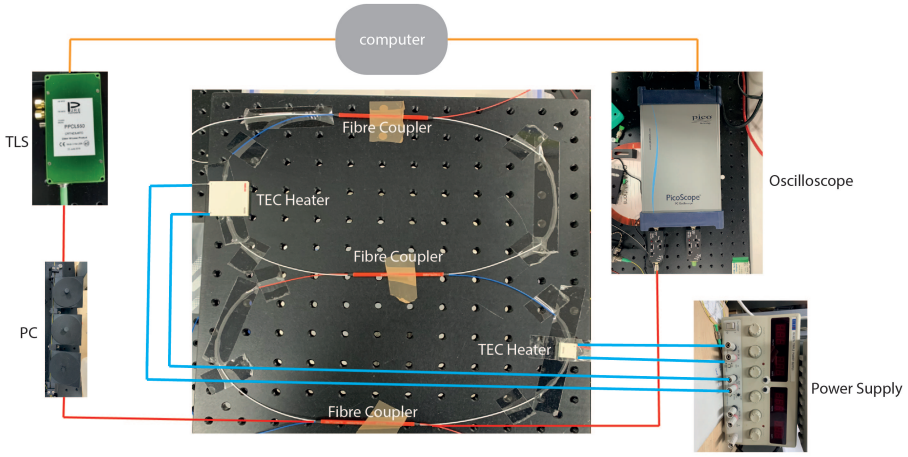

Figure 6.5: The experimental setup of the system. The device consists of two coupled ring resonators, which are formed by three fibre couplers. Two thermoelectric (TEC) heaters placed on the upper and bottom rings are used to induce thermal perturbation. The uneven distribution of optical energy will occur when only one of the heaters is utilized.

6.2.2 Transmission spectrum for the devices with different coupling coefficients

The spectrum of the devices without thermal perturbation is shown in figure. 6.6. The split notches M1 and M2 in the spectrum indicate two split resonant modes, which are called symmetric and antisymmetric modes [151, 157]. For one mode, the ER is defined as the difference between the on-resonance and off-resonance transmissions [147, 158]. To maximise ER, the coupling coefficient κ and attenuation coefficient α have to be equal to reach the critical coupling. Figure. 6.6 (a) displays the transmission spectrum of Device A. In this situation, the maximum ER is 0.15, which indicates a massive gap between the κ and the α. Device B is also examined, which is shown in figure. 6.6 (b). It shows that when the κ is increased, the maximum ER increases from 0.15 to 0.4, which enlarges the initial ER by 160%. It is also found that the enlarged ERs significantly improves the device's sensitivity to the temperature changes, which will be discussed later. It should be noticed that the initial ERs of the split modes shown in figure. 6.6 are different. This is because the two fabricated fibre-coupled ring resonators are not identical due to fabrication imperfection. Nevertheless, this will not

affect the measurement because each time before the temperature is measured, the response without temperature perturbation is measured first and it will be used as an initial benchmark. When temperature perturbation is induced, the actual temperature change will be measured by the difference between the response and the pre-set benchmark.

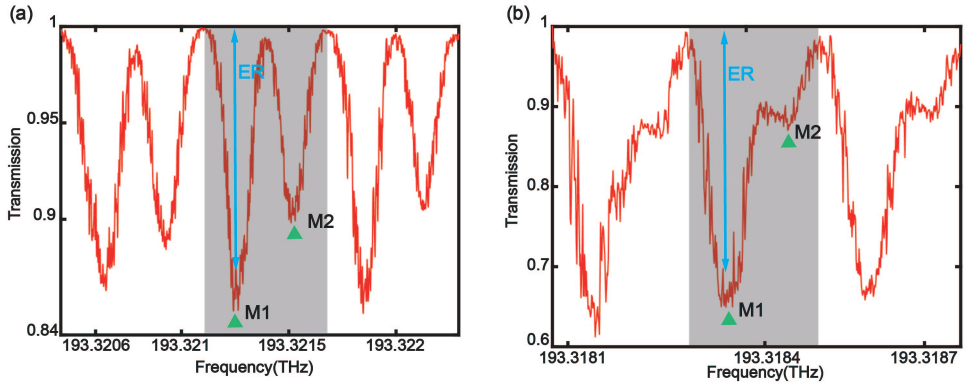

Figure 6.6: Measured spectrum of the devices with different coupling coefficients: (a) Device A with $\kappa = 0.1$ and (b) Device B with $\kappa = 0.5$. The split notches M1 and M2 are the two split resonant modes. The gray area represents one period.

6.2.3 Simulation results

6.2.3.1 Fitting of the measured data

Figure. 6.7 (a) and (b) display the theoretical fits to the measured spectrum. The fitting functions are calculated by using the transfer matrix method [159], and also verified by the Lumerical interconnect module simulation. Before doing further analysis, a smoothing function is utilized to remove the glitches of the signal. Compare with the raw data shown in figure. 6.7, most glitches are removed after smoothing by a Gaussian window and the processed signals show good fits with the theoretical models.

6.2.4 The ERs of the split modes when the devce is heated

In this experiment, the thermal perturbation is induced by two thermoelectric (TEC) heaters, placed on the upper and bottom rings, respectively. The heating length that the TEC heaters can cover is 1 cm. Due to the thermal-optical effect, the refractive index of the covered coupled ring resonators will change according to the induced temperature variation. The thermal-optic coefficient is $1.33 \times 10^{-5} K^{-1}$ for silica optical fibre; therefore there will be 0.0000133 refractive index changes per K. We simulate the transmission responses with temperature variations, and the results are shown in

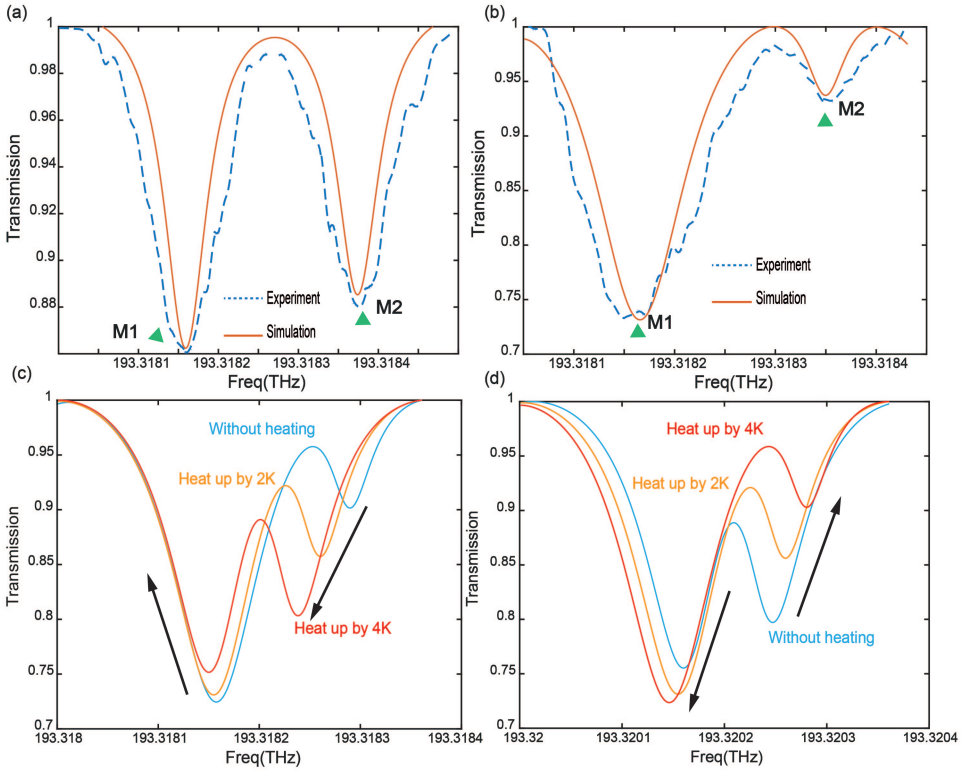

Figure 6.7: (a) The theoretical fits to the measured spectrum for Device A. (b) The theoretical fits to the measured spectrum for Device B. (c) and (d) The changes of two split modes when temperature perturbation is induced, the simulation is based on $\kappa = 0.5$. (c) when the upper ring is heated. (d) when the bottom ring is heated.

figure. 6.7 (c) and (d). It can be seen that the variations of the two split modes show opposite trends when different rings are heated up, respectively. In figure. 6.7 (c), only the upper ring is heated. When the temperature is increased by the value from 0K (Blue line) to 4k (Red line), the ERs of M2 increase from 0.1 to 0.22 while the ERs of M1 drop from 0.28 to 0.25. Comparing with only heating the upper ring, the variations of M1 and M2 will be different if only the bottom ring is heated, which is shown in figure. 6.7 (d). The ERs of M2 reduce from 0.22 to 0.1 and the ERs of M1 increase from 0.24 to 0.28 as the bottom ring is heated. These opposite changes are due to the optical mode localization effect, it induces unevenly distributed energy to the split modes, which will be discussed in the next section.

6.2.4.1 The energy distributions of the split modes when the device is heated

After comparing the transmissions between different heating positions, it is found that heating the upper ring will cause opposite changes on the ERs of the two split modes regarding to heating the lower ring. This is due to the induced uneven optical energy distributions of the split modes to the two rings when different rings are heated. Based on our previous work, when the temperature of the upper ring increases, as

shown in figure. 6.8 (a), the ER of M1 drops while the ER of M2 rises. This indicates that the energy of the mode M1 is more localized into the bottom ring. In contrast, for the mode M2, the optical energy is more localized into the upper ring. While heating the bottom ring will give opposite distributions, as shown in figure. 6.8 (b), the ER of M1 raises and the ER of M2 declines. In this case, the energy is more allocated into the upper ring when the mode M1 is pumped, and into the bottom ring when the mode M2 is pumped. In conclusion, the energy distributions of the resonant modes are significantly influenced by the location of the heating source. Also, the energy concentration of M2 and M1 are proportional and inversely proportional to the temperature, respectively. In this way, we correlate the energy localization of the split modes to the measured ER changes, enabling us to utilize the measured thermally-induced ERs changes to quantify the energy distribution of the resonance modes.

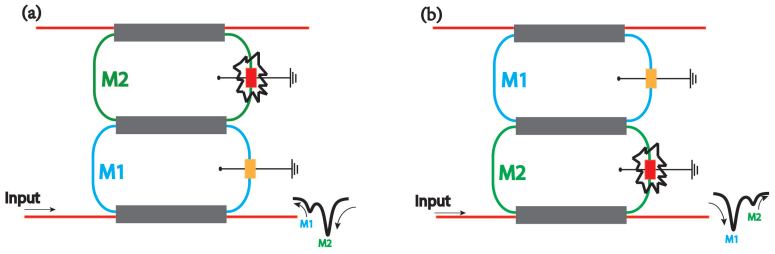

Figure 6.8: The optical energy distributions of M1 and M2 when two rings are heated, respectively. (a) When the upper ring is heated. (b) When the bottom ring is heated.

6.2.4.2 The comparison between M1 and M2 when the temperature is changing

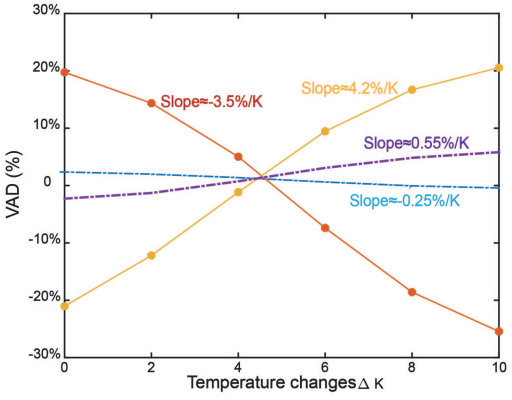

Figure 6.9: The simulated results for the variation of VAD when the temperature is changing. Yellow line: the upper ring is heated, $\kappa = 0.5$. Red line: the bottom ring is heated, $\kappa = 0.5$. Purple line: the upper ring is heated, $\kappa = 0.1$. blue line: the bottom ring is heated, $\kappa = 0.1$.

In this experiment, the variation of the normalized amplitude difference (VAD) between M1 and M2 is used to quantify the induced thermal perturbation. VAD is

defined as $VAD = ((T_{M1} - T_{M2})/T_{M1}) \times 100\%$, where T_{M1} and T_{M2} are the normalized amplitudes of the mode M1 and M2, respectively. When the upper ring or the bottom ring is heated, the VAD will vary with temperature. In figure. 6.9, Device A and Device B are evaluated, respectively. When Device A is tested, the significant difference between the attenuation coefficient α and coupling coefficient κ decreases ER, which limits the total range of amplitude changes. When the upper ring is heated (Blue line), the VAD is gradually decreasing from 2% to -1% as the temperature increases from 0k to 10k, the corresponding variation rate is $\sim -0.25\%/\mathrm{K}$. In contrast, the VAD exhibits opposite trend when the bottom ring is heated (Purple line), which is gradually increasing from -2% to 5%, the corresponding variation rate is $\sim 0.55\%/\mathrm{K}$. However, when the κ increases, enabling the coupled rings to approach critical coupling, the maximum ERs of both modes will increase. As shown by the yellow and red lines in figure. 6.9, the VAD is gradually changing between -25% to 20% as the temperature is increasing. The variation rates are $\sim -3.5\%/\mathrm{K}$ and $\sim 4.2\%/\mathrm{K}$ for the upper and bottom heating positions, respectively. The results show that under the same temperature changing range ΔK, the variation rate of VAD for Device B is four times higher than the Device A. In conclusion, the VAD variation rate is significantly relied on the maximum ER that the system can reach. Heating different positions gives opposite VAD variations, the variation is 0 when the transmissions of M1 and M2 are equal, which agrees with the theory.

6.2.4.3 Comparing with thermally-induced frequency-shift

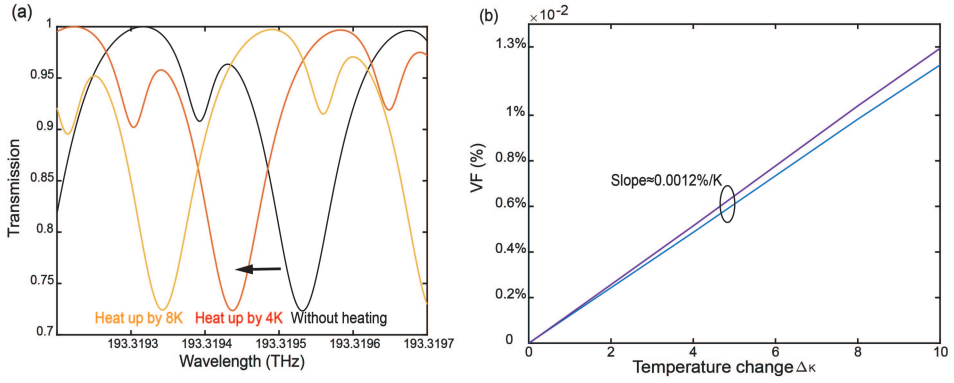

Figure 6.10: (a) The simulated frequency shift when two rings are heated at the same time. (b) The variation of the VF when ΔT increases from 0K to 10K, purple line: M1, blue line: M2.

As the coupled ring resonator is heated, the frequency of the resonant mode will shift due to the thermal-optical effect. However, this shift is small as the thermal-optical coefficient is small. In theory, the resonant frequency shift that is due to the thermal-optical effect can be expressed as [160]:

$$f_r - f_0 = \frac{N}{n_g} \cdot f_r \cdot \Delta T \tag{6.29}$$

where f_0 and f_r are the resonant frequencies before and after thermal perturbation, respectively. N is the thermal-optical coefficient and n_g is the group index. Figure. 6.10 (a) displays the resonant frequency shift when both rings are heated. Both split modes are blue-shifted when the temperature increases. The resonant frequencies of modes M1 and M2 are shifted by 72MHz and 90MHz, respectively when the temperature is increasing by 8K. To evaluate the temperature sensitivity of the thermally-induced-frequency-shift-based sensing, we define the variation of the resonant frequency as $VF = ((f_r - f_0)/f_0) \times 100\%$, where f_0 and f_r are the resonant frequencies before and after the temperature changes. As shown in figure. 6.10 (b), when the temperature is increased by the value from 0K to 10K, both resonant frequencies shift at a similar rate. The variation rate of the VF is around 0.0012%/K. Comparing the VAD and the VF, it is found that the variation rate of the optical-mode-localization-effect-based VAD is about 3 orders of magnitude greater than the variation rate of the frequency-shift-based VF, and this can be further enhanced if the critical coupling is reached. Traditionally, fibre ring resonators are rarely used as temperature sensor because thermal optical effects are immaterial when using large cavities [160], only on-chip micro-resonators are eligible for temperature sensing [161, 49]. With the mode localization enhancement, the sensitivity to temperature changes improves by 3 orders of magnitude, which makes fibre-coupled ring resonators a potential ultra-high sensitive temperature sensor.

6.2.5 Experimental results

6.2.5.1 The temperature response of TEC heater

Firstly, two TEC heaters (Thorlabs-TECF1S) are tested. The dimension of the TEC heater is shown in figure. 6.11 (a), the effective heating distance is assumed to be $10mm$. When it is connected to the power supply (TTI EL302), the temperature response is shown in figure. 6.11 (b). Due to the limit of the temperature measuring equipment, only the temperatures at I=0A, 0.1A, 0.2A and 0.4A will be used to test our devices.

6.2.5.2 Transmission responses when the devices are heated

Figure. 6.12 displays the measured transmission responses when the upper or bottom ring is heated. In the experiment, both devices are heated up by the value from 0K to 8.5K. For Device A, The ER of M1 decreases from 0.16 to 0.13 when the upper ring is

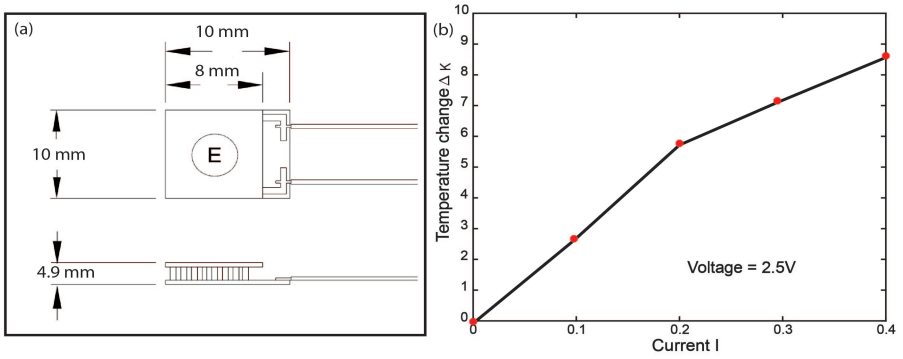

Figure 6.11: (a) The dimension of the TEC heater and (b)its temperature response

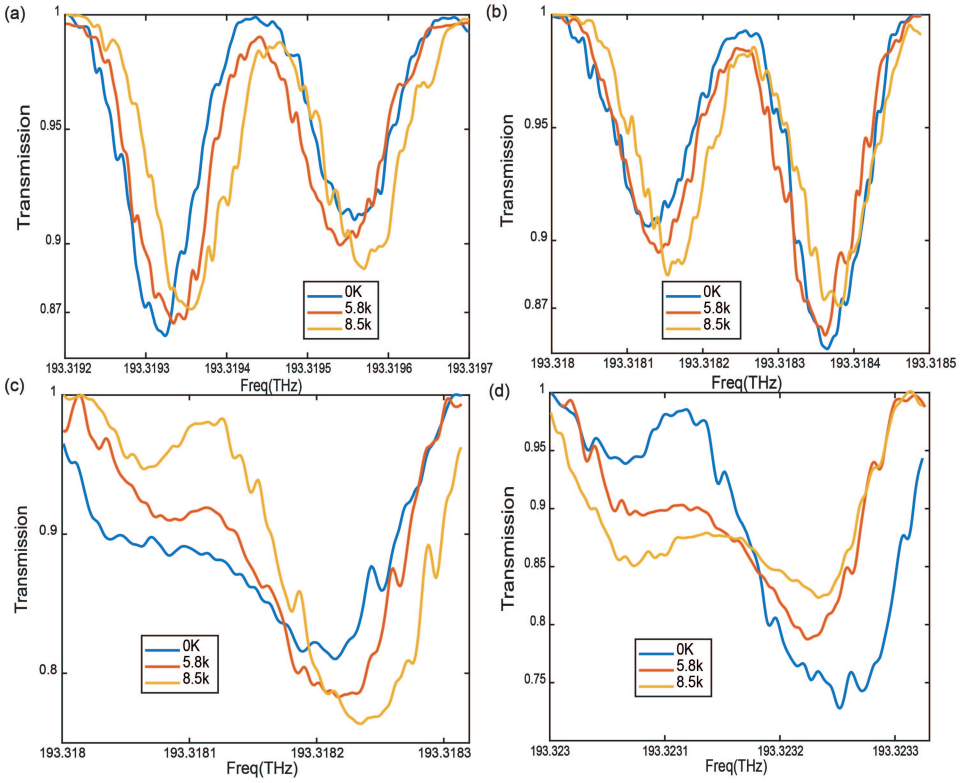

Figure 6.12: The transmission response of the device with (a) $\kappa = 0.1$ when the upper ring is heated, (b) $\kappa = 0.1$ when the bottom ring is heated, (c) $\kappa = 0.5$ when the upper ring is heated (d)$\kappa = 0.5$ when the bottom ring is heated. The inset is the temperature changes induced by TEC heaters.

heated and increases from 0.09 to 0.12 when the bottom ring is heated, respectively. In contrast, the ER of M2 increases from 0.09 to 0.12 when the upper ring is heated and decreases from 0.16 to 0.13 when the bottom ring is heated, respectively. The results are shown in figure. 6.12 (a) and (b). When Device B is tested, the coupling coefficient κ increases from 0.1 to 0.5. As shown in figure. 6.12 (c) and (d), the variations of M1 and M2 show the same trends as Device A, but as the temperature increases, the steps of the variations become larger. the ER of M1 decreases from 0.12 to 0.04 when the upper ring is heated and increases from 0.06 to 0.15 when the bottom ring is heated,

respectively. In contrast, the ER of M2 increases from 0.17 to 0.23 when the upper ring is heated and decreases from 0.27 to 0.16 when the bottom ring is heated, respectively. Overall, increasing the coupling coefficient κ from 0.1 to 0.5 enables the coupled rings to approach critical coupling, which improves the maximum ERs of both modes. The measured opposite ERs changes of two modes with temperature also show good agreement with the theoretical results shown in figure. 6.12 (c) and (d).

6.2.5.3 The variations of VAD and VF during temperature changes

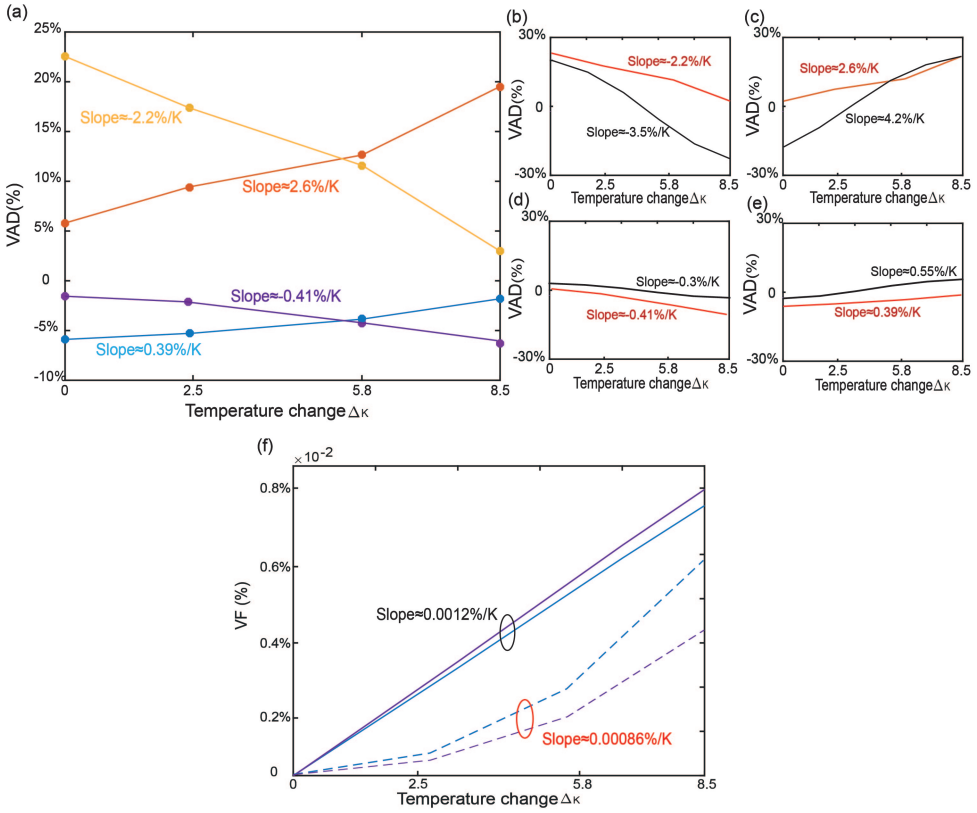

Figure 6.13: (a) The results for the variation of VAD with temperature changes. Yellow line: $\kappa = 0.5$, the upper ring is heated. Orange line: $\kappa = 0.5$, the bottom ring is heated. Purple line: $\kappa = 0.1$, the upper ring is heated. Blue line: $\kappa = 0.1$, the bottom ring is heated. (b)-(e) The comparisons between the simulated (Black line) and the measured (Red line) VADs: (b) $\kappa = 0.5$, the upper ring is heated. (c) $\kappa = 0.5$, the bottom ring is heated. (d) $\kappa = 0.1$, the upper ring is heated. (e) $\kappa = 0.1$, the bottom ring is heated. (f) The comparison between the simulated (solid line) and the measured (dashed line) VFs: purple line: M1, blue line M2.

To evaluate the device's sensitivity to the temperature changes, the variation of VAD is calculated based on the recorded transmissions. Figure. 6.13 (a) displays the VAD variation at 0K, 2.5K, 5.8K and 8.5K heated temperature. For Device B, the variation of the VAD ranges from 2.5% to 22.5%. The corresponding variation rate is $\sim -2.2\%/\mathrm{K}$ when the upper ring is heated and $\sim 2.6\%/\mathrm{K}$ when the bottom ring is heated. In contrast, for Device A, the variation range of VAD is limited within -6% to -2%. The

variation rates are $\sim -0.41\%/\mathrm{K}$ and $\sim 0.39\%/\mathrm{K}$ for the upper and bottom heating positions, respectively, which is around six times lower than Device A. The result is similar to our simulated one shown in figure. 6.9, where the variation rate of VAD improves by four times when increasing κ from 0.1 to 0.5. Figure. 6.13 (b)-(e) show the comparisons of VADs between the simulations and the measured results. It is found that the variation rates of the VADs of the measured results are slightly lower than the simulation results except when $\kappa = 0.1$ and the upper ring is heated, where the variation rate is $\sim -0.41\%/\mathrm{K}$ in the experiment and $\sim -0.3\%$ in the simulation. In addition, the maximum error occurs when $\kappa = 0.5$ and the bottom ring is heated, which is shown in figure. 6.13 (c), the variation rate in the experiment is $\sim 1.6\%$ lower than the simulation.

Figure. 6.13(f) shows the comparison between the simulated (solid line) VF and the experimental (dashed line) VF extracted from Figure. 6.12(c). The results show that the variation rate of VF when ΔT increases from 0K to 8.5K is $\sim 0.00086\%/\mathrm{K}$, which is at least three orders of magnitude lower than the variation rate of VAD. The experimental results exhibit good agreement with the simulation, proving that the optical mode localization effect has a good potential for ultra-sensitive sensing.

6.3 Discussion

Through theoretical and experimental studies, the phenomenon of optical mode localization due to the temperature perturbation in fibre-coupled ring resonators has been demonstrated. The device's sensitivity to temperature changes is improved by at least 3 orders of magnitude compared with frequency-shift-based sensing. In the experiment, the couplings of the fibre couplers are fixed so that it's hard to balance between the loss-induced attenuation factor α and coupling coefficient κ. If replacing them by tunable couplers, the sensitivity could be even higher.

In this experiment, fused fibre couplers from Thorlabs are used to form the fibre-coupled ring resonators. Fused fiber couplers are created by bringing two fibres into proximity and then heating and stretching them together to form a fused region. The coupling coefficient κ in this type of coupler is primarily determined by the degree of overlap between the evanescent fields of the fibres. By controlling the distance between the fibres and the duration and temperature of the fusion process, the coupling coefficient can be adjusted.

In consideration of cost saving, we directly purchased the fused fibre coupler from Thorlabs to form our device. Therefore, the coupling coefficient is fixed for a single fibre coupler. According to our research, a tunable fibre coupler is available in the market, but it is expensive. There are a few approaches commonly used to achieve

tunable fibre couplers, such as electro-optic tuning [162], thermal-optic tuning [163], mechanical tuning [162], etc.

Our previous study [164] shows that Both α and κ affect the sensitivity. While α is primarily determined by the loss induced from the fibres, couplers and fusion splices, which is hard to be controlled. From our previous study [164], when $\kappa = 0.1$, the highest sensitivity is achieved when $\alpha = 0.92$. While when κ increases to 0.64, the highest sensitivity is achieved when $\alpha = 0.84$. Therefore, increasing the coupling coefficient κ will reduce the requirement for the system loss. In this experiment, the system loss is high which leads to a low α. Therefore, the sensitivity is improved when we increase κ from 0.1 to 0.5.

In this experiment, the data for each measurement is obtained by averaging three replicate measurements. This approach effectively reduces the experimental errors caused by optical noise originated from the detector, laser power, external vibration, etc [165]. Due to the limited size of the fibre ring resonator, where a minimum circumference of 30cm has been reported [28], the FSR is within the range of hundreds megahertz. In this case, laser with good frequency resolution (narrow linewidth) is required. In this experiment, the measured minimum FSR of our device is 400 MHz, which is shown in figure. 6.7. The linewidth of the laser is 1MHz, which means 400 points can be measured for each period. In addition, random de-tuning will also happen because the laser has reached its maximum tunable linewidth. Therefore, laser with narrower linewidth can be used to improve the accuracy of the measurement.

The system can be potentially used for ultra-sensitive temperature fibre sensing. Also, any form of external perturbations can change the symmetry feature of the system, so that the quantitative measurement of this perturbation can be carried out. Not limited to temperature, other external perturbations including strain, pressure, etc., can be measured through optical mode localization effect. Therefore, the fibre-coupled ring resonators can be further explored for various sensing applications such as strain sensing[166], pressure sensing[167], gas sensing[168], etc. In addition, comparing with on-chip integrated photonic sensors, fibre-coupled ring resonators offer larger scale for sensing range. Also, due to the flexibility of optical fibres, the sensing objects can be more than just regular shapes, which enables sensing under various conditions.

6.4 Optical mode localization in on-chip coupled microring resonators

After the demonstration on fibre-coupled ring resonator, we also implement and study, for the first time, mode localization in coupled optical microresonators. The device consists of two coupled microrings and three microheaters, fabricated in a

silicon-on-insulator process. Optical mode localization is tuned by thermal perturbations from the microheaters. Optical energy localized to one microring gives rise to changes in the extinction ratios (ERs) of the antisymmetric (AS) and symmetric (S) resonances. It is demonstrated that the ER difference between the AS and S resonances can be tuned from -26.78 dB to 24.71 dB. Transmission variations of the AS and S resonances caused by mode localization have also been studied. The transmission variation is three orders of magnitude greater than the variation of resonant wavelength caused by thermally perturbating two microrings simultaneously. The demonstrated optical mode localization and the induced changes in ERs of resonances can provide a new way for optical information processing and ultrasensitive sensing. This work is done by my colleague Hailong Pi.

6.4.1 Simulation

6.4.1.1 Spectrum

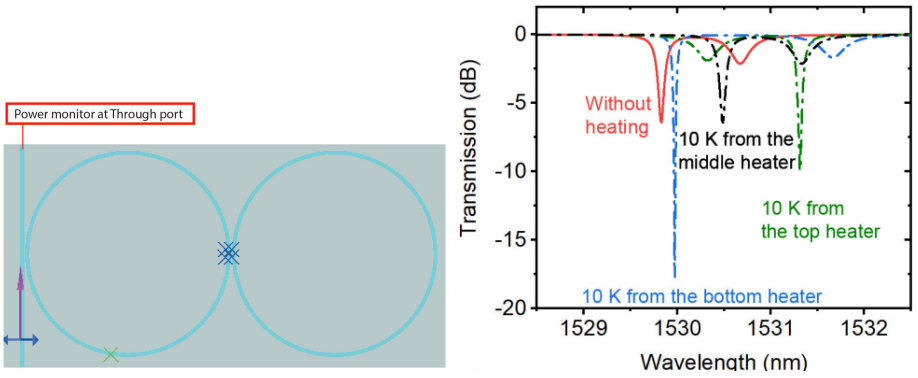

Figure 6.14: (a) The structure of a coupled-microring resonator, the width of the waveguide is 450 nm, the gap between the bus waveguide and microring, the gap between two microrings are 150 nm. (b)Simulated transmission spectra when different microrings are heated

Since on-chip microring resonator has smaller footprint, it is easier for simulation to run with short computational time. Here, the results are obtained using the varFDTD solver (Lumerical MODE solutions). The two microrings in the simulation are identical when they are not heated, which is shown in fig. 6.14 (a). Heating different microrings will give rise to the transmission spectra with distinct features, as shown in fig. 6.14 (b).The red line presents the transmission spectrum when no microring is heated. When ΔT of the top microring is increased by 10 K, the transmission spectrum is shown by the green dotted line. Compared to the ERs without heating, the ER of the S resonance experiences a significant change, increasing from 2.12 dB to 9.90 dB. The ER difference (ΔER) between AS and S resonances is decreased from 4.29 dB to -7.99 dB. Changing heating top microring to heating the bottom microring profoundly changes the ERs of resonances, as shown in the blue dotted line. Compared to the

transmission without heating, ΔER increases from 4.29 dB to 15.95 dB. Fig. 6.14 (b) also presents the transmission spectrum (black dotted line) when the middle microheater heats the two microrings together. The ERs of the AS and S resonances remain constant, and only the red shifts of resonant wavelengths occur.

6.4.1.2 Optical power distribution

Comparing the transmission spectra obtained using different microheaters, we can see that the top and bottom microheaters induce opposite changes in the ERs of the AS and S resonances. This is because the optical energy localizes to opposite microrings when the top or bottom microrings are heated. Figure. 6.15(a) and (b) show the changes in ΔER and optical energy ratio (R, defined as the ratio between the optical energy in the upper and bottom microrings) when different microrings are heated. In fig. 6.15(a), heating the upper ring can decrease ΔER and R decreases with decreasing ΔER at the AS resonance. This means more optical energy is in bottom ring than in the upper ring when pumping the device's AS resonance. On the contrary, at the S resonance, R increases with decreasing ΔER. At this time, Optical energy is localized to the upper ring.

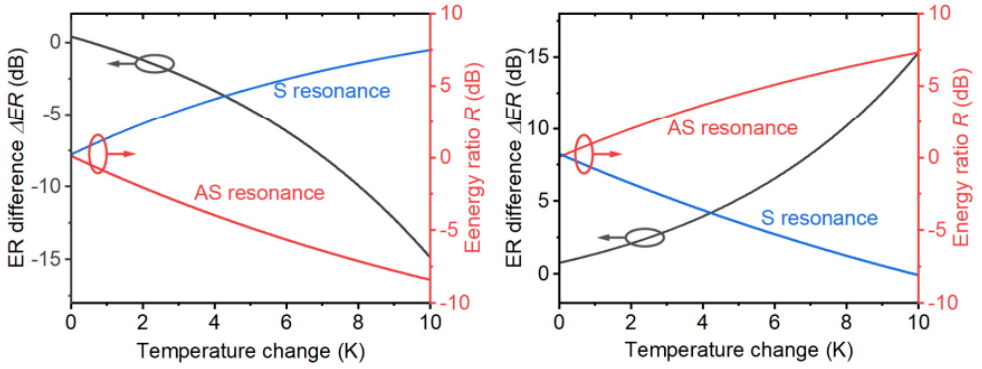

Figure 6.15: (a) Simulated ER difference (ΔER) between AS and S resonances and optical energy ratio (R) between the upper ring and the bottom ring when the temperature in the upper ring increases. (b) Simulated ΔER and R when the temperature in the bottom ring increases

Heating the bottom ring gives rise to opposite energy distributions. As shown in fig. 6.15(b), Heating the bottom ring increases ΔER. Energy is localized to the upper ring when pumping the device's AS resonance, while energy is localized to the bottom ring when pumping the S resonance. In conclusion, R at the AS resonance is positively correlated with ΔER, while R at the S resonance is negatively correlated with ΔER. This relation enables us to characterize optical mode localization using the ERs of AS and S resonances.

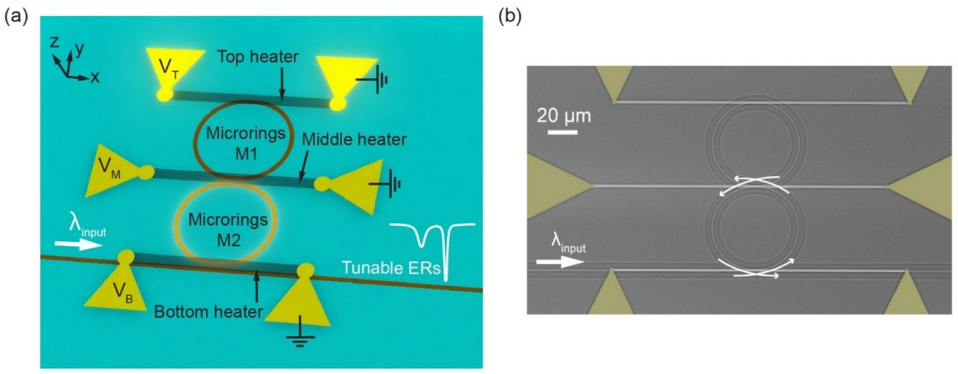

Figure 6.16: (a) Schematic of the device for studying optical mode localization. It consists of two coupled microrings and a bus waveguide. Three microheaters are used to heat different microrings. Optical energy will localize to one microring when a microheater is utilized. The figure shows that the top heater is used, and optical energy is localized to microring M2. The localized energy induces changes in the ERs of resonant modes. (b) SEM image of the fabricated device.

6.4.2 Device based on two coupled microrings

The device consists of two coupled microrings, a bus waveguide and three microheaters, as shown in fig. 6.16. All the waveguides are strip waveguides with a height of 220nm and a waveguide width of 400 nm. The bending radius of the microrings is 28.4 um, defined from the middle of the waveguides. The coupling gap between the two microrings is 250 nm, and the gap between the bus waveguide and microring M2 is also 250 nm. The coupling length for the two coupling areas is 2.2 µm. There is a SiO2 cladding layer with a thickness of 1 µm on top of the waveguides. Three TiN-based microheaters are utilized on top of the cladding layer. A pair of electrodes for supplying direct current (DC) voltages is connected to a pair of electrodes.

The device shown in fig. 6.16 (a) is fabricated on a 220 nm silicon-on-insulator platform using the CORNERSTONE rapid prototyping service. fig. 6.16 (b) shows the SEM image of the fabricated device. The yellow regions are the electrodes connected to the microheaters. The white arrows indicate the light coupling in and out of the bus waveguide, microrings M1 and microring M2.

6.4.3 Experimental setup and transmission spectrum

Fig. 6.17 (a) illustrates the schematic of the experimental setup used to measure the transmission spectra of the device. A DC power supply is used to apply voltages on specific electrodes to heat microrings. A current meter (CM) is used to record the DC current at each applied voltage. A probe laser sweeping in wavelength works with a

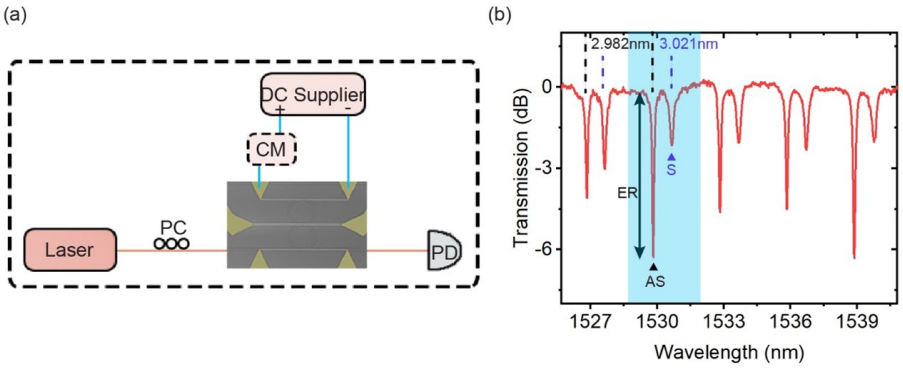

Figure 6.17: (a) Schematic of the experimental setup. It shows that a DC voltage is applied on the top microheater. (b) Transmission spectrum of the device when no microheater is used.

photodetector (PD) to record the transmission spectra. A polarization controller (PC) is used after the probe laser to excite the transverse electric mode in the device.

The transmission spectrum of the device without applying any DC voltage is shown in fig. 6.17 (b). The split notches in the transmission indicate the occurrence of the AS and S modes. The AS and S modes can be identified based on the free spectral range (FSR). The FSR for the left mode in the blue region is 2.98 nm, and the FSR for the right mode in the region is 3.02 nm. The smaller FSR indicates that the left mode in the region is the AS mode and the right mode in the region is the S mode. For a mode, the ratio between the on-resonance transmission and the off-resonance transmission is called extinction ratio (ER). The ERs of the AS and S resonances shown in fig. 6.17 (b) are different. The difference is because the fabricated microrings M1 and M2 are not identical. In the next sections, the refractive indices of the two microrings will be tuned by microheaters to study optical mode localization. The changes in the ERs of the AS and S resonances in the blue region, shown in fig. 6.17 (b), will be investigated.

6.4.4 Experimental results

The fabricated device shown in fig. 6.16 (a) is measured to explore the mode localization tuned by different heating conditions. At first, the middle heater is used to heat the two microrings simultaneously. Fig. 6.18 shows the transmission spectra of the device when different DC power is used. Both the AS and S resonant wavelengths are red-shifted as the applied DC power increases. According to the simulated results in Fig. 6.14 (b), heating both microrings will cause the same shifts of the resonant wavelengths. Fig. 6.18 (b) summarizes the resonance shift of AS and S modes. Compared to the S mode, the AS mode experiences larger resonance shifts when the DC power increases. This is because the heating increases the refractive indices of the waveguides in the coupling area and decreases the coupling coefficient.

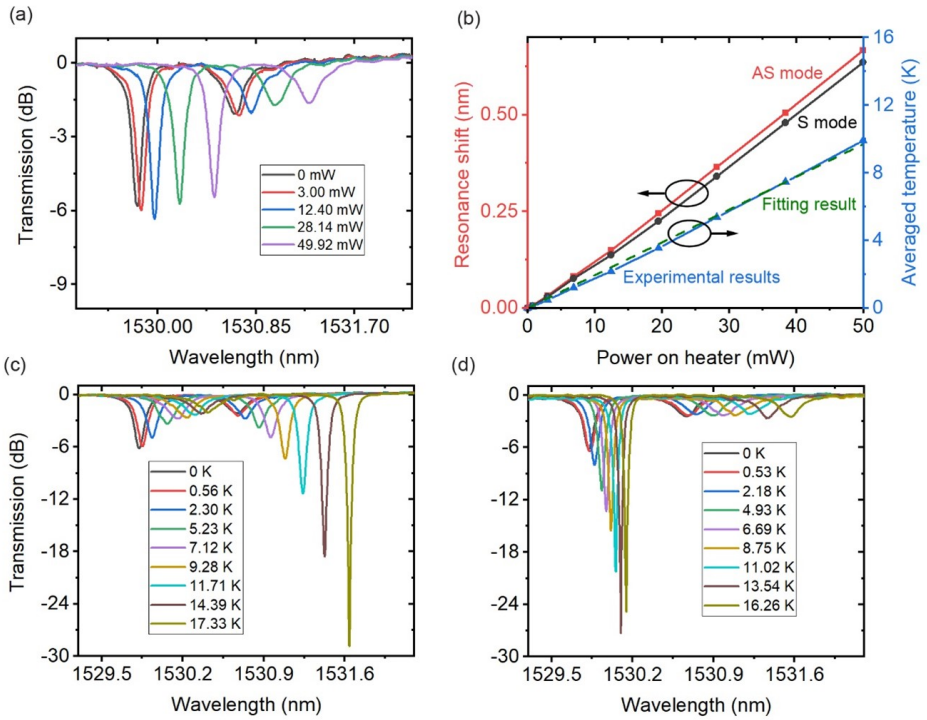

Figure 6.18: (a) Transmission spectra when the DC power on the middle microheater increases. (b) The resonance shifts of the AS and S modes when the DC power on the middle microheater increases. The relationship between the averaged temperature change ΔT and the applied DC power is derived. The blue line shows the calculated relationship from the experimental results, and the green dotted line shows the fitting results. (c) Transmission spectra when the top microheater heats microing M1. The temperatures in the inset are the average temperature changes ΔT calculated based on applied DC power. (d) Transmission spectra when the top microheater heats microring M1. The insert shows the average temperature change ΔT.

Following the measurement with the middle microheater, the top and bottom microheaters were utilized. Fig. 6.18 (c) and (d) show the transmission spectra of the device when the top and bottom heaters are used, respectively. The temperatures in the inset are the average temperature changes ΔT in microring M1 (Fig. 6.18 (c)) and in microring M2 (Fig. 6.18 (d)). When the microring M1 is heated, the ER of the S resonance experiences significant increases and the ER of the AS resonance decreases. On the contrary, when the microring M2 is heated, the ER of the AS resonance experiences significant increases and the ER of the S resonance decreases.

The opposite changes in the ERs of the AS and S resonances shown in fig. 6.18(c) and (d) result from mode localization. The mode localization is related to the ER difference ΔER between the AS and S resonances. The microheater increases the average temperature ΔT of the microring from 0K to 18K. It can be observed that the ER difference decreases as the temperature increases when the top heater is used. This indicates more optical energy is stored in microring M2 at the AS resonance and more energy is in microring M1 at the S resonance. The minimum ER difference of -26.78 dB is achieved when the temperature change ΔT is 17.33 K. Unlike heating microring M1,

heating microring M2 increases the ER difference. This means more optical energy is stored in microring M1 at the AS resonance and more energy is in microring M2 at the S resonance. The maximum difference of 24.71 dB is achieved when the temperature change is 13.54 K. Unlike the large variation caused by the top and bottom heaters, the variation of ERs caused by the middle heater is small. The ER difference is 3.24 ± 1.21 dB.

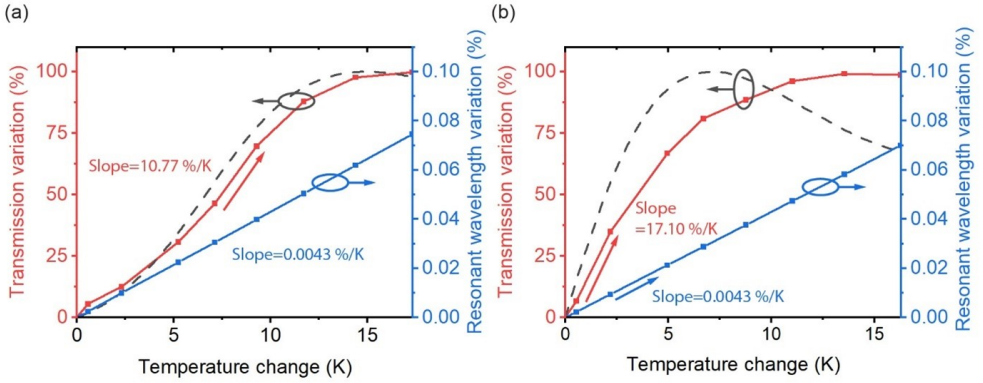

Figure 6.19: Comparison between the transmission and resonant wavelength vibrations. (a) The top heater is used. (b) The bottom heater is used.

Fig. 6.19(a) compares the transmission variation of the S resonance when the top heater is used and the resonant wavelength variation when the middle heater is used. The transmission variation gradually increases when the temperature increases in microring M1. The slope within the temperature range from 7.12 K to 9.28 K is 10.77%/K. The slope of the resonant wavelength variation is 0.0043%/K. Fig. 6.19 (b) shows the comparison between the transmission variation of the AS resonance when the bottom heater is used and the variation of the resonant wavelength when the middle heater is used. The transmission variation gradually increases and reaches the maximum at the temperature change of 13.54 K. The variation decreases as the temperature change ΔT increases further. The slope in the temperature range from 0.53 K to 2.18 K is 17.10%/K. The slope of the resonant wavelength variation is also 0.0043%/K. The dotted line is the simulated transmission variation. It can be seen that the temperature at which the maximum transmission variation occurs is 7.2 K. The mismatch between the simulated and experimental results is because the heating from the bottom heater changes the coupling coefficient between the bus waveguide and microing M2. Despite the mismatch, the experimental results exhibit three orders of magnitude improvement in sensitivity compared to the resonance wavelength shift.

6.4.5 Discussion

The mode localization has been experimentally investigated and theoretically studied in coupled optical microring resonators. The perturbation inducing the optical energy

localization is introduced by microheaters. Heating the microring M1 will localize the optical energy to microring M2 at the AS resonance and localize the optical energy to microring M1 at the S resonance. The ER of the S resonance experiences a significant increase. On the contrary, heating the microring M2 will localize optical energy to the microring M1 at the AS resonance and localize the optical energy to microring M2 at the S resonance. The ER of the AS resonance experiences a significant increase. These results show great agreement with our work on fibre-based system.

The ER difference between the AS and S resonances can be tuned from -26.78 dB to 24.71 dB by heating different microrings. Compared to the variation of resonant wavelength induced by heating two microrings simultaneously, the transmission variations of AS or S resonances are improved by three orders of magnitude.

6.5 Conclusion

In summary, we study the the optical mode localization in both on-chip- and fibre-coupled ring resonators. Through the simulation of the on-chip coupled ring resonators, we prove the energy distributions of the resonant modes are significantly influenced by the location of the heating source, which is originate from the optical mode localization effect. Then, we experimentally demonstrate the optical mode localization in fibre- and silicon-coupled ring resonators and their feasibility for high-sensitive sensing. For fibre-based system, two fibre-coupled ring resonators with different coupling coefficients (Device A and Device B) are fabricated by fusion-spliced fibre couplers, the thermal perturbations are induced by two TEC heaters covered on the upper and the bottom ring resonators, respectively. The VAD variation rate of $\sim$2.3%/K is achieved when the coupling coefficient is 0.5, which is three orders of magnitude greater than the variation rate of the frequency-shift-based VF. The value can be further enhanced if the system reaches critical coupling. For silicon-based system, The ER difference between the AS and S resonances can be tuned from -26.78 dB to 24.71 dB by heating different microrings, which shows three orders of magnitude improvement compared to the variation of resonant wavelength shift induced by heating two microrings simultaneously. These results shows that optical mode localization-based sensing increases the sensitivity of a cavity to the changes in refractive index, resulting in a larger shift in the amplitude of a resonant mode for a given change in refractive index, which provide a new way for ultra-sensitive fibre temperature sensing.

Chapter 7

Conclusions

7.1 Summary

In summary, this thesis proposes three novel PICs for nonlinear optics and sensing applications, including on-chip unsuspended silicon waveguide for enhanced stimulated Brillouin scattering, on-chip OFDR system and optical mode localization system.

Firstly, we propose a novel Si-AlN-Sapphire platform to achieve a robust Brillouin scattering interaction, all while avoiding the need to suspend the silicon core waveguide. This platform offers improved mechanical and thermal stability, and simplifies fabrication without compromising crystal quality. To address the decrease in the total gain coefficient in the unsuspended structure resulting from reduced moving boundary contribution, we employ a genetic algorithm to optimize the waveguide structure and total gain coefficient. To ensure feasibility in fabrication, the optimization process is constrained by limiting the maximum etching step to two for the final structure. The design can realize a total gain value of $2462 W^{-1} m^{-1}$, which is 8 times larger than the recently reported result in unsuspended silicon waveguide.

Secondly, a novel on-chip OFDR system is proposed. The device is based on a standard $220nm$- SOI platform, the footprint is under $100\mu m^2$. The experiment results shows that the system achieves a spatial resolution of $7.59\mu m$, which is very close to the theoretical results. The components in the system are designed by traditional methods and photonic inverse design approach, respectively. The measured results show that both methods achieve great performances, but the footprint of the inverse-designed-components is at least 20 times smaller than the devices designed by traditional methods, which is very essential for ultra-compact photonic circuit.

Following the demand for further reducing the footprint and detection complexity of our on-chip OFDR system, a novel monolithically integrated polarization rotator and

splitter with designed power ratio is designed by using a modified direct-binary-search (DBS) algorithm. The device achieves both polarization rotation and power splitting with a maximum insertion loss of 1 dB. The crosstalk between TE_{00} and TM_{00} modes is less than -9.5 dB. The device can change the detecting scheme of our on-chip OFDR system, the detection complexity can be further reduced.

Lastly, optical mode localization effect is proposed. It is proved that optical mode localization-based sensing increases the sensitivity of a cavity to the changes in refractive index, resulting in a larger shift in the amplitude of a resonant mode for a given change in refractive index, which provide a new way for ultra-sensitive temperature sensing. This effect is utilized into fibre- and on-chip- coupled-ring resonators to produce ultra-high sensitive sensor. The experiment results exhibits at least 3 orders of magnitude higher sensitivity than the traditional resonant-shift based sensors.

7.2 Future work

Firstly, the theoretical work from Chapter. 3 can be experimentally demonstrated. To obtain the Si-AlN-Sapphire wafer, one can either deposit a silicon layer on the top of AlN or direct wafer bond a device silicon layer with a commercial AlN-Sapphire wafer. The deposition method benefits from higher efficiency and easier process, while direct wafer bonding has the advantages of better surface roughness and crystal quality, which will greatly affect the performance of SBS device. Therefore direct wafer bonding is preferred for this specific application.

Recently, a hydrophilic wafer bonding process is reported to further enhance the bonding quality between silicon and AlN layers [131]. The core procedure of the process is to active the AlN layer with a plasma etching. This specific plasma, including O_2, Ar, SF_6, can change the chemical and topography of the AlN layer. After the plasma activation, AlN layer will have enhanced hydrophilicity, reduced surface roughness and low nanotopography. All of these changes lead to a strong and solid bonding between silicon and AlN layers [131]. Via this method, a strong bonding can be formed between the silicon and AlN layers, and both silicon and AlN can retain the crystalline quality of the pre-bonded wafers.

In fig. 3.10, it can be seen that the SBS gain is significantly sensitive to the offset of the trench position. Any small variation of the offset will lead to a reduction of the SBS gain. To tackle this problem, we can introduce the concept of Computational Lithography [169, 170]. Computational lithography focuses on using computational algorithms and simulations to enhance the lithography process [170]. Recently, researchers have successfully used computational lithography to resolve fabrication errors due to optical proximity effects [171]. In order to decrease the sensitivity of

fabrication error to the SBS gain in our system, the offset of the trench width, depth and position can be used as the feedback and fed to the genetic algorithm. By adding constraints to wider range of trenching width, depth and position, the optimized SBS gain should be stable within a wider parameter range.

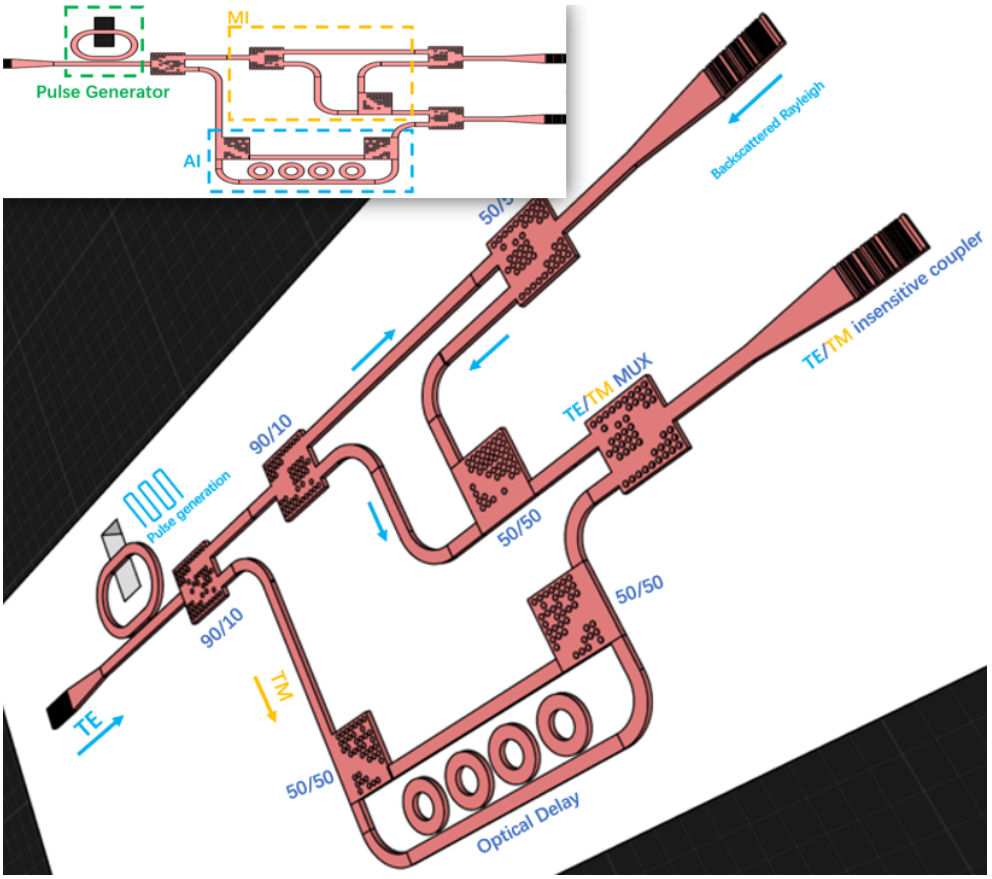

Figure 7.1: The schematic of the optimized on-chip OFDR system. The continuous light signal with fundamental TE mode is passing through an on-chip pulse generator [172]. Then a set of pulses is generated and enters the monolithically integrated polarization rotator and splitter with designed power ratio, where 10 % of the input signal is converted to TM mode and used as AI signal, the other 90 % is remained as TE mode and used as MI signal. For MI, the signal will be coupled out to the FUT and the back-scattered signal will be interfered with the signal in the reference arm. For AI, the TM mode signal will experience an optical delay to maximize the spatial resolution, and then interferes with the signal in the reference arm. Finally, the TE and TM beat signals are collected by a TE/TM multiplexer and coupled out by a TE/TM insensitive coupler.

Secondly, the on-chip OFDR system can be further improved with more compact in size and simpler probing scheme with the help of photonic inverse design method. Currently, the signals from MI and AI are collected by two separate GCs, where calibration is needed to ensure two signals are extracted in phase. Also, extra GCs induce more complexities during the coupling between fibre and GC. To tackle these problems, photonic inverse design algorithms can be used to design multi-functional devices, which will fulfil the same functionalities as the previous devices but with more compactness and integration.

As shown in fig. 7.1, several updates are made to achieve more compact and efficient on-chip OFDR system. Firstly, an on-chip pulse generator [172] is placed before the interferometers, this change replaces the original out-of-chip- function generator and Electro-optic modulator (EOM), which effectively reduces the construction cost. Secondly, a monolithically integrated polarization rotator and splitter with designed power ratio is used to separate AI and MI signal by converting 10 % of the input signal to TM-mode-AI signal. This modification changes the original probing scheme as we utilize the orthogonality between TE and TM mode; interference will not occur. Therefore, the signal from AI and MI can be collected at the same time using a TE/TM insensitive grating coupler without destroying the information. Thirdly, a TE/TM multiplexer and a TE/TM insensitive grating coupler are required due to the appearance of TE and TM modes. Fourthly, for optical delay line, the original straight waveguide is replaced by cascaded optical ring resonators [173], which will significantly reduce the footprint of the device. Lastly, the on-chip FUT is replaced by optical fibre in real scenario. Signal from MI will be coupled out to the FUT and the back-scattered signal will be coupled in and interfered with the signal in the reference arm to measure the temperature or sprain distributively in actural conditions.

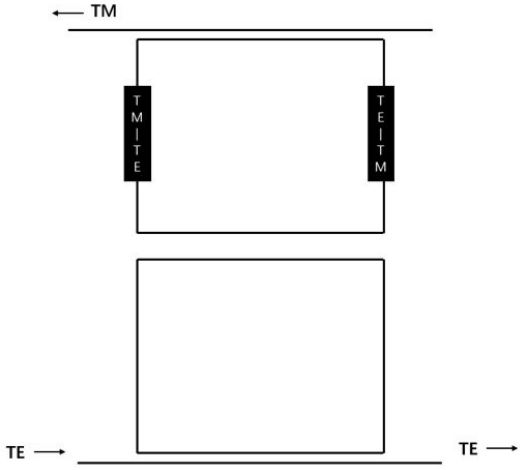

Figure 7.2: The schematic of the tunable TE-TM coverter.

Thirdly, it has been approved in chapter five that the power amplitude of the split resonant modes in the coupled ring resonators can be thermally tuned and shows ultra-high sensitivity. If combining the coupled ring resonators and the optimized polarization rotator shown in chapter five, it is possible to realize an ultra-sensitive and compact tunable TE-TM converter. The schematic is shown in fig. 7.2. The TE mode only exists in the bottom ring resonator, the polarization conversion occurs in the upper ring resonator. With such system, TE and TM modes can be arbitrarily converted by using the heater placed on the ring resonators. The TE and TM modes will be coupled out from the through port (bottom port) and drop port (upper port), respectively.

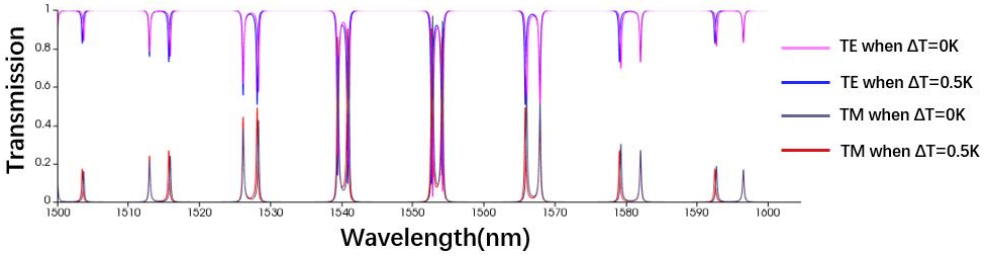

Figure 7.3: The simulated transmission spectrum of the tunable TE-TM converter.

Fig. 7.3 shows the simulated transmission spectrum of the tunable TE-TM converter. Taking a pair of split resonance modes within the wavelength of 1520 nm to 1530 nm as an example, the amplitude of TE and TM modes show corresponding changes when the temperature is changing. When the temperature change ΔT varies from 0K to 0.5K, the amplitude of TE mode decreases while the amplitude of TM mode increases. The same trend can also be observed from other wavelength ranges. Therefore, it is possible to combine coupled ring resonators and optimized polarization rotator to realize a novel tunable TE-TM converter, which can be applied to a wide range of applications such as optical communication, sensing, etc.

Chapter 8

List of publications

Feng, Y., Wang, S., Mashanovich, G., & Yan, J. (2021). Theory analysis of the optical mode localized sensing based on coupled ring resonators. Optics Express, 29(20), 32505-32522.

Wang, S., Li, P. and Yan, J., 2023. Monolithically integrated polarization rotator and splitter with designed power ratio. Optics Express, 31(9), pp.14128-14139.

Li, P.,Wang S, Mashanovich, G.Z., Ou, J.Y. and Yan, J., 2023. Enhanced stimulated Brillouin scattering in the unsuspended silicon waveguide assisted with genetic algorithms. Optics Express, 31(10), pp.16162-16177. (Co-first author)

Wang S, Pi, H., Feng, Y. and Yan, J., 2023. Optical mode localization sensing based on fiber-coupled ring resonators. Optics Express, 31(13), pp.21834-21844.

Pi H, Wang S, Feng Y, Thomson DJ, Yan J. "Optical mode localization in on-chip coupled microring resonators", Apl Photonics. (Peer-reviewing)

Han G, Guo Z, Wang S, Du H, Yu Y, Marco J, Greenwood D, Yan J. "Integrated optical frequency domain reflectometry with ultimate spatial resolution". Opt Express. (Peer-reviewing)

Bibliography

[1] Po-Han Fu, Yi-Chou Tu, and Ding-Wei Huang. "Broadband optical waveguide couplers with arbitrary coupling ratios designed using a genetic algorithm". In: *Optics express* 24.26 (2016), pp. 30547–30561.

[2] Luluzi Lu et al. "Inverse-designed single-step-etched colorless 3 dB couplers based on RIE-lag-insensitive PhC-like subwavelength structures". In: *Optics letters* 41.21 (2016), pp. 5051–5054.

[3] Guozhen Liang et al. "Robust, efficient, micrometre-scale phase modulators at visible wavelengths". In: *Nature Photonics* 15.12 (2021), pp. 908–913.

[4] Vien Van. *Optical microring resonators: theory, techniques, and applications*. CRC Press, 2016.

[5] Tuo Shi et al. "Silicon photonics platform for 400G data center applications". In: *Optical Fiber Communication Conference*. Optica Publishing Group. 2018, M3F–4.

[6] Kiyoshi Asakawa, Yoshimasa Sugimoto, and Shigeru Nakamura. "Silicon photonics for telecom and data-com applications". In: *Opto-Electronic Advances* 3.10 (2020), pp. 200011–1.

[7] Patrick Steglich et al. "Optical biosensors based on silicon-on-insulator ring resonators: A review". In: *Molecules* 24.3 (2019), p. 519.

[8] Tayebeh Sahraeibelverdi et al. "Polymer ring resonator with a partially tapered waveguide for biomedical sensing: Computational study". In: *Sensors* 21.15 (2021), p. 5017.

[9] Muzammil Iqbal et al. "Silicon photonic micro-ring resonators for drug screening and kinetic analysis". In: *Label-Free Biosensor Methods in Drug Discovery* (2015), pp. 133–153.

[10] Arthur H Hartog. *An introduction to distributed optical fibre sensors*. CRC press, 2017.

[11] Jia Song et al. "Long-range high spatial resolution distributed temperature and strain sensing based on optical frequency-domain reflectometry". In: *IEEE Photonics Journal* 6.3 (2014), pp. 1–8.

[12] Robert W Boyd. *Nonlinear optics*. Academic press, 2020.

[13] RY Chiao, Ch H Townes, and BP Stoicheff. “Stimulated Brillouin scattering and coherent generation of intense hypersonic waves”. In: *Physical Review Letters* 12.21 (1964), p. 592.

[14] Jiang Li, Hansuek Lee, and Kerry J Vahala. “Low-noise Brillouin laser on a chip at 1064 nm”. In: *Optics letters* 39.2 (2014), pp. 287–290.

[15] Amol Choudhary et al. “On-chip Brillouin filtering of RF and optical signals”. In: *IEEE journal of selected topics in quantum electronics* 24.6 (2018), pp. 1–11.

[16] Amol Choudhary et al. “High-resolution, on-chip RF photonic signal processor using Brillouin gain shaping and RF interference”. In: *Scientific Reports* 7.1 (2017), p. 5932.

[17] Ravi Pant et al. “On-chip stimulated Brillouin scattering”. In: *Optics express* 19.9 (2011), pp. 8285–8290.

[18] Raphaël Van Laer et al. “Interaction between light and highly confined hypersound in a silicon photonic nanowire”. In: *Nature Photonics* 9.3 (2015), pp. 199–203.

[19] Flavien Gyger et al. “Observation of stimulated Brillouin scattering in silicon nitride integrated waveguides”. In: *Physical review letters* 124.1 (2020), p. 013902.

[20] Warren Jin et al. “Stimulated Brillouin scattering in AlGaAs on insulator waveguides”. In: *CLEO: Science and Innovations*. Optica Publishing Group. 2020, SM4L–7.

[21] Jingcui Song et al. “Stimulated Brillouin scattering in low-loss Ge 25 Sb 10 S 65 chalcogenide waveguides”. In: *Journal of Lightwave Technology* 39.15 (2021), pp. 5048–5053.

[22] Wenjun Qiu et al. “Stimulated Brillouin scattering in nanoscale silicon step-index waveguides: a general framework of selection rules and calculating SBS gain”. In: *Optics express* 21.25 (2013), pp. 31402–31419.

[23] Mikołaj K Schmidt et al. “Suspended mid-infrared waveguides for Stimulated Brillouin Scattering”. In: *Optics express* 27.4 (2019), pp. 4976–4989.

[24] Hualong Wu et al. “Recent advances in fabricating wurtzite AlN film on (0001)-plane sapphire substrate”. In: *Crystals* 12.1 (2021), p. 38.

[25] Luis A Bru, Daniel Pastor, and Pascual Muñoz. “Integrated optical frequency domain reflectometry device for characterization of complex integrated devices”. In: *Optics Express* 26.23 (2018), pp. 30000–30008.

[26] Pradyumna Thiruvenkatanathan et al. “Enhancing parametric sensitivity in electrically coupled MEMS resonators”. In: *Journal of Microelectromechanical Systems* 18.5 (2009), pp. 1077–1086.

[27] P Thiruvenkatanathan et al. “Ultrasensitive mode-localized mass sensor with electrically tunable parametric sensitivity”. In: *Applied Physics Letters* 96.8 (2010), p. 081913.

[28] John E Heebner et al. “Optical transmission characteristics of fiber ring resonators”. In: *IEEE journal of quantum electronics* 40.6 (2004), pp. 726–730.

[29] Kostadin Djordjev et al. “High-Q vertically coupled InP microdisk resonators”. In: *IEEE Photonics Technology Letters* 14.3 (2002), pp. 331–333.

[30] D Rafizadeh et al. “Waveguide-coupled AlGaAs/GaAs microcavity ring and disk resonators with high finesse and 21.6-nm free spectral range”. In: *Optics letters* 22.16 (1997), pp. 1244–1246.

[31] LD Hutcheson, PR Haugen, and A Husain. “Gigabit per second optical chip-to-chip interconnects”. In: *Fiber Optic Sources and Detectors*. Vol. 587. SPIE. 1986, pp. 116–125.

[32] Yuan Meng et al. “Optical meta-waveguides for integrated photonics and beyond”. In: *Light: Science & Applications* 10.1 (2021), pp. 1–44.

[33] Frank J Effenberger and Abhay M Joshi. “Ultrafast, dual-depletion region, InGaAs/InP pin detector”. In: *Journal of lightwave technology* 14.8 (1996), pp. 1859–1864.

[34] V Berger. “Nonlinear photonic crystals”. In: *Physical review letters* 81.19 (1998), p. 4136.

[35] Peter T Rakich et al. “Giant enhancement of stimulated Brillouin scattering in the subwavelength limit”. In: *Physical Review X* 2.1 (2012), p. 011008.

[36] Stefan Diez et al. “Four-wave mixing in semiconductor optical amplifiers for frequency conversion and fast optical switching”. In: *IEEE Journal of selected topics in Quantum Electronics* 3.5 (1997), pp. 1131–1145.

[37] Laura Mercadé et al. “Vertical engineering for large Brillouin gain in unreleased silicon-based waveguides”. In: *Physical Review Applied* 15.3 (2021), p. 034021.

[38] Blair Morrison et al. “Tunable microwave photonic notch filter using on-chip stimulated Brillouin scattering”. In: *Optics Communications* 313 (2014), pp. 85–89.

[39] J Pastrňák and L Roskovcová. “Refraction index measurements on AlN single crystals”. In: *physica status solidi (b)* 14.1 (1966), K5–K8.

[40] Jani Kaaos, Glenn Ross, and Mervi Paulasto-Krockel. “Aluminum Nitride to Silicon Direct Bonding for an Alternative Silicon-On-Insulator Platform”. In: *ACS applied materials & interfaces* 13.32 (2021), pp. 38857–38865.

[41] Jesper Håkansson and Dries Van Thourhout. “Generating novel waveguides for stimulated Brillouin scattering with genetic algorithms”. In: *APL Photonics* 4.1 (2019), p. 010803.

[42] Christian Wolff et al. “Stimulated Brillouin scattering in integrated photonic waveguides: Forces, scattering mechanisms, and coupled-mode analysis”. In: *Physical Review A* 92.1 (2015), p. 013836.

[43] C Wolff et al. “Germanium as a material for stimulated Brillouin scattering in the mid-infrared”. In: *Optics express* 22.25 (2014), pp. 30735–30747.

[44] Joshua EY Lee, Jize Yan, and Ashwin A Seshia. “Study of lateral mode SOI-MEMS resonators for reduced anchor loss”. In: *Journal of Micromechanics and Microengineering* 21.4 (2011), p. 045010.

[45] BG Helme and PJ King. “The phonon viscosity tensor of Si, Ge, GaAs, and InSb”. In: *physica status solidi (a)* 45.1 (1978), K33–K37.

[46] A Frangi et al. “Validation of PML-based models for the evaluation of anchor dissipation in MEMS resonators”. In: *European Journal of Mechanics-A/Solids* 37 (2013), pp. 256–265.

[47] Xin Meng et al. “Atomic layer deposition of silicon nitride thin films: a review of recent progress, challenges, and outlooks”. In: *Materials* 9.12 (2016), p. 1007.

[48] Peng Li et al. “Tailorable stimulated Brillouin scattering in a partially suspended aluminium nitride waveguide in the visible range”. In: *Optics Express* 30.15 (2022), pp. 27092–27108.

[49] Gun-Duk Kim et al. “Silicon photonic temperature sensor employing a ring resonator manufactured using a standard CMOS process”. In: *Optics express* 18.21 (2010), pp. 22215–22221.

[50] Lei Wan et al. “On-chip, high-sensitivity temperature sensors based on dye-doped solid-state polymer microring lasers”. In: *Applied Physics Letters* 111.6 (2017).

[51] Xin Li et al. “Accurate on-chip temperature sensing for multicore processors using embedded thermal sensors”. In: *IEEE Transactions on Very Large Scale Integration (VLSI) Systems* 28.11 (2020), pp. 2328–2341.

[52] Ping Lu et al. “Distributed optical fiber sensing: Review and perspective”. In: *Applied Physics Reviews* 6.4 (2019), p. 041302.

[53] Robert F Klein Breteler et al. “Photonic integrated Brillouin optical time domain reflection readout unit”. In: *Optical Engineering* 50.7 (2011), pp. 071111–071111.

[54] Jiaqiang Huang et al. “Distributed fiber optic sensing to assess in-live temperature imaging inside batteries: rayleigh and FBGs”. In: *Journal of The Electrochemical Society* 168.6 (2021), p. 060520.

[55] Daniele Inaudi and Branko Glisic. “Long-range pipeline monitoring by distributed fiber optic sensing”. In: (2010).

[56] Judit Gómez, Joan R Casas, and Sergi Villalba. "Structural Health Monitoring with Distributed Optical Fiber Sensors of tunnel lining affected by nearby construction activity". In: *Automation in Construction* 117 (2020), p. 103261.

[57] Dan Zhao et al. "High resolution optical frequency domain reflectometry for analyzing intra-chip reflections". In: *IEEE Photonics Technology Letters* 29.16 (2017), pp. 1379–1382.

[58] Mudabbir Badar et al. "Integrated auxiliary interferometer for self-correction of nonlinear tuning in optical frequency domain reflectometry". In: *Journal of Lightwave Technology* 38.21 (2020), pp. 6097–6103.

[59] Ting Feng et al. "Distributed transverse-force sensing along a single-mode fiber using polarization-analyzing OFDR". In: *Optics Express* 28.21 (2020), pp. 31253–31271.

[60] Rodrigo Mendes Gerosa et al. "Distributed pressure sensing using an embedded-core capillary fiber and optical frequency domain reflectometry". In: *IEEE Sensors Journal* 21.1 (2020), pp. 360–365.

[61] Frederic Monet et al. "High-resolution optical fiber shape sensing of continuum robots: A comparative study". In: *2020 IEEE international conference on robotics and automation (ICRA)*. IEEE. 2020, pp. 8877–8883.

[62] Matthew Spletzer et al. "Highly sensitive mass detection and identification using vibration localization in coupled microcantilever arrays". In: *Applied Physics Letters* 92.11 (2008), p. 114102.

[63] Pradyumna Thiruvenkatanathan et al. "Limits to mode-localized sensing using micro-and nanomechanical resonator arrays". In: *Journal of Applied Physics* 109.10 (2011), p. 104903.

[64] Pradyumna Thiruvenkatanathan, Jize Yan, and A Ashwin Seshia. "Ultrasensitive mode-localized micromechanical electrometer". In: *2010 IEEE international frequency control symposium*. IEEE. 2010, pp. 91–96.

[65] Pradyumna Thiruvenkatanathan, Jize Yan, and A Ashwin Seshia. "Common mode rejection in electrically coupled MEMS resonators utilizing mode localization for sensor applications". In: *2009 IEEE international frequency control symposium joint with the 22nd European frequency and time forum*. IEEE. 2009, pp. 358–363.

[66] Pradyumna Thiruvenkatanathan, Jize Yan, and Ashwin A Seshia. "Differential amplification of structural perturbations in weakly coupled MEMS resonators". In: *IEEE transactions on ultrasonics, ferroelectrics, and frequency control* 57.3 (2010), pp. 690–697.

[67] Ruize Xu, Shengli Zhou, and Wen J Li. "MEMS accelerometer based nonspecific-user hand gesture recognition". In: *IEEE sensors journal* 12.5 (2011), pp. 1166–1173.

[68] Honglong Chang et al. “An integrated MEMS gyroscope array with higher accuracy output”. In: *Sensors* 8.4 (2008), pp. 2886–2899.

[69] Don C Abeysinghe et al. “A novel MEMS pressure sensor fabricated on an optical fiber”. In: *IEEE photonics technology letters* 13.9 (2001), pp. 993–995.

[70] Muhammad Ali Shah et al. “Design approaches of MEMS microphones for enhanced performance”. In: *Journal of sensors* 2019 (2019).

[71] Vinayak Pachkawade. “State-of-the-art in mode-localized MEMS coupled resonant sensors: A comprehensive review”. In: *IEEE Sensors Journal* 21.7 (2021), pp. 8751–8779.

[72] Philip W Anderson. “Absence of diffusion in certain random lattices”. In: *Physical review* 109.5 (1958), p. 1492.

[73] Chun Zhao et al. “A review on coupled MEMS resonators for sensing applications utilizing mode localization”. In: *Sensors and Actuators A: Physical* 249 (2016), pp. 93–111.

[74] Vinayak Pachkawade. “Ultra-precise MEMS based bio-sensors”. In: *Biosensor-Current and Novel Strategies for Biosensing* (2020).

[75] Lucas B Soldano and Erik CM Pennings. “Optical multi-mode interference devices based on self-imaging: principles and applications”. In: *Journal of lightwave technology* 13.4 (1995), pp. 615–627.

[76] Hirohito Yamada et al. “Optical directional coupler based on Si-wire waveguides”. In: *IEEE photonics technology letters* 17.3 (2005), pp. 585–587.

[77] Michael A Seldowitz, Jan P Allebach, and Donald W Sweeney. “Synthesis of digital holograms by direct binary search”. In: *Applied optics* 26.14 (1987), pp. 2788–2798.

[78] Bing Shen et al. “An integrated-nanophotonics polarization beamsplitter with 2.4$\times$ 2.4 μm2 footprint”. In: *Nature Photonics* 9.6 (2015), pp. 378–382.

[79] Tao Wang et al. “Ultra-compact reflective mode converter based on a silicon subwavelength structure”. In: *Applied Optics* 59.9 (2020), pp. 2754–2758.

[80] Hao Jia et al. “Ultra-compact dual-polarization silicon mode-order converter”. In: *Optics Letters* 44.17 (2019), pp. 4179–4182.

[81] Hansi Ma et al. “Ultra-compact and efficient 1$\times$ 2 mode converters based on rotatable direct-binary-search algorithm”. In: *Optics Express* 28.11 (2020), pp. 17010–17019.

[82] Weijie Chang et al. “Inverse design of a single-step-etched ultracompact silicon polarization rotator”. In: *Optics Express* 28.19 (2020), pp. 28343–28351.

[83] Hucheng Xie et al. “Inversely designed 1$\times$ 4 power splitter with arbitrary ratios at 2-μm spectral band”. In: *IEEE Photonics Journal* 10.4 (2018), pp. 1–6.

[84] Huan Yuan et al. "An ultra-compact dual-channel multimode wavelength demultiplexer based on inverse design". In: *Results in Physics* 27 (2021), p. 104489.

[85] Luluzi Lu et al. "Inverse-designed ultra-compact star-crossings based on PhC-like subwavelength structures for optical intercross connect". In: *Optics Express* 25.15 (2017), pp. 18355–18364.

[86] Kwaku O Abrokwah. "Characterization and modeling of plasma etch pattern dependencies in integrated circuits". PhD thesis. Massachusetts Institute of Technology, 2006.

[87] Hansi Ma et al. "Arbitrary-direction, multichannel and ultra-compact power splitters by inverse design method". In: *Optics Communications* 462 (2020), p. 125329.

[88] Melanie Mitchell. *An introduction to genetic algorithms*. MIT press, 1998.

[89] Zejie Yu, Haoran Cui, and Xiankai Sun. "Genetic-algorithm-optimized wideband on-chip polarization rotator with an ultrasmall footprint". In: *Optics letters* 42.16 (2017), pp. 3093–3096.

[90] Zejie Yu, Haoran Cui, and Xiankai Sun. "Genetically optimized on-chip wideband ultracompact reflectors and Fabry–Perot cavities". In: *Photonics Research* 5.6 (2017), B15–B19.

[91] Yuan Xie et al. "Design of an arbitrary ratio optical power splitter based on a discrete differential multiobjective evolutionary algorithm". In: *Applied Optics* 59.6 (2020), pp. 1780–1785.

[92] Zhouhui Liu et al. "Integrated nanophotonic wavelength router based on an intelligent algorithm". In: *Optica* 6.10 (2019), pp. 1367–1373.

[93] Xiaofei Wang et al. "Polarization-independent fiber-chip grating couplers optimized by the adaptive genetic algorithm". In: *Optics Letters* 46.2 (2021), pp. 314–317.

[94] Randy L Haupt and Douglas H Werner. *Genetic algorithms in electromagnetics*. John Wiley & Sons, 2007.

[95] Zhongwei Jin et al. "Complex inverse design of meta-optics by segmented hierarchical evolutionary algorithm". In: *ACS nano* 13.1 (2019), pp. 821–829.

[96] James Kennedy and Russell Eberhart. "Particle swarm optimization". In: *Proceedings of ICNN'95-international conference on neural networks*. Vol. 4. IEEE. 1995, pp. 1942–1948.

[97] Yi Zhang et al. "A compact and low loss Y-junction for submicron silicon waveguide". In: *Optics express* 21.1 (2013), pp. 1310–1316.

[98] Yuhui Shi and Russell Eberhart. "A modified particle swarm optimizer". In: *1998 IEEE international conference on evolutionary computation proceedings. IEEE world congress on computational intelligence (Cat. No. 98TH8360)*. IEEE. 1998, pp. 69–73.

[99] Jason CC Mak et al. "Binary particle swarm optimized 2× 2 power splitters in a standard foundry silicon photonic platform". In: *Optics letters* 41.16 (2016), pp. 3868–3871.

[100] Qichao Lu et al. "Particle swarm optimized ultra-compact polarization beam splitter on silicon-on-insulator". In: *Photonics and Nanostructures-Fundamentals and Applications* 32 (2018), pp. 19–23.

[101] Jae Woong Yoon et al. "Wideband Omnidirectional Polarization-Insensitive Light Absorbers Made with 1D Silicon Gratings". In: *Advanced Optical Materials* 2.12 (2014), pp. 1206–1212.

[102] Zhenwei Xie et al. "Ultra-broadband on-chip twisted light emitter for optical communications". In: *Light: Science & Applications* 7.4 (2018), pp. 18001–18001.

[103] Xinlun Cai et al. "Integrated compact optical vortex beam emitters". In: *Science* 338.6105 (2012), pp. 363–366.

[104] Nenad Bozinovic et al. "Terabit-scale orbital angular momentum mode division multiplexing in fibers". In: *science* 340.6140 (2013), pp. 1545–1548.

[105] O Sigmund. "Topology optimization in nano-photonics". In: *AIP Conference Proceedings*. Vol. 1176. 1. American Institute of Physics. 2009, pp. 26–28.

[106] Martin Philip Bendsøe and Noboru Kikuchi. "Generating optimal topologies in structural design using a homogenization method". In: *Computer methods in applied mechanics and engineering* 71.2 (1988), pp. 197–224.

[107] Jie Huang et al. "Digital nanophotonics: The highway to the integration of subwavelength-scale photonics: Ultra-compact, multi-function nanophotonic design based on computational inverse design". In: *Nanophotonics* 10.3 (2020), pp. 1011–1030.

[108] Alexander Yukio Piggott. *Automated design of photonic devices*. Alexander Yukio Piggott, 2018.

[109] Mike Giles and Niles A Pierce. "An introduction to the adjoint approach to design". In: (2000).

[110] Alexander Y Piggott et al. "Inverse design and demonstration of a compact and broadband on-chip wavelength demultiplexer". In: *Nature Photonics* 9.6 (2015), pp. 374–377.

[111] Christopher M Lalau-Keraly et al. "Adjoint shape optimization applied to electromagnetic design". In: *Optics express* 21.18 (2013), pp. 21693–21701.

[112] Wanjing Kuang, Lin Ma, Zuyuan He, et al. "Ultra-Compact Low Loss Polymer Wavelength (De) Multiplexer With Spot-Size Convertor Using Topology Optimization". In: *IEEE Photonics Journal* 13.3 (2021), pp. 1–9.

[113] Alexander Y Piggott et al. "Inverse design and implementation of a wavelength demultiplexing grating coupler". In: *Scientific reports* 4.1 (2014), pp. 1–5.

[114] Kaiyuan Wang et al. "Inverse design of digital nanophotonic devices using the adjoint method". In: *Photonics Research* 8.4 (2020), pp. 528–533.

[115] Yasuhide Tsuji and Koichi Hirayama. "Design of optical circuit devices using topology optimization method with function-expansion-based refractive index distribution". In: *IEEE photonics technology letters* 20.12 (2008), pp. 982–984.

[116] Jesse Lu and Jelena Vučković. "Nanophotonic computational design". In: *Optics express* 21.11 (2013), pp. 13351–13367.

[117] David Sell et al. "Large-angle, multifunctional metagratings based on freeform multimode geometries". In: *Nano letters* 17.6 (2017), pp. 3752–3757.

[118] Tyler W Hughes et al. "Adjoint method and inverse design for nonlinear nanophotonic devices". In: *ACS Photonics* 5.12 (2018), pp. 4781–4787.

[119] Thaibao Phan et al. "High-efficiency, large-area, topology-optimized metasurfaces". In: *Light: Science & Applications* 8.1 (2019), p. 48.

[120] Ronghui Lin et al. "Inverse design of plasmonic metasurfaces by convolutional neural network". In: *Optics Letters* 45.6 (2020), pp. 1362–1365.

[121] Jing He et al. "Plasmonic nanoparticle simulations and inverse design using machine learning". In: *Nanoscale* 11.37 (2019), pp. 17444–17459.

[122] Sunny Chugh et al. "Machine learning regression approach to the nanophotonic waveguide analyses". In: *Journal of Lightwave Technology* 37.24 (2019), pp. 6080–6089.

[123] Xiaozhong Li et al. "Deep neural network for plasmonic sensor modeling". In: *Optical Materials Express* 9.9 (2019), pp. 3857–3862.

[124] Dianjing Liu et al. "Training deep neural networks for the inverse design of nanophotonic structures". In: *Acs Photonics* 5.4 (2018), pp. 1365–1369.

[125] Zhaocheng Liu et al. "Generative model for the inverse design of metasurfaces". In: *Nano letters* 18.10 (2018), pp. 6570–6576.

[126] Min Teng et al. "Broadband SOI mode order converter based on topology optimization". In: *2018 Optical Fiber Communications Conference and Exposition (OFC)*. IEEE. 2018, pp. 1–3.

[127] Kiyanoush Goudarzi et al. "Ultra low loss broadband 1×2 optical power splitters with various splitting ratios". In: *Optics Continuum* 1.9 (2022), pp. 1888–1895.

[128] Alexander Y Piggott et al. "Inverse design and demonstration of a compact and broadband on-chip wavelength demultiplexer". In: *Nature Photonics* 9.6 (2015), pp. 374–377.

[129] Peng Li, Jun-Yu Ou, and Jize Yan. "Method for optimising the performance of PML in anchor-loss limited model via COMSOL". In: *IET Science, Measurement & Technology* 16.6 (2022), pp. 327–336.

[130] Valentina Zega et al. "Analysis of frequency stability and thermoelastic effects for slotted tuning fork MEMS resonators". In: *Sensors* 18.7 (2018), p. 2157.

[131] Zengkai Shao et al. "On-chip switchable radially and azimuthally polarized vortex beam generation". In: *Optics Letters* 43.6 (2018), pp. 1263–1266.

[132] WF Eickhoff and RJAPL Ulrich. "Optical frequency domain reflectometry in single-mode fiber". In: *Applied Physics Letters* 39.9 (1981), pp. 693–695.

[133] Kivilcim Yüksel, Marc Wuilpart, and Patrice Mégret. "Analysis and suppression of nonlinear frequency modulation in an optical frequency-domain reflectometer". In: *Optics express* 17.7 (2009), pp. 5845–5851.

[134] Yang Du et al. "Cryogenic temperature measurement using Rayleigh backscattering spectra shift by OFDR". In: *IEEE Photonics Technology Letters* 26.11 (2014), pp. 1150–1153.

[135] Zhongjin Lin and Wei Shi. "Broadband, low-loss silicon photonic Y-junction with an arbitrary power splitting ratio." In: *Optics express* 27.10 (2019), pp. 14338–14343.

[136] Zhen Guo et al. "Ultimate spatial resolution realisation in optical frequency domain reflectometry with equal frequency resampling". In: *Sensors* 21.14 (2021), p. 4632.

[137] Jakob Søndergaard Jensen and Ole Sigmund. "Topology optimization for nano-photonics". In: *Laser & Photonics Reviews* 5.2 (2011), pp. 308–321.

[138] Yuxiao Liu et al. "Direct-binary-search-optimized compact silicon-based polarization beam splitter using a pixelated directional coupler". In: *Optics Communications* 484 (2021), p. 126670.

[139] Mohammad H Tahersima et al. "Deep neural network inverse design of integrated photonic power splitters". In: *Scientific reports* 9.1 (2019), pp. 1–9.

[140] Robert Halir et al. "Ultra-broadband nanophotonic beamsplitter using an anisotropic sub-wavelength metamaterial". In: *Laser & Photonics Reviews* 10.6 (2016), pp. 1039–1046.

[141] Hansi Ma et al. "Inverse-designed arbitrary-input and ultra-compact $1\times$ N power splitters based on high symmetric structure". In: *Scientific Reports* 10.1 (2020), pp. 1–7.

[142] Apratim Majumder et al. "Ultra-compact polarization rotation in integrated silicon photonics using digital metamaterials". In: *Optics express* 25.17 (2017), pp. 19721–19731.

[143] Yang Du et al. "Cryogenic temperature measurement using Rayleigh backscattering spectra shift by OFDR". In: *IEEE Photonics Technology Letters* 26.11 (2014), pp. 1150–1153.

[144] Victor J Katz. "The history of Stokes' theorem". In: *Mathematics Magazine* 52.3 (1979), pp. 146–156.

[145] Vilson R Almeida and Michal Lipson. "Optical bistability on a silicon chip". In: *Optics letters* 29.20 (2004), pp. 2387–2389.

[146] Hailong Pi et al. "Coherent generation of arbitrary first-order Poincaré sphere beams on an Si chip". In: *Optics Express* 30.5 (2022), pp. 7342–7355.

[147] Wim Bogaerts et al. "Silicon microring resonators". In: *Laser & Photonics Reviews* 6.1 (2012), pp. 47–73.

[148] Hailong Pi et al. "Integrated vortex beam emitter in the THz frequency range: Design and simulation". In: *APL Photonics* 5.7 (2020), p. 076102.

[149] Xiangming Xu et al. "On-chip optical pulse train generation through the optomechanical oscillation". In: *Optics Express* 29.23 (2021), pp. 38781–38795.

[150] Hailong Pi et al. "Coherent generation of arbitrary first-order Poincaré sphere beams on an Si chip". In: *Optics Express* 30.5 (2022), pp. 7342–7355.

[151] Bo Peng et al. "What is and what is not electromagnetically induced transparency in whispering-gallery microcavities". In: *Nature communications* 5.1 (2014), pp. 1–9.

[152] Dominik G Rabus. *Integrated ring resonators*. Springer, 2007.

[153] Amnon Yariv. "Universal relations for coupling of optical power between microresonators and dielectric waveguides". In: *Electronics letters* 36.4 (2000), pp. 321–322.

[154] Shun Lien Chuang. *Physics of photonic devices*. John Wiley & Sons, 2012.

[155] Yasuharu Suematsu and Katsumi Kishino. "Coupling coefficient in strongly coupled dielectric waveguides". In: *Radio Science* 12.4 (1977), pp. 587–592.

[156] Peter T Rakich et al. "Trapping, corralling and spectral bonding of optical resonances through optically induced potentials". In: *Nature Photonics* 1.11 (2007), pp. 658–665.

[157] Hailong Pi et al. "Positive and negative pull-back instabilities in mode splitting optomechanical devices". In: *ACS Photonics* 9.1 (2021), pp. 123–131.

[158] Feifan Wang et al. "Controlling microring resonator extinction ratio via metal-halide perovskite nonlinearity". In: *Advanced Optical Materials* 9.22 (2021), p. 2100783.

[159] Joyce KS Poon et al. “Matrix analysis of microring coupled-resonator optical waveguides”. In: *Optics express* 12.1 (2004), pp. 90–103.

[160] Tal Carmon, Lan Yang, and Kerry J Vahala. “Dynamical thermal behavior and thermal self-stability of microcavities”. In: *Optics express* 12.20 (2004), pp. 4742–4750.

[161] Haitan Xu et al. “Ultra-sensitive chip-based photonic temperature sensor using ring resonator structures”. In: *Optics Express* 22.3 (2014), pp. 3098–3104.

[162] John E Heebner et al. “Optical transmission characteristics of fiber ring resonators”. In: *IEEE journal of quantum electronics* 40.6 (2004), pp. 726–730.

[163] Kwang T Kim, Kyu J Cho, and Byeong H Lee. “Empirical analysis of widely tunable fused fiber coupler assisted by external medium of high thermo-optic coefficient”. In: *Fiber and Integrated Optics* 30.1 (2011), pp. 61–72.

[164] Yu Feng et al. “Theory analysis of the optical mode localized sensing based on coupled ring resonators”. In: *Optics Express* 29.20 (2021), pp. 32505–32522.

[165] Damian Presti, Fabian A Videla, and Gustavo A Torchia. “Optical fiber ring resonator as a high-resolution spectrometer. Characterization and applications with single line diode lasers”. In: *Optical Engineering* 57.5 (2018), pp. 057108–057108.

[166] Ali Masoudi and Trevor P Newson. “Contributed Review: Distributed optical fibre dynamic strain sensing”. In: *Review of scientific instruments* 87.1 (2016), p. 011501.

[167] Juncheng Xu et al. “A novel temperature-insensitive optical fiber pressure sensor for harsh environments”. In: *IEEE Photonics Technology Letters* 17.4 (2005), pp. 870–872.

[168] Thomas Allsop and Ronald Neal. “A review: application and Implementation of optic fibre sensors for gas detection”. In: *Sensors* 21.20 (2021), p. 6755.

[169] Stephen Lin et al. “Computational lithography for silicon photonics design”. In: *IEEE Journal of Selected Topics in Quantum Electronics* 26.2 (2019), pp. 1–8.

[170] Xu Ma and Gonzalo R Arce. *Computational lithography*. John Wiley & Sons, 2011.

[171] Li-Ye Xiao et al. “A Novel Optical Proximity Correction (OPC) System Based on Deep Learning Method for the Extreme Ultraviolet (EUV) Lithography”. In: *Progress In Electromagnetics Research* 176 (2023), pp. 95–108.

[172] Xiangming Xu et al. “On-chip optical pulse train generation through the optomechanical oscillation”. In: *Optics Express* 29.23 (2021), pp. 38781–38795.

[173] Jaime Cardenas et al. “Wide-bandwidth continuously tunable optical delay line using silicon microring resonators”. In: *Optics express* 18.25 (2010), pp. 26525–26534.